

BOR DERGİSİ

JOURNAL OF BORON

CILT/VOL

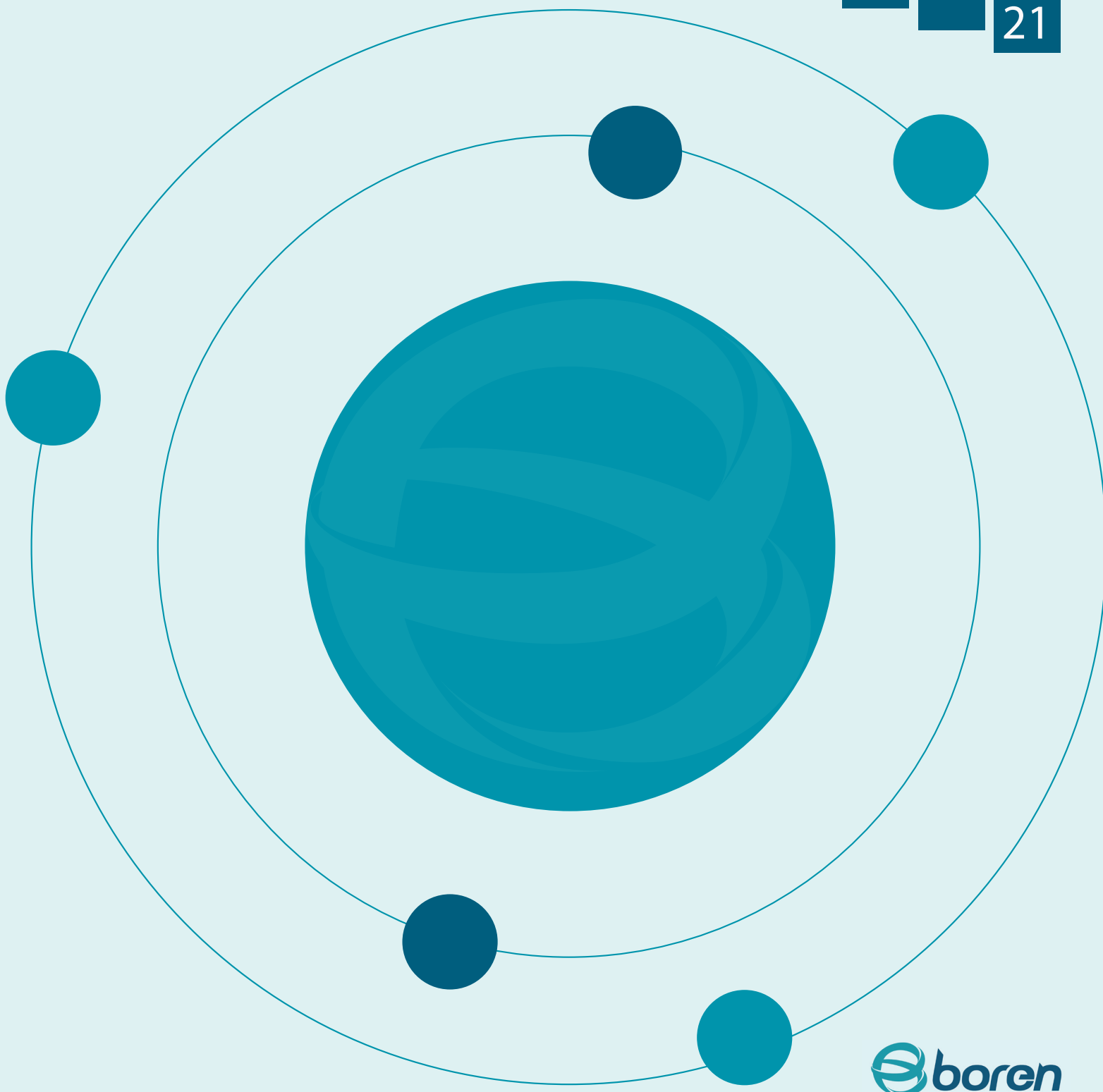
06

SAYI/ISSUE

01

YIL/YEAR

20
21



BOR DERGİSİ

JOURNAL OF BORON

CİLT VOL 06 SAYI ISSUE 01 YIL YEAR 2021

Türkiye Enerji Nükleer Maden Araştırma Kurumu (TENMAK) Adına İmtiyaz Sahibi

Owner on Behalf of TENMAK

Başkan/President

Dr. Abdulkadir Balıkçı

Baş Editör/Editor in Chief

Dr. Zafer Evis (Ankara, Türkiye)

Editörler/Editors

Dr. Abdulkerim Yörükoğlu (Ankara, Türkiye)

Dr. Fatih Akkurt (Ankara, Türkiye)

Dr. Sedat Sürdem (Ankara, Türkiye)

DANIŞMA KURULU

ADVISORY BOARD

Dr. Ali Çırpan (Ankara, Türkiye)

Dr. Arun K. Chattopadhyay (Pittsburgh, ABD)

Dr. Atakan Peker (Washington, ABD)

Dr. Ayşen Tezcaner (Ankara, Türkiye)

Dr. Bilal Demirel (Kayseri, Türkiye)

Dr. Cahit Helvacı (İzmir, Türkiye)

Dr. Çetin Çakanyıldırım (Çorum, Türkiye)

Derya Maraşlıoğlu (Ankara, Türkiye)

Dr. Dursun Ali Köse (Çorum, Türkiye)

Dr. Duygu Ağaoğulları (İstanbul, Türkiye)

Dr. Emin Bayraktar (Paris, Fransa)

Dr. Erol Pehlivan (Konya, Türkiye)

Dr. Fatih Algı (Aksaray, Türkiye)

Dr. Gülay Özkan (Ankara, Türkiye)

Dr. Gülhan Özbayoğlu (Ankara, Türkiye)

Dr. Hatem Akbulut (Sakarya, Türkiye)

Dr. Hüseyin Çelikkan (Ankara, Türkiye)

Dr. İhsan Efeoğlu (Erzurum, Türkiye)

Dr. İsmail Çakmak (İstanbul, Türkiye)

Dr. İsmail Duman (İstanbul, Türkiye)

Dr. İsmail Girgin (Ankara, Türkiye)

Dr. Jamal Ahmad (Abu Dhabi, BAE)

Dr. Mehmet Suat Somer (İstanbul, Türkiye)

Dr. Metin Gürü (Ankara, Türkiye)

Dr. Nalan Kabay (İzmir, Türkiye)

Dr. Nuran Ay (Eskişehir, Türkiye)

Dr. Olcay Şendil (Ankara, Türkiye)

Dr. Onuralp Yücel (İstanbul, Türkiye)

Dr. Osman Okur (Kocaeli, Türkiye)

Dr. Rafaqat Hussain (Islamabad, Pakistan)

Dr. Rasim Yarım (Friedrichshafen, Almanya)

Dr. Raşit Koç (Illinois, ABD)

Dr. Sait Gezgin (Konya, Türkiye)

Dr. Şafak Gökhan Özkan (İstanbul, Türkiye)

Dr. Şener Oktik (İstanbul, Türkiye)

Dr. Taner Yıldırım (Maryland, ABD)

Dr. Yuri Grin (Dresden, Almanya)

Sorumlu Yazı İşleri Müdürü Manager of Publication

Dr. Sedat Sürdem

Endüstriyel İlişkiler Koordinatörü

e-mail: sedat.surdem@tenmak.gov.tr

Editorial Teknik Personel/Editorial Technical Staff

Dr. Abdulkadir Solak

Sema Akbaba

Sinem Erdemir Guran

Yayınçı/Publisher

TENMAK Bor Araştırma Enstitüsü (BOREN)

Yayın İdare Adresi/Address of Publication Manager

Dumlupınar Bulvarı (Eskişehir Yolu 7. km), No:166, D Blok,
06530, Ankara, Türkiye

Tel: (0312) 201 36 00

Fax: (0312) 219 80 55

boren.journal@tenmak.gov.tr

<https://dergipark.org.tr/boron>

Yayın Türü/Type of Publication: Yaygın süreli yayın

Yayın Aralığı/Range of Publication: 3 Aylık

Basım Tarihi/Publication Date: 31/03/2021

Matbaa/Printing: Kuban Matbaacılık Yayıncılık

Bor Dergisi uluslararası hakemli bir dergidir. Dergi, ULAKBİM TR Dizin ve Google Scholar tarafından indekslenmeyece olup yılda dört defa yayımlanmaktadır. Derginin yazım kılavuzuna, telîf hakkı devir formuna ve yayınlanan makalelere <https://dergipark.org.tr/boron> adresinden ulaşılabilir. / Journal of Boron is International refereed journal. Journal of Boron is indexed by ULAKBİM TR Indexed and Google Scholar, published quarterly a year. Please visit the Journal website <https://dergipark.org.tr/boron> for writing rules, copyright form and published articles.



İÇİNDEKİLER/CONTENTS

Investigation of mechanical and tribological characteristics of Ni-B coatings deposited on steel.....	209
.....Fatih Doğan, Erhan Duru, Mehmet Uysal, Hatem Akbulut, Serdar Aslan	
Ni-B katalizörünün hidrojen üretiminde yanıt yüzey yöntemi ile optimizasyonu.....	216
.....Hüseyin Elçiçek	
Zinc borate chemical garden and zinc borate powders from tincal mineral and zinc sulfate heptahydrate...	227
.....Burcu Alp, Mehmet Gönen, Sevdiye Atakul Savrik, Devrim Balkose	
The role of B_2O_3 in lithium-zinc-calcium-silicate glass for improving the radiation shielding competencies: A theoretical evaluation via Phy-X/PSD.....	236
.....Recep Kurtuluş, Taner Kavas	
Kolemanit katkısının kordiyerit cam-seramiklerin kristalizasyon davranışları üzerindeki etkilerinin araştırılması..	243
.....Süleyman Akpinar, Atilla Evcin	
Synthesis and characterization of carborane-functionalized hyperbranched polyester for boron neutron capture therapy.....	252
.....Gülten Özçayan, Yüksel Şahin, Ernur Söylemez, M. Elif Ünsal	



Investigation of mechanical and tribological characteristics of Ni-B coatings deposited on steel

Fatih Doğan^{1*}, Erhan Duru², Mehmet Uysal³, Hatem Akbulut⁴, Serdar Aslan⁵

¹Sakarya University, Institute of Natural Science, Sakarya, 54187, Turkey

ORCID orcid.org/0000-0001-9798-0153

²Sakarya University, Faculty of Engineering, Department of Metallurgy and Materials Engineering, Sakarya, 54187, Turkey

ORCID orcid.org/0000-0002-6205-6566

³Sakarya University, Faculty of Engineering, Department of Metallurgy and Materials Engineering, Sakarya, 54187, Turkey

ORCID orcid.org/0000-0002-9396-7450

⁴Sakarya University, Faculty of Engineering, Department of Metallurgy and Materials Engineering, Sakarya, 54187, Turkey

ORCID orcid.org/0000-0002-6299-136X

⁵Sakarya University, Faculty of Engineering, Department of Metallurgy and Materials Engineering, Sakarya, 54187, Turkey

ORCID orcid.org/ 0000-0001-5061-6338

ARTICLE INFO

Article history:

Received July 1, 2020

Accepted December 6, 2020

Available online March 31, 2021

Research Article

DOI: 10.30728/boron.762584

Keywords:

Hardness

Ni-B electrodeposited coating

Wear mechanism

ABSTRACT

In this study, mechanical properties and wear behaviors of Ni-B coatings were investigated. The mechanical and wear properties of the coating change depending on the nickel boride (Ni_2B and Ni_3B) phases formed after heat treatment at 400°C for 2 hours. Nodular structure formed in the surface morphology and columnar growth in the cross-sectional images of the coating as-deposited and annealed was examined by scanning electron microscopy (SEM). The amorphous structure at as-deposited and the nickel boride phases formed in the structure after annealing were analyzed by X-ray diffraction (XRD). Using the Debye-Scherrer formula, the effect of the phases formed in the structure on the crystalline grain size after annealing was calculated. The hardness values of the coating as-deposited and annealed were calculated by nano-indentation hardness measurement method. Wear tests of the coatings, which were subjected to heat treatment at 400°C for 2 h, were carried out in dry conditions without the use of lubricants, at different loads (1N-3N-5N), at a sliding speed of 25 mm/s and at 25°C. After the wear tests, the wear surfaces of the samples were imaged by SEM and their chemical compositions were analyzed by energy dispersive spectroscopy (EDS). The wear rate and coefficients of friction the samples tested under different loads had compared each other.

1. Introduction

Studies on coating technology to improve the surface properties of materials have been increasing. Although hard chrome is the most used in surface coating processes in the industry, alternative studies are carried out due to the lack of mechanical properties of this coating and the low service life. Mild carbon steels are used more commonly than alloy and mild steels due to their low cost, and they are subjected to different surface treatments since their strength and wear resistance are low [1].

To increase the strength and wear resistance of the material in the industrial area, surface treatments are made on mild carbon steels by electrodeposition coating method. Pure nickel coating produced by electrodeposition method cannot show high resistance in wear environments due to its low hardness. As is known, the strength of the material improves with the

alloying [2]. The most concentrated studies as an alternative to hard chrome plating are Ni alloy coatings. Ni alloy coatings are becoming widespread in industrial areas such as aviation, automobile, and defense due to their low deposition cost, easy of use industry, high hardness values, very good friction, and wear properties. Especially Ni-B alloy coatings are the most preferred research area due to their superior mechanical and tribological properties. Ni-B coatings produced by electrodeposition coating technique are formed in amorphous structure. The mechanical and tribological properties of the Ni-B coatings are affected by the applied heat treatment. Boron element added to improve the mechanical properties of its alloy dissolves in the matrix and crystal nickel boride phases are formed after the coating is subjected to heat treatment [3]. In annealed coatings, there is a significant increase in the hardness of the coating with the grain refining effect resulting from the crystallization of nickel and the

*Corresponding author: drdoganfatih@gmail.com

formation of Ni_3B and Ni_2B phases. Thus, increasing coating hardness also improves the wear properties of the coating [4]. Although it has been reported in the previous studies that the formation of Ni_3B and Ni_2B crystal phases increases the hardness and wear resistance of the coating, it has not been fully explained that these phases also improve the strength and wear behavior of the coating [5,6].

In this study, the microstructure, hardness and tribology properties of Ni-B coatings produced by the pulse current electrodeposition method were investigated. Particularly, attention was paid to the effect of heat treatment on the strength increase of the coating. The results obtained showed that Ni-B coating produced without using any lubricating reinforcement element is resistant to the applied wear medium.

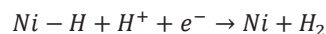
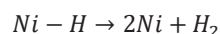
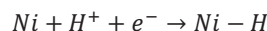
2. Methods

Mild carbon steel of 5 mm thickness, 40 mm x 30 mm size was used for the cathode in Ni-B electrodeposition coating. The substrate surface was polished using alumina after mechanically sanded using 200-400-600-800-1000-1200 grit SiC polishing paper to remove the roughness of the sample surfaces, increase adhesion and ensure homogeneity of the coating. Then, samples that cleaned with ethanol in ultrasonic bath were rinsed with deionized water and dried. Finally, before starting the coating procedure, the samples were immersed in $\text{HCl}:\text{H}_2\text{O}$ (1:3) solution to clean the oxide layer that may form on the substrate surface, then cleaned with deionized water and placed in the coating solution. After the coating process, the samples were heat treated under an argon atmosphere at 400°C for 2 hours.

Table 1. Chemical composition and operating conditions of Ni-B electrodeposition coating.

Chemical composition	
Chemicals	Composition (g/L)
$\text{NiSO}_4 \cdot 6\text{H}_2\text{O}$	240
$\text{NiCl}_2 \cdot 6\text{H}_2\text{O}$	45
H_3BO_3	30
TMAB(Trimethylamineborane)	3
Coating bath conditions	
pH	3
Temperature (°C)	50
Current density (mA/cm^2)	4.5
Stirring rate (rpm)	450
Deposition time (min.)	60
Anode	Ni (%99.9)
Cathode	S-37 steel (mild carbon steel)

Figure 1 shows a schematic of the electrodeposition Ni-B alloy coating bath. The chemical composition and operation conditions of the Ni-B coating bath are given in Table 1. Electrodeposition of nickel in the Ni-B coating and reactions with hydrogen discharge are given below:



Additionally, the TMAB compound used as the boron source in the coating bath is included in the Ni matrix by the following reaction [7]:

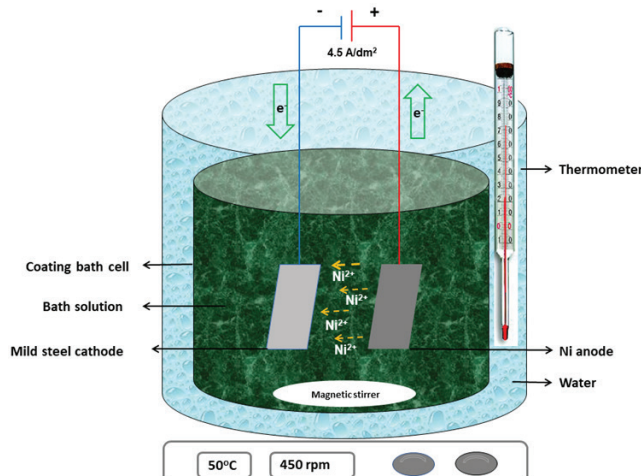
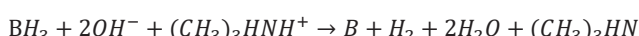


Figure 1. Schematic illustration of electrodeposited Ni-B alloy coating bath.

The surface morphology and cross-sectional view of the coating as-deposited and annealed were examined using the JEOL 6060-LV scanning electron microscope (SEM). The crystal structures of the coatings were characterized by the X-ray diffraction (XRD) technique using the Rigaku D/MAX 2000 X-ray generator and Cu K α radiation diffractometer with a wavelength of 1.54059 Å. Crystalline sizes were calculated by the formula of Debye-Scherrer. The hardness values of the coating after heat treatment were measured using the Nano hardness device (Anton Paar Nanoindentation tester: NHT³) with Berkovich indenter under load of 25 mN. The hardness measurements were made from the cross-sectional area of the coating and hardness values obtained from five different points were averaged for each sample. In addition, the load-depth curves of the samples as-deposited and heat treated were analyzed by nano-indentation test. Tribological behavior of the coatings was performed on the Tribometer (CSM Instruments TRB 18-317) by dry sliding against the Al_2O_3 ball (Ø 6 mm). The wear tests were

carried out at $25^{\circ}\text{C} \pm 2$ room temperature and $45\% \pm 5$ relative humidity media. Wear tests were carried out at different applied loads (1N-3N-5N) at sliding rates of 25 cm/s over 400 m sliding distance, and wear rate and friction coefficient values of each sample were calculated. The image of wear traces on the surface of the coating after the wear tests were obtained by SEM. Elemental analysis of sample surfaces abraded at different loads was performed with EDS. In addition, the coefficient of friction values and wear rates of the samples were analyzed after the friction test.

3. Results and Discussion

The surface morphology and cross-sectional images of the as-deposited and the annealed coatings are shown in Figure 2. Surface morphologies of Ni-B coatings are in the form of cauliflower structure and it is seen that the nodular structure of the coating is refinement after heat treatment. The void structure seen on the coating surface before heat treatment decreased after the heat treatment. This can be explained by the fact that nickel borides formed after annealed decrease the porous structure of the coating and form a denser layer. In addition, it can be stated that the smoothness of the coating surface increases with the decrease in the nickel crystal's grain size [8]. The columnar growth observed in the coatings was dense and continuous, and there were no defects in the adhesion of the coating to the substrate. When the interface between the coating and the substrate is examined, it is seen that while significant defects are observed in the coating before

heat treatment, it is seen that defects are reduced and adhesion is better after heat treatment. The columnar structure which improves the tribological properties of the coating prevents adhesive wear by reducing the contact area between the coating surface and the opposite surface. Thus, it can be said that heat treatment can positively affect the internal tension of the coating, and the load applied during friction can be distributed evenly and the load on the Ni matrix phase can be reduced [9].

The XRD spectra of Ni-B coatings as-deposited and heat treated are shown in Figure 3. It is seen that the nickel phase structure, which is semi-amorphous before the heat treatment, the Ni crystal phase structures and nickel borides after the heat treatment. This transformation resulted with the formation of (111), (200), (220) planes at 44.36° , 51.80° and 76.28° peaks, respectively. In the phase diagram in the literature, the nickel in the amorphous microstructure crystallizes at different temperatures to form Ni_3B and Ni_2B phases [10]. After the coatings annealed, the amorphous phase of the nickel crystal peaks decreased, while crystal nickel boride (Ni_3B and Ni_2B) phases are formed. Nickel borides formed in the coating prevent nucleation of nickel phases. The formation of narrow and dense peaks of nickel and nickel boride phases after heat treatment shows that the crystallinity of the structure increases [11]. With the Debye-Scherrer formula (Eq.1) given below, the average crystallite size for the nickel crystal was calculated as 41 nm [12]. Nickel borides formed after annealed can reduce the

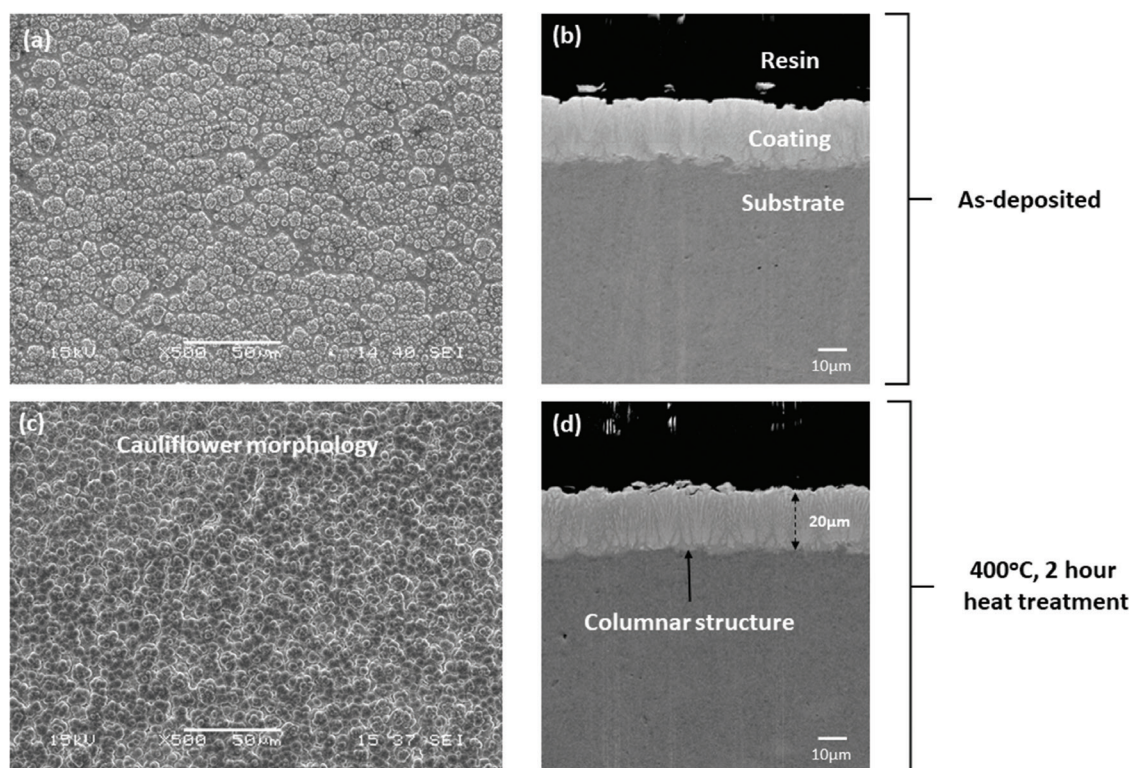


Figure 2. Surface morphology and cross-section images of Ni-B alloy coatings (a, b) as-deposited and (c,d) heat treated, respectively.

crystalline grain boundaries and dislocation areas and make the coating more compact. Thus, increased coating strength can show high wear resistance during friction.

$$d = \frac{0.9\lambda}{B \cos \theta} \quad (1)$$

Where, d is mean crystalline size, λ is X-ray wavelength (0.15418 nm), B is the corrected peak width at half maximum intensity (FWHM) and θ is Bragg diffraction angle. The crystallinity of the coating, which increases because of heat treatment, can be explained by the inhibition of crystal grain growth in the matrix.

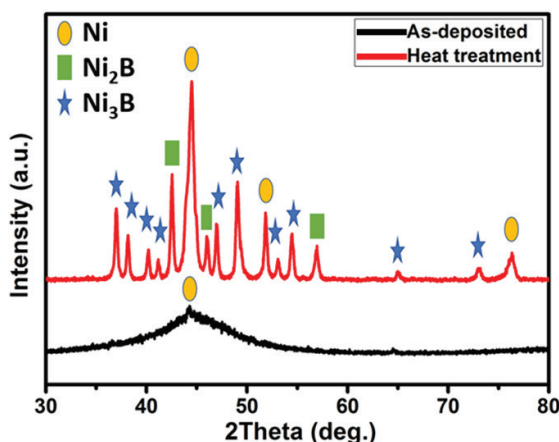


Figure 3. XRD result of Ni-B alloy coating as-deposited and heat treated.

The hardness measurements and load-depth curve performed on the coatings as-deposited and annealed are given in Figure 4, respectively. As can be seen in Figure 4a, the hardness and elastic modulus of the coating after heat treatment was increased significantly. While the hardness of the amorphous coating was 610 HV, it increased to 838 HV with the precipitation of the Ni_3B and Ni_2B crystals. The increase in hardness and elastic modulus can be explained by the precipita-

tion of Ni_3B and Ni_2B phases, which are formed after heat treatment and are compatible with XRD results. Increased hardness after heat treatment increases the wear resistance of the coating surface exposed to wear [13]. Also, the decrease in the grain size of the crystal after heat treatment can be explained by the higher hardness of the coating than the Hall-Petch effect [14]. In addition, the non-porous and dense structure formed on the coating surface improves both the hardness and wear resistance of the coating. The trace images that appear uniformly in the cross section of the coating show the nano-indentation hardness test. Only at the beginning of the loading/unloading plot curve of the test performed under a load of 25 mN for 10 seconds, relatively little curvature is seen. Thus, it can be stated that the samples are not deformed too much. According to the results of the nano-indentation test (Figure 4b), the high indentation depth that occurs when the load applied on the material is removed shows that the material is ductile. It has been observed that the depth decreases with the increase in the hardness of the material after heat treatment. The sample, which showed an elastic structure before heat treatment, became brittle after annealed and increased the coating hardness.

Low and high magnification SEM images of the wear traces of coatings annealed at 400°C for 2-hours and tested at different loads are shown in Figure 5. The wear trace of the sample, which was abraded by applying 1N load (Figure 5a), is more than the other samples. In addition, it is seen that there are more cracks and spills in the wear trace. When the wear trace images are examined, it was observed that the wear trace width was the lowest in the wear with 3N load (Figure 5c). The contact surface area is increased by increasing the applied load to 5N and thus the wear trace width of the coating is increased (Figure 5e). Also, the residual particles formed by increasing the load to 5N increased the wear trace width and roughness [15]. High magnification SEM images were taken from the regions marked with red to examine the wear traces in detail. As seen in Figure 5b, when a 1N load

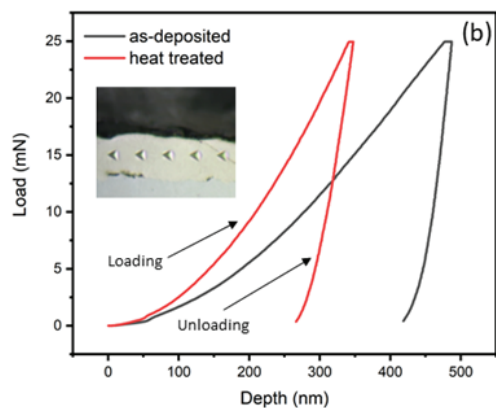
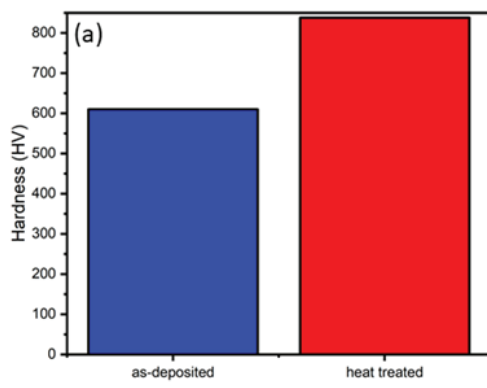


Figure 4. (a) Hardness and (b) load-depth curve for Ni-B alloy coatings as-deposited and heat treated.

is applied to the coating surface, the wear trace observed during the sliding indicates that the coating surface can bear the load. Since nickel is a ductile metal, the boron particles in the matrix are exposed and the load is reduced by the borides in contact with the hard surface. Nickel borides with lubricating properties protect the coating surface against the opposite surface. In addition, nickel crystal and nickel borides facilitate the plastic deformation of the coating. As shown in Figure 5d, when the applied load is increased to 3N, the roughness of the eroded surface has decreased. [16]. Columnar growth increases wear resistance by reducing the actual contact area of the coating. When the applied load is increased to 3N, high contact pressure caused by the increased load leads to an increase in temperature. Thus, the increased oxide layer increases wear resistance.

As seen in Figure 6, EDS analysis in wear traces shows that the Ni and O elements are present in the worn parts. 3N load sample has more O elements on the wear surface than other samples. Severe wear occurs by increasing the applied load to 5N and adhesive wear has occurred in the fragmentation of the wear trace. Since the protective oxide layer starts to break at 5N load and the crystal borides with lubricant properties do not resist sufficiently against the applied load,

the contact area between the coating surface and the opposite surface increases and resulting with high wear. The disruption of the adhesive-induced connection due to chemical interaction between the contact surface causes the formation of local debris particles [17]. As the contact interface temperature increases with increasing the load to 5N, the hardening of the matrix is reduced by the breakdown of the protective oxide layer. Thus, the contact of the load with the soft substrate material causes breaks in the material. Detection of the element Fe, which is the element of the substrate material in EDS analysis (Figure 6), confirms the cracks that occur in wear [18].

The friction coefficients and wear rates of Ni-B coatings abraded at different loads are given in Figure 7. Friction coefficients increased at the beginning of each coating due to surface roughness. Then progressed steadily throughout the wear test. As seen in the figure, the lowest friction coefficient and the lowest wear rate were observed in the abraded coating with 3N load. High volume nickel crystal and crystal borides increase the wear resistance of the coating. Nickel borides formed after heat treatment increase the hardness of the coating, thereby increasing the plastic resistance of the coating. The contact area between the coating surface and the opposing surface decreases

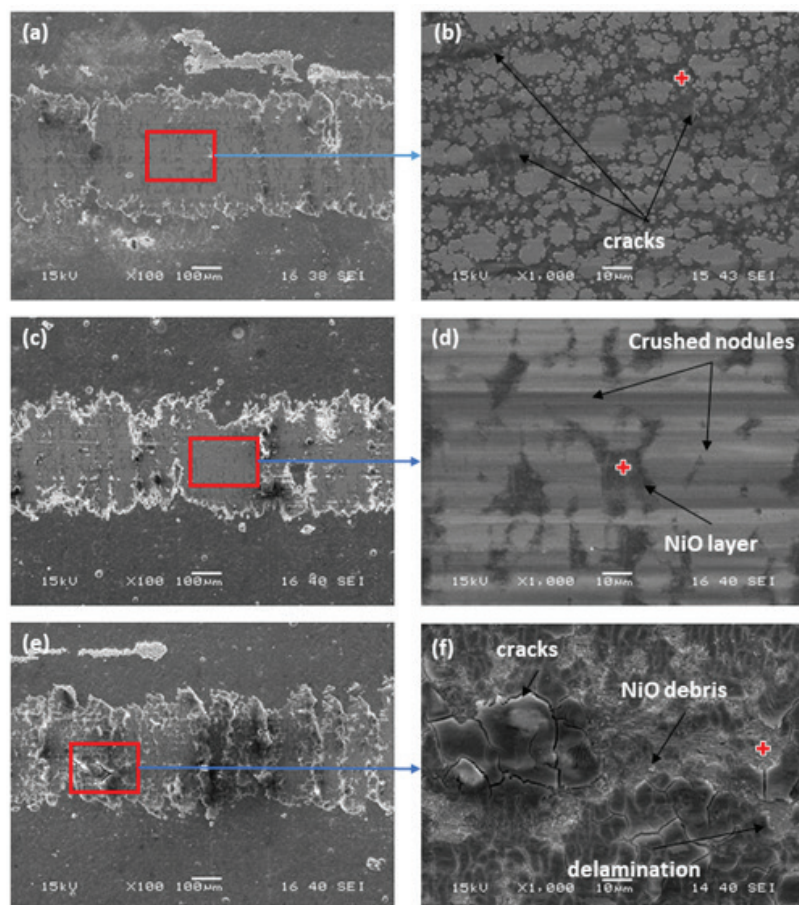


Figure 5. Low (a,c,e) and high (b,d,f) magnification SEM images of wear marks of Ni-B alloy coatings, which are formed as a result of friction tests performed under 1N, 3N and 5N load at room temperature, dry shear conditions, respectively.

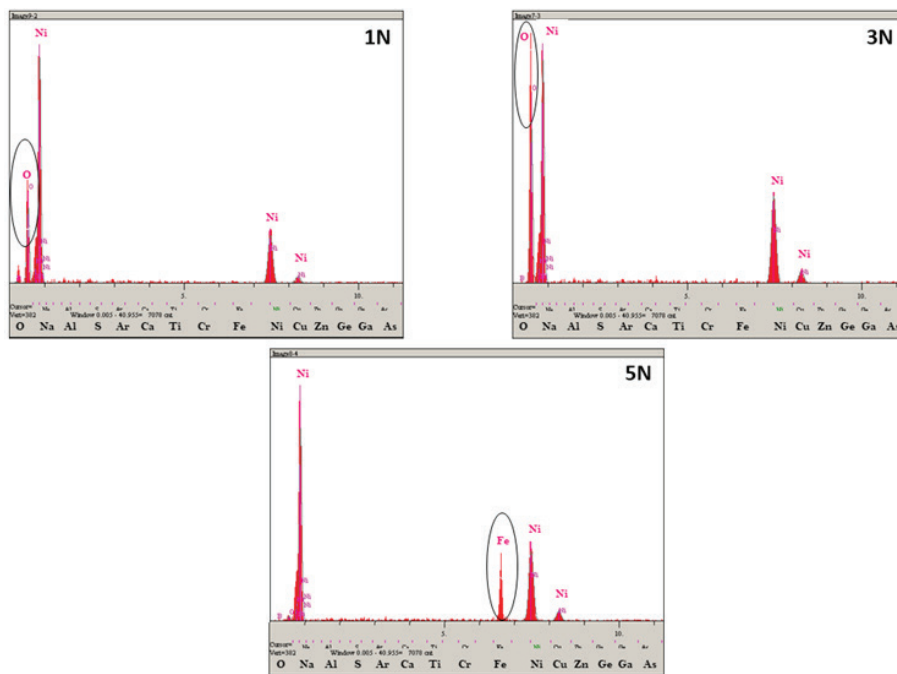


Figure 6. EDS analysis of worn surfaces at different loads, respectively.

and the friction coefficient value of the coating decreases. In addition, as described in Figure 6, the oxide layer formed on the coating surface plays an important role in reducing the contact area. As seen in the figure, when the load applied to Ni-B coatings is increased to 5N, the wear rate and friction coefficient increase due to friction force is more severe. Thus, increasing the load causes the protective tribo-oxide layer to break, cracks to form and increased friction. With the decrease of the plastic deformation in the contact area at 5N load, direct contact occurs between the coating surface and the opposite surface. Also, the volume of the nickel crystal and the presence of nickel boride phases in the adhesive wear mechanism affect the wear of the coating. Increasing the load causes the borides in the matrix to break and an increase in wear rate. Therefore, with increasing the applied load to 5N, because of the high adhesion between the coating surface and the opposite surface, the friction coefficient value of the coating increases [19].

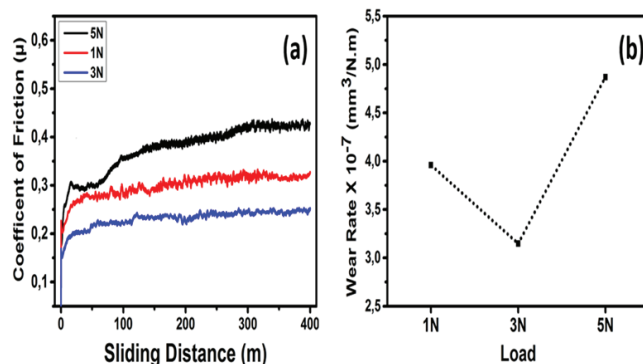


Figure 7. Coefficient of friction and wear rate of coatings abraded in different loads.

4. Conclusion

Electrodeposited Ni-B coatings were heat treated at 400°C for 1 hour. While nickel crystallized after heat treatment, the deposits in the precipitated state were observed to precipitate the Ni₃B and Ni₂B phases. The mechanical and tribological properties of Ni-B coatings have been improved by the precipitation of Ni₃B and Ni₂B crystals and formation of smaller grain size after heat treatment. The hardness of the coating increased significantly after heat treatment. Increased coating hardness has shown high wear resistance by reducing the contact area between the coating surface and the opposing surface. The increase in coating hardness in heat treated coatings increased the plastic resistance of the coating and reduced the contact area between the coating surface and the opposing surface. When the coating surface is worn with 3N load, the nickel borides and the Ni-O layer formed with the increasing temperature due to the contact pressure during wear increased the wear resistance. By increasing the applied load to 5N, the separations formed by the adhesive wear mechanism on the coating surface and the residual particles increased the wear rate and friction coefficient of the coating. The wear rate and coefficient of friction of coatings that was abraded at room temperature with different loads increased with increasing higher load.

Acknowledgement

This work has been supported by the Boron Research Institute (Grant No: 2017-31-07-25-001) and Scientific Research Projects Unit for the Sakarya University (Grant No. 2016-50-02-007), Turkey.

References

- [1] Dossett, J., & Totten, G. E. (Eds.). (2013). *Steel Heat Treating Fundamentals and Processes* (Vol. 4A), ASM International. <https://doi.org/10.31399/asm.hb.v04a.9781627081658>.
- [2] Wang, Y. M., Cheng, S., Wei, Q. M., Ma, E., Nieh, T. G., & Hamza, A. (2004). Effects of annealing and impurities on tensile properties of electrodeposited nanocrystalline Ni. *Scripta Materialia*, 51(11), 1023-1028.
- [3] Brooman, E. W. (2004). Wear behavior of environmentally acceptable alternatives to chromium coatings: Nickelbased candidates, *Metal Finishing*, 102(9), 75-82.
- [4] Krishnaveni, K., Narayanan, T. S., & Seshadri, S. K. (2005). Electroless Ni-B coatings: preparation and evaluation of hardness and wear resistance. *Surface and Coatings Technology*, 190(1), 115-121.
- [5] Pal, S., Sarkar, R., & Jayaram, V. (2018). Characterization of thermal stability and high-temperature tribological behavior of electroless Ni-B coating. *Metallurgical and Materials Transactions A*, 49(8), 3217-3236.
- [6] Bhushan, B. (2000). *Modern Tribology Handbook, Two Volume Set* (1st ed.). CRC Press. <https://doi.org/10.1201/9780849377877>.
- [7] Ahmadiyeh, S., Rasooli, A., & Hosseini, M. G. (2020). Preparation of pulse electrodeposited Ni-B coating with RSM software and evaluation of its microhardness and electrochemical behavior. *Metallurgical and Materials Transactions A*, 1-13.
- [8] Zhang, Z., Jiang, Y., Huang, L., Nie, X., & Liu, G. (2017). Experiment study of laser thermal enhanced electrochemical deposition. *Microsystem Technologies*, 23(6), 1695-1701.
- [9] Xiao, Q. L., Shao, S. Y., Shao, J. D., & Fan, X. Z. (2009). Influences of oxygen partial pressure and deposition rate on residual stress of YSZ thin films. *Chinese Journal of Lasers*, 36, 1195-1199.
- [10] Teppa, O., & Taskinen, P. (1993). Thermodynamic assessment of Ni-B phase diagram. *Materials Science and Technology*, 9(3), 205-212.
- [11] Delaunois, F., & Lienard, P. (2002). Heat treatments for electroless nickel-boron plating on aluminium alloys. *Surface and Coatings Technology*, 160(2-3), 239-248.
- [12] Patterson, A. L. (1939). The Scherrer formula for X-ray particle size determination. *Physical Review*, 56(10), 978-982.
- [13] Liu, B., Wang, B., & Gu, J. (2019). Effect of ammonia addition on microstructure and wear performance of carbonitrided high carbon bearing steel AISI 52100. *Surface and Coatings Technology*, 361, 112-118.
- [14] Sahoo, P., & Das, S. K. (2011). Tribology of electroless nickel coatings-a review. *Materials & Design*, 32(4), 1760-1775.
- [15] Kanta, A. F., Vitry, V., & Delaunois, F. (2009). Wear and corrosion resistance behaviours of autocatalytic electroless plating. *Journal of Alloys and Compounds*, 486(1-2), L21-L23.
- [16] Cao, Z. Q., Sun, Y., & Sun, H. J. (2012). Effect of grain size on oxidation behavior of Fe-40Ni-15Cr alloys. *High Temperature Materials and Processes*, 31(1), 83-87.
- [17] Chen, L. H., & Rigney, D. A. (1990). Adhesion theories of transfer and wear during sliding of metals. *Wear*, 136(2), 223-235.
- [18] Holmberg, K., & Matthews, A. (2009). *Coatings tribology: Properties, mechanisms, techniques and applications in surface engineering*. Elsevier. <https://doi.org/10.1088/0022-3727/40/18/S07>.
- [19] Pal, S., & Jayaram, V. (2018). Effect of microstructure on the hardness and dry sliding behavior of electroless Ni-B coating. *Materialia*, 4, 47-64.



Ni-B katalizörün hidrojen üretiminde yanıt yüzey yöntemi ile optimizasyonu

Hüseyin Elçiçek*

Sakarya Uygulamalı Bilimler Üniversitesi, Denizcilik Meslek Yüksekokulu, Sakarya, 54800, Türkiye,
ORCID orcid.org/0000-0003-1064-6668

MAKALE BİLGİSİ

Makale Geçmişi:
İlk gönderi 12 Kasım 2020
Kabul 1 Ocak 2021
Online 31 Mart 2021

Araştırma Makalesi

DOI: 10.30728/boron.825013

Anahtar kelimeler:
Hidrojen
Ni-B katalizörü
Taguchi
Yanıt yüzey yöntemi

ÖZET

Son günlerde yaşanan COVID-19 salgını, temiz ve yenilenebilir enerji kaynaklarının kullanımının ne derece önemini birkez daha göstermiştir. Bu çalışmada, geleceğin enerji kaynağı olarak düşünülen temiz hidrojen, Ni-B katalizörleri kullanılarak NaBH_4 'ün hidrolizi ile üretilmiştir. Hidroliz reaksiyonu esnasında reaksiyon kinetikine doğrudan etkisinin olduğu bilinen ortam sıcaklığı, karıştırma hızı, katı-sıvı oranı ve kullanılan yakıtta $\text{NaBH}_4\text{-NaOH}$ oranı gibi parametrelerin reaksiyon hızına olan etkileri yanıt yüzey metodu ile ayrıntılı olarak incelenmiştir. Kullanılan yanıt yüzey metodunda deneysel çalışmalar Taguchi L9 ortogonal dizisi kullanılarak gerçekleştirilmiş ve parametrelerin etkinliği varyans analizi ile belirlenmiştir. Oluşturulan model sonucunda, maksimum hidrojen üretim hızının eldesi için optimum parametreler; ortam sıcaklığı 347,17°C; karıştırma hızı 200,21 rpm; katı-sıvı oranı 2,86 mg_{catalyst}/ml_{yakıt}; ve $\text{NaBH}_4\text{-NaOH}$ oranı 1,04 olarak belirlenmiştir. Varyans analizine göre hidrojen üretim hızını etkileyen parametrelerin etkinliği sırasıyla reaksiyon sıcaklığı, karıştırma hızı ve $\text{NaBH}_4\text{-NaOH}$ oranı olarak belirlenmiştir. Buna karşılık katı-sıvı oranının etkisinin belirgin bir şekilde ortaya çıkmadığı görülmüştür. Yanıt yüzey yöntemi kullanılarak geliştirilen modelden elde edilen tahmin sonuçları ile deneysel verilerin birbirilerini doğruladığı, yapılan doğrulama deneyleri sonucunda ortaya konulmuştur.

Optimization of Ni-B catalyst with response surface methodology in hydrogen production

ARTICLE INFO

Article history:

Received November 12, 2020
Accepted January 1, 2021
Available online March 31, 2021

Research Article

DOI: 10.30728/boron.825013

Keywords:

Hydrogen
Ni-B catalyst
Taguchi
Response surface methodology

ABSTRACT

The COVID-19 pandemic shows once again how important the use of clean and renewable energy sources is. In this study, clean hydrogen, which is considered as the energy source of the future, was produced by the hydrolysis of NaBH_4 using Ni-B catalysts. During the hydrolysis reaction, the effects of parameters such as reaction temperature, stirring speed, solid-liquid ratio and $\text{NaBH}_4\text{-NaOH}$ ratio in the fuel used, which are known to have a direct effect on the reaction kinetics, on the reaction rate were studied in detail by the response surface methodology. Experimental studies in the response surface methodology used were carried out using the Taguchi L9 orthogonal array and the efficiency of the parameters was determined by analysis of variance. As a result of the created model, optimum parameters for obtaining the maximum hydrogen production rate; reaction temperature 347.17°C; stirring speed 200.21 rpm; solid-liquid ratio 2.86 mg_{catalyst}/ml_{yakıt}; and the ratio of $\text{NaBH}_4\text{-NaOH}$ 1.04. According to the analysis of variance, the efficiency of the parameters affecting the hydrogen generation rate was determined as reaction temperature, stirring speed and $\text{NaBH}_4\text{-NaOH}$ ratio, respectively. On the other hand, it has been seen that the effect of solid-liquid ratio does not appear clearly. As a result of the validation tests, it was revealed that the predictions obtained from the model developed using the response surface methodology are in good agreement with the experimental results.

1. Giriş (Introduction)

Dünya nüfusunun hızlı artışı ve artan enerji talebinin yanı sıra şehirlerin plansız bir şekilde büyümesi ile birlikte çok sayıda çevre sorununa ve insan sağlığı için ciddi risklere neden olmaktadır. Hızla artan hava kirli-

lığı, küresel ölçekte toplum sağlığı ve çevre için ciddi bir tehdit oluşturmaktadır. Yapılan araştırmalar sonucunda ciddi hastalıkların oluşmasına neden olan hava kirliliği ile solunum hastalığı semptomları, akciğer yetmezliği, kronik bronşit ve solunum problemlerine bağlı ölüm sayıları arasında doğrudan bir ilişki olduğunu

*Sorumlu yazar: helcicek@subu.edu.tr

doğrulamıştır. Bununla birlikte, Dünya Sağlık Örgütü (WHO) hava kirliliğinin kanserinin temel nedenlerinden biri olarak bildirmiştir [1,2]. Son zamanlarda hızla artış gösteren yeni tip koronavirüs (COVID-19) pandemi süreci, özellikle kronik hastalıkları bulunan kişilerin, COVID-19 enfeksiyonuna yakalanma riski ve hasta üzerindeki olumsuz etkisi artmaktadır. Pandemi süreci, insanın temiz su, hava ve enerji ihtiyacını gün yüzüne çıkarmış ve bu yönde atılacak adımların sürdürülebilirliği ve iyileştirilmesi hayatı önem taşımaktadır [3]. Ekonomik ve çevresel kaygılar, bununla birlikte fosil yakıtlara bağımlılığın azaltılması ve doğaya salınan zararlı emisyonların en aza indirilmesi sürdürülebilir alternatif enerji kaynakları ile sağlanabilecektir [4]. Günümüzde fosil kaynaklı yakıtlara alternatif olarak, yüksek verimliliği ve çevre dostu olması nedeniyle hidrojen, umut verici bir enerji kaynağı olarak ve geleceğin yakımı kabul edilmektedir [5-8]. Bununla birlikte, güvenli, verimli ve düşük maliyetli hidrojen üretiminin henüz sağlanamaması nedeniyle, hidrojen yaygın olarak kullanılmamaktadır. Hidrojen kaynağı olarak birçok farklı araştırma gerçekleştirilmiş olup, su, doğalgaz, kömür, çeşitli bitkiler ve kimyasal hidrürler gibi birçok farklı malzemenin verimliliği araştırılmıştır. Kimyasal hidrürler (LiBH_4 , NaBH_4 , KBH_4 , NaH , vb.) hacimsel olarak yüksek hidrojen depolama yoğunluğuna sahip olması nedeniyle taşınabilir uygulamalar için en umut verici depolama kaynakları arasında yer almaktadır [9,10]. Özellikle sodyum borhidrür (NaBH_4), yüksek teorik hidrojen içeriği (%10,8 kütlece), kararlı yapısı, düşük sıcaklıklarda hidroliz yoluyla hidrojen üretiminin gerçekleşmesi, reaksiyon sonrasında toksik olmayan yan ürünlerin ortaya çıkması ve uygun katalizör varlığında hidroliz reaksiyonunun kolaylıkla kontrol edilebilmesi nedeniyle hidrojen üretiminde yaygın olarak kullanılmaktadır. Bununla birlikte, uygun katalizör seçimi, üretilen hidrojenin saflığını ve verimliliğini önemli ölçüde etkilemektedir [11]. Literatürde, Co-B bazlı katalizörler, düşük maliyetleri, yüksek aktiviteleri ve yeniden kullanılabilirlikleri nedeniyle NaBH_4 hidrolizi yoluyla hidrojen üretiminde tercih edilmekte ve etkileri kapsamlı bir şekilde araştırılmıştır [9,12-14]. NaBH_4 'ün genel hidroliz reaksiyonu şu şekilde tanımlanmaktadır:



NaBH_4 'ün kütlece %10,8 hidrojen içerirken, hidroliz reaksiyonunda (suyun da katkısıyla) normal şartlar altında 1 g NaBH_4 ile 2,37 L hidrojen üretilmektedir. NaBH_4 'ün oda sıcaklığında kendi kendine hidroliz reaksiyonu ile toplam dönüşümü %7-8 civarında gerçekleşmektedir [15,16] ve su içerisindeki reaksiyonu ekzotermiktir. Reaksiyon sonucunda ortaya çıkan sodyum metaborat (NaBO_2) çevreye zararsız bir ürün olarak oluşmakta ve tekrar NaBH_4 'e dönüştürülebilmektedir [17]. Hidroliz reaksiyonun hızını ve verimliliğini artırmak için asidik ve metalik katalizörler literatürde sıkça kullanılmaktadır [18]. Bununla birlikte, sodyum borhidrür çözeltisinin raf ömrünü uzatmak ve bekletil-

diginde açığa çıkan hidrojen gazını önlemek amacıyla çözelti içerisinde sodyum hidroksit (NaOH) gibi bazik çözeltiler eklenerken alkali çözeltileri halinde depolana bilmektedir. NaBH_4 ve NaOH konsantrasyonunun yanı sıra, katalizör türü, katalizör miktarı, karıştırma hızı ve reaksiyon sıcaklığı gibi birçok parametre hidroliz kinetiği üzerinde önemli etkileri bulunmaktadır.

NaBH_4 'ün hidroliz reaksiyonunda platin (Pt) [19], rutenyum (Ru) [20] ve paladyum (Pd) [21] bazlı katalizörler yaygın olarak kullanılmaktadır. Bu katalizörler, yüksek aktivite göstergelerine rağmen, yüksek maliyetleri nedeniyle geniş çaplı uygulamalarda kullanımlarını sınırlamaktadır [22]. Son zamanlarda yapılan çalışmalarla düşük maliyetli, dayanıklı, ve verimli alternatifler bulma ihtiyacından dolayı, kobalt (Co) [23], nikel (Ni) [24], manganez (Mn) [25] ve bakır (Cu) [26] gibi geçiş metalleri birçok çalışmada tercih edilmiştir. Bu металer içerisinde nikel, yüksek aktivite göstermesi, seçici ve ucuz olması nedeniyle en çok tercih edilen metaller arasında yer almaktadır [27]. Nikel bazlı katalizörlerin kullanımı 2000'li yılların ilk yarısına uzanmaktadır. Hua vd. (2003) aktif bir nikel borid (Ni_xB) katalizörü kullanarak NaBH_4 'ün hidrolizi ile hidrojen üretim verimini ve hızını farklı NaOH konsantrasyonlarında ve sıcaklık değerlerinde incelenmiştir. Elde edilen sonuçdan, Ni_xB katalizörünün 150°C'de vakum altında ıslı işleme tabi tutulması sonucunda katalitik aktivitesinin ve stabilitesinin önemli ölçüde iyileşme gösterdiği bulunmuştur. Çalışma koşullarında, hidroliz reaksiyonu 45°C'de kütlece %6,75 hidrojen üretimi gerçekleşken, oda sıcaklığında bu oran kütlece %4,0 olarak rapor edilmiştir [28]. Lee vd. (2019) grafen destekli Ni katalizörü kullanarak hidrojen üretimi incelemiştir. Çalışma sonucunda, maksimum hidren üretim hızının 600-800 ml.dk⁻¹.g⁻¹ olduğu ve reaksiyon kinetiğinin birinci dereceden olduğu bulunmuştur [29]. Ghodke vd. (2020) termal plazma yoluyla sentezlendikleri nikel nanopartiküllerini kullanarak, NaBH_4 başlangıç konsantrasyonu, pH ve çözelti sıcaklığının hidrojen üretim hizina (HGR) etkisini incelemiştir. Maksimum hidrojen üretimi hızı 320°K sıcaklığında 1000 ml.dk⁻¹.g⁻¹ katalizör olarak bulunmuştur. Ni nanopartiküllerinin hidroliz reaksiyon kinetiği incelendiğinde, 305-315°K sıcaklık aralığında birinci dereceden, 300°K sıcaklığında ise sıfırıncı dereceden reaksiyon kinetiği rapor edilmiştir. Bununla birlikte, birinci dereceden reaksiyon kinetiğine göre hesaplanan aktivasyon enerjisi 69,76 kJ/mol iken aktivasyon entalpisi 67,18 kJ/mol olarak bulunmuştur [30]. Son zamanlarda yapılan çalışmalar incelendiğinde hidroliz yöntemi ile hidrojen üretiminin verimliliğini, sıcaklık, NaOH ve NaBH_4 miktarı, karıştırma hızı ve katalizör miktarı-yakıt oranı gibi parametreler önemli ölçüde etkilemektedir. Aydin vd. (2016) yapmış oldukları çalışmada Co-Ti-B katalizörünü kullanarak çözelti sıcaklığı, NaBH_4 , NaOH ve (Ti) konsantrasyonunun hidrojen üretim hızı üzerine etkilerini araştırmışlardır. Araştırmacılar, deneysel çalışmalar sonucunda %5 Ti/(Ti-Co) molar oranında en yüksek hidrojen üretim

oranına ulaşırken bu katalizör için optimum yakıt kon-
santrasyonu kütlece %5 NaOH ile %5 NaBH₄ olarak
bulunmuştur [9]. Saka vd. (2015) tarafından yapılan
çalışmada, Cu-Co destekli katalizör kullanılarak sod-
yum borhidrür çözeltisinin hidroliz reaksiyonundan
hidrojen üretiminin verimliliği farklı Cu-Co oranlarında
araştırılmıştır. Deneysel sonuçlar, Cu-Co katali-
zörünün optimal karışım yüzdesinin 60:40 olduğunu,
bununla birlikte Cu oranının aşırı artması sonucunda
katalitik aktivitenin önemli ölçüde kötüleştiğini gös-
termişlerdir [31]. Ekinci vd. (2020) hidrojen üretimi için
mikrodalga fırın içerisinde Ni-B katalizörü kullanılarak
gerçekleştirilmiştir. Araştırmacılar, Ni-B katalizörünün
katalitik aktivesini, NaOH ve NaBH₄ konsantrasyonu,
katalizör miktarı, mikrodalga sıcaklığı ve gücü gibi pa-
rametrelerini dikkate alarak incelemiştir. Deneyle
hem mikrodalgasız hem de mikrodalga kullanılarak
Ni-B katalizör ile yapılmış ve mikrodalga kullanımı so-
nucunda maksimum hidrojen üretiminin elde edildiği
belirtilmiştir [32]. Literatür çalışmalarından da açıkça
gördüğü gibi birçok parametre hidrojen üretiminde
etkili olmaktadır. Etkin parametrelerin doğru metotlar
kullanılarak optimize edilmesiyle, hem deneysel çalış-
malarda ortaya çıkan maliyet hem de deney süreleri
önemli ölçüde azalacaktır. Optimizasyon süreci için
çeşitli teknikler kullanılmakla birlikte Yanıt yüzey yon-
temi (RSM) ve Taguchi metodu yaygın olarak tercih
edilmektedir. RSM metodunda proses değişkenlerinin
çıktı üzerine etkisini ve bununla birlikte parametreler
arası etkileşimleri dikkate alınarak, oluşturulan deney
plani ile proses optimizasyonu gerçekleştirilmektedir.
RSM kontrol edilebilir deneysel parametreler ve çik-
tılardı arasındaki ilişkinin değerlendirilmesi için bir am-
pirik modelin oluşturulması esasına dayanmaktadır.
Ortaya çıkan empirik ifade proses performans çıktıları
ile (bağımlı değişken) prosese etki eden parametreler
(bağımsız değişkenler) arasındaki ilişkiyi tanımlamak-
tedir. Sıklıkla kullanılan bir diğer optimizasyon yöntemi
ise Taguchi metodudur. Taguchi optimizasyon metodu
minimum deney ile, kontrol edilebilen ve kontrol edi-
lemyen parametrelerin çıktı üzerine olan etkilerini
belirleyebilmek için kullanılan en önemli optimizasyon
yöntemlerinden biridir. Bu metot ile birlikte, zaman,
para ve deney malzemelerinin ekonomik bir şekilde
kullanarak kalitekarakteristğini etkileyen en önem-
li değişkenleri bulmak hedeflenmektedir. Kazıcı vd.
(2020) tarafından yapılan çalışmada, aktif karbon (AC)
destekli palladyum, kobalt ve gümüş nano parçacık
(PdCoAg/AC) katalizörünü kullanarak amonyak boran
(NH₃BH₃) ile hidrojen (H₂) üretiminin optimizasyonunu
yanıt yüzey metodolojisi kullanılarak araştırılmışlardır.
Araştırmacılar maksimum hidrojen üretiminin (11414,4
ml.dk⁻¹.g⁻¹), 2,55 mmol/5 mL NH₃BH₃ konsantrasyonu,
15,50 mg katalizör miktarı ve 50°C sıcaklık şartlarında
elde etmişlerdir [33]. Özkan vd. (2019) yanıt yüzey
yöntemini kullanarak Box-Wilson metodu ile HCl kon-
santrasyonu ve sıcaklığın hidrojen üretimi üzerine etki-
lerini araştırmışlardır. Araştırmacılar, HCl konsantrasyonu
ve sıcaklığın hidrojen üretimi üzerine etkilerini araştırmışlardır.

yonunun hidrojen üretimi üzerindeki etkisinin, sıcaklığı göre daha etkili olduğunu belirtmişlerdir. Bununla birlikte, en yüksek dehidrojenasyon verimi (%100) 3,76 M HCl konsantrasyonunda ve sıcaklık 157°C'de ve bu koşullar altında mininum reaksiyon süresi elde edilmiştir [34]. Bu çalışmalara ilave olarak, proton değişim membran (PEM) yakıt hücrelerinde proses verimliliğini artırmak ve parametrelerin optimizasyonunu yapmak amacıyla Taguchi metodu yaygın olarak kullanılmaktadır [35,36].

Hidrojen üretiminde alkali NaBH_4 çözeltisinin hidroliz tepkimesini hızlandırmak için kullanılan katalizörlerin yanı sıra hidroliz reaksiyonunu etkileyen parametrelerin reaksiyon hızı üzerine etkilerinin araştırılması büyük önem taşımaktadır. Ayrıca uygun deney tasarım modellerinin kullanılması ile laboratuvar çalışmalarında harcanan zaman ve maliyet minimize edilecektir. Bu çalışmada, Ni-B katalizörü ile hidrojen üretimini maksimize etmek amacıyla yanıt yüzey yöntemi kullanılarak sıcaklık, karıştırma hızı, katı-sıvı oranı ve $\text{NaBH}_4\text{-NaOH}$ oranı parametrelerinin hidroliz reaksiyonu üzerine etkileri araştırılmıştır. Deneysel çalışmalar Taguchi L9 ortogonal deneysel tasarım modeli kullanılarak gerçekleştirilmiş ve parametrelerin etkinliği ve birbiri arasındaki etkileşim varyans analizi (ANOVA) kullanılarak belirlenmiştir. Bu çalışmada elde edilen sonuçlar, Ni-B katalizörü kullanılarak farklı çalışma koşulları altında gerçekleştirilen prosesler için hidrojen üretiminin optimum koşulların belirlenmesine katkı sağlayacaktır.

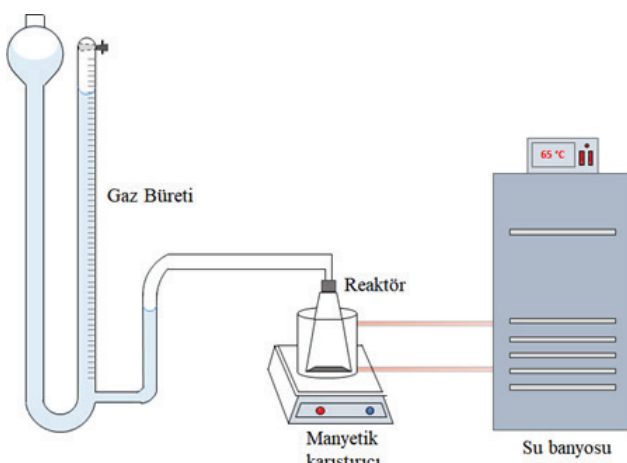
2. Malzemeler ve Yöntemler (Materials and Methods)

2.1. Katalizör Sentezi (Catalyst Synthesis)

Deneysel çalışmalarında kullanılan nikel(II)klorür hekzahidrat ($\text{NiCl}_2 \cdot 6\text{H}_2\text{O}$), sodyum hidroksit (NaOH), etanol ($\text{CH}_3\text{CH}_2\text{OH}$) ve sodyum borhidrür (NaBH_4 , %95) çözeltileri Sigma Aldrich'ten temin edilmiştir. İlk olarak 0,02M $\text{NiCl}_2 \cdot 6\text{H}_2\text{O}$ ve 50 ml etanol oda sıcaklığında homojen karışım elde edilene kadar (~10 dk) karıştırılmıştır. Hazırlanan tüm çözeltilerin indirgenme reaksiyonu öncesinde pH değerleri kaydedilmiştir. Daha sonra elde edilen karışım, 6°C ayarlanmış olan termostatlı ve sirkülasyonlu bir su banyosu içerisinde manyetik karıştırıcı yardımı ile 500 rpm hızında karıştırılmıştır. Su banyosu içerisinde bulunan çözeltinin sıcaklığı 80°C'ye ulaştığında, indirgeyici olarak 500 mg NaBH_4 ve 10 ml su karışımı çözelti içerisinde şırınga pompası ile 5 ml/dk hızında enjekte edilmiştir. Elde edilen siyah çökelti, su ve etanol ile yıkarak santrifüjle sıvıdan ayrılmıştır. Yıkama işlemi sonucunda çöktürülen partiküller vakum altında 110°C'de 1 saat süreyle kurutulmuştur. Daha sonra katalizör içerisindeki nemı uzaklaştırmak için kurutma işlemine 110°C sıcaklığında devam edilmiş ve katalizör kurutulduktan sonra havanda örtülmüştür.

2.2. Katalizör Performans Testi (Catalytic Performance Test)

Hazırlanan Ni-B katalizörü içeresine deneysel tasarım modelinde belirtilen oranlarda hazırlanan yakıt ilave edilerek hidrojen üretim hızı (HGR) su hacminin değişim yöntemi ile belirlenmiştir [9]. Hazırlanan katalizör Tablo 2'de verilen oranlarda tartılarak, balon joje içeresine alınmış ve üzerine taze hazırlanmış yakıt çözeltisi ilave edilmiştir. Su banyosu belirlenen sıcaklıkta ulaştığında yakıt ilavesi ile birlikte deneysel başlatılmıştır. Üretilen hidrojen gazının hacmindeki değişiklik 1 dakikalık aralıklarla kaydedilmiştir. HGR, kullanılan toplam katalizör miktarına göre belirlenmiştir. HGR ölçümlerini gerçekleştirebilmek amacıyla çalışmalarında kullanılan deney düzeneğinin şematik gösterimi Şekil 1'de verilmiştir.



Şekil 1. Hidrojen üretim düzeneğinin şematik gösterimi (Schematic representation of the hydrogen generation setup).

2.3. Deney Tasarımı (Experimental Design)

Bu çalışmada, Ni-B katalizörü kullanılmış olup hidrojen üretimini maksimize etmek amacıyla L9 Taguchi ortogonal dizisi kullanılmıştır. Çalışmada dört bağımsız parametre kullanılmış olup, bu parametrelerin aralıkları reaksiyon sıcaklığı (328-348°K), karıştırma hızı (200-600 rpm), katı-sıvı oranı ($1-3 \text{ mg}_{\text{katalizör}}/\text{ml}_{\text{yakıt}}$) ve $\text{NaBH}_4\text{-NaOH}$ (1-3) şeklinde dir. Deneysel çalışmalarında kullanılan parametreler, bu parametrelerin seviyeleri ve değerleri Tablo 1'de ve L9 Taguchi ortogonal deney planı Tablo 2'de verilmiştir.

Taguchi, deney planında performans ölçütü olarak sinyal-gürültü (SN) oranının kullanılmasının gerekliliğini de ileri sürmüştür ve yapmış olduğu çalışmalarında yetmişten fazla SN oranı geliştirmesine rağmen, literatürde sıkılıkla; hedef değer en iyi, en küçük en iyi ve en büyük en iyi SN oranları kullanılmaktadır. Bu çalışmada üretilen hidrojenin maksimize etmek amacıyla en büyük en iyi SN oranı kullanılmış olup, matematiksel ifade denklemi aşağıda verilmiştir.

$$SN = -10 \log \left[\frac{1}{n} \sum_{i=1}^n \frac{1}{y_i^2} \right] \quad (1)$$

Taguchi deney tasarım yöntemi basitliği ve kullanım kolaylığı nedeniyle birçok mühendislik ve endüstriyel uygulamada kullanılmaktadır. Bununla birlikte, deney tasarım planının kullanılması ile ürün geliştirme maliyetleri düşmektedir, ürünün piyasaya sürülmeye süresi azalmaktır ve üretkenlik önemli ölçüde artmaktadır. Örneğin, bu çalışmada 4 parametreli ve 4 seviyeli bir çalışmayı gerçekleştirmek için 256 (4^4) deney yapmak

Tablo 1. Deneysel çalışmalarında kullanılan parametreler ve seviyeleri (Parameters and levels used in experimental studies).

Parametre	Birim	Seviye		
		1	2	3
A Sıcaklık	°K	338	328	348
B Karıştırma Hızı	rpm	200	400	600
C Katı-Sıvı Oranı	$\text{mg}_{\text{katalizör}}/\text{ml}_{\text{yakıt}}$	1	2	3
D $\text{NaBH}_4\text{-NaOH}$ oranı		1	2	3

Tablo 2. L9 Ortogonal dizisi ait deney planı ve sonuçlar (Experimental design of L9 orthogonal array and responses).

Deney No.	Sıcaklık	Karıştırma Hızı	Katı-Sıvı Oranı	$\text{NaBH}_4\text{-NaOH}$ Oranı	HGR
1	338	200	1	1	2,41
2	338	400	2	2	2,25
3	338	600	3	3	1,99
4	328	200	2	3	0,98
5	328	400	3	1	1,32
6	328	600	1	2	1,08
7	348	200	3	2	3,13
8	348	400	1	3	2,65
9	348	600	2	1	2,76

gerekirken, Taguchi metodunun kullanılması ile 9 deney yaparak, parametrelerin optimizasyonu yapılabilmektedir. Aynı zamanda hidrojen üretim parametrelerini etkileyen her bir girdi değişkeninin katkısı ANOVA teknigi kullanılarak belirlenmiştir. ANOVA tekniginde parametrelerin çıktı üzerindeki etkileri genellikle F oranı ile belirlenir ve F oranı ne kadar yüksekse parametrenin etkinliği o kadar önemli olduğu kabul edilir.

Yanıt yüzey yöntemi (RSM), girdi parametrelerinin çıktı üzerindeki etkilerinin incelendiği ve çıktıyı optimize etmeye çalıştığı uygulamaları modelllemek ve değerlendirmek için kullanılan istatistiksel bir yöntemdir. Yanıt yüzey yöntemi tipik olarak, deneysel tasarım matrisinin geliştirilmesi, çıktı fonksiyonunun oluşturulması ve çıktıının optimizasyonu için optimum parametre seviyelerinin belirlenmesi olarak özetlenen üç aşamadan oluşur. RSM genellikle çıktıının giriş parametreleri üzerindeki etkilerini ilişkilendirmek için ikinci dereceden bir polinom kullanır. Bu eşitlik Denklem 3'de verilmiştir.

$$Y = \beta_0 + \sum_{i=1}^n \beta_i X_i + \sum_{i=1}^n \beta_{ii} X_i^2 + \sum_{i < j} \beta_{ij} X_i X_j + \varepsilon \quad (2)$$

Denklemde, Y çıktıyı, X girdi değişkenlerini (parametrelere), XX çarpımları değişkenler arasındaki etkileşimleri; β katsayıları model parametrelerini, ε ise hata terimini göstermektedir.

3. Sonuçlar ve Tartışma (Results and Discussion)

Bu çalışmada sodyum borhidrürün hidrolizi için Ni-B katalizörlerinin kullanıldığı deney düzeneğinin optimizasyonu; reaksiyon sıcaklığı, karıştırma hızı, katı-sıvı oranı ve $\text{NaBH}_4\text{-NaOH}$ oranı parametreleri dikkate alınarak gerçekleştirılmıştır. Optimizasyon işlemlerinde Taguchi L9 ortogonal dizisi kullanılmış olup, çalışma koşulları içinde maksimum hidrojen üretim oranını belirlemek için yanıt yüzey metodu ile matematiksel eşitlik elde edilmiştir. Deneysel çalışma planı ve elde edilen hidrojen üretim hızı (HGR) değerleri Tablo 2'de

verilmiştir. Çalışmada etkileri araştırılan dört bağımsız parametre ve bu parametrelerin hidrojen üretimi üzerindeki etkileri aşağıda verilen kodlanmış değişkenler cinsinden ikinci dereceden matematiksel eşitlik ile ifade edilmiştir.

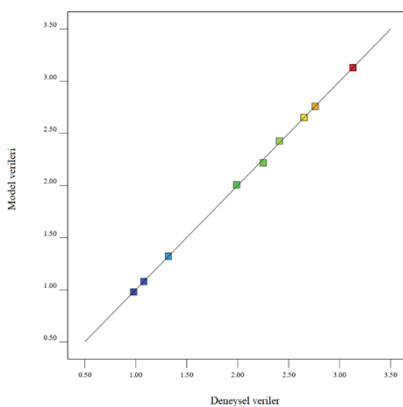
$$\begin{aligned} HGR = & 2,22 + 0,86A - 0,12B + 0,05C \\ & - 0,15D - 0,12AB - 0,23A^2 \end{aligned} \quad (3)$$

Model denklemde parametrelerin önünde yer alan pozitif veya negatif işaretler, sırasıyla sinerjik ve antagonistik etkiye göstermektedir [37,38]. Denklemde açıkça görüldüğü gibi, parametrelerin birbirleri arasındaki etkileşimler de görülmektedir. Reaksiyon sıcaklığı ve karıştırma hızının bileşik etkisinin hidrojen üretim hızı üzerinde negatif bir etkiye sahip olduğu görülmektedir. Oluşturulan modelde her bir parametrenin kapsamlı olarak anlamlılığı varyans analizi (ANOVA) kullanılarak incelenmiştir. Bağımsız girdi parametrelerinin çıktı parametresi üzerindeki etkileşimleri Tablo 3'de verilmiştir. Her bir parametrenin değişkenliği F testi kullanılarak grup bulgularının değişkenliği ile karşılaştırılmıştır. F değerinin büyülüğu girdi parametrelerinin değişimin çıktı parametresi üzerinde etkisini göstermektedir. ANOVA analizinde modelin F değeri 959,3 olarak bulunmuş olup bu değer modelin önemini olduğunu göstermektedir. Bununla birlikte parametrelerin çıktı üzerindeki etkinliğini gösteren bir diğer göstergesi, p-değeri'dir. 0,05'ten küçük p değerleri karşılık gelen parametrelerin çıktı üzerinde önemli bir etkiye sahip olduğunu ve anlamsız model terimlerinin modelden çıkarılabilceğini gösterir. ANOVA sonuçları, A, B, D, AB ve A^2 parametrelerinin önemli model terimleri olduğunu göstermektedir (p -değeri $<0,0500$). Geliştirilen modele ait korelasyon katsayısı (R^2) 0,9997 ve ayarlanmış korelasyon katsayısı (Adj-R^2) 0,9986 olarak bulunmuştur. Modele ait korelasyon katsayılarının 1'e yakın olması, ortaya konulan modelin hidrojen üretimi ni tahmin etmede başarılı olduğunu ve aynı zamanda

Tablo 3. Deneysel çalışmalarında kullanılan parametreler ve seviyeleri (Analysis of variance for hydrogen generation rate).

Parametreler	SS	df	MS	F-değeri	p-değeri
Model	4,82	6	0,8032	959,03	0,0010
A-Sıcaklık	4,44	1	4,44	5298,63	0,0002
B-Karıştırma Hızı	0,0794	1	0,0794	94,75	0,0104
C-Katı-Sıvı Oranı	0,0150	1	0,0150	17,91	0,0516
D-NaBH₄-NaOH oranı	0,1261	1	0,1261	150,63	0,0066
AB	0,0552	1	0,0552	65,94	0,0148
A²	0,1058	1	0,1058	126,33	0,0078
Artık	0,0017	2	0,0008		
Toplam	4,82	8			
R²	0,9997				
Adj-R²	0,9986				
Pred- R²	0,9952				

deneysel verilerle model verilerinin uyumluluğunu göstermektedir. ANOVA sonuçlarına göre her bir parametre incelendiğinde, parametrelerin etkinliği sırasıyla, reaksiyon sıcaklığı, $\text{NaBH}_4\text{-NaOH}$ oranı ve karıştırma hızı olarak bulunmuştur ve reaksiyon sıcaklığının kare değerinin ve reaksiyon sıcaklığı ile karıştırma hızının bileşik etkisinin HGR üzerinde önemli bir etkiye sahip olduğu da gösterilmiştir ($p < 0,05$). Hidrojen üretim hızının modelden elde edilen verilerle karşılaştırma grafiği Şekil 2'de gösterilmiştir.

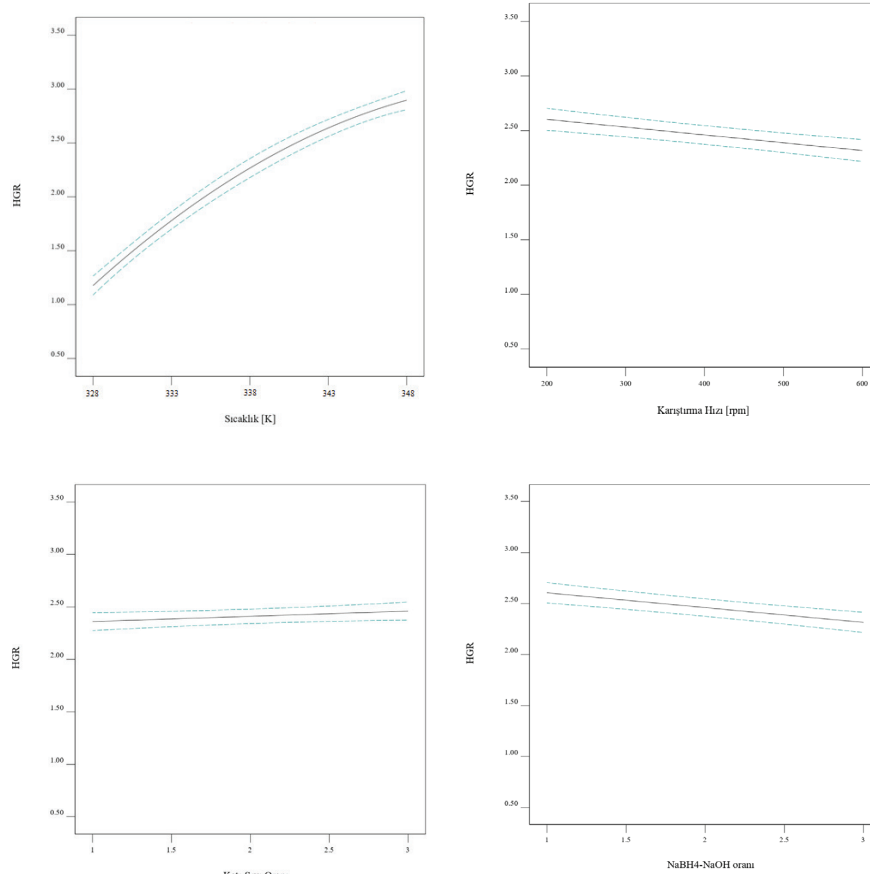


Şekil 2. Hidrojen üretim hızı tahmin edilen verilerle deneySEL verilerin karşılaştırılması (Predicted versus experimental values plot for hydrogen generation rate).

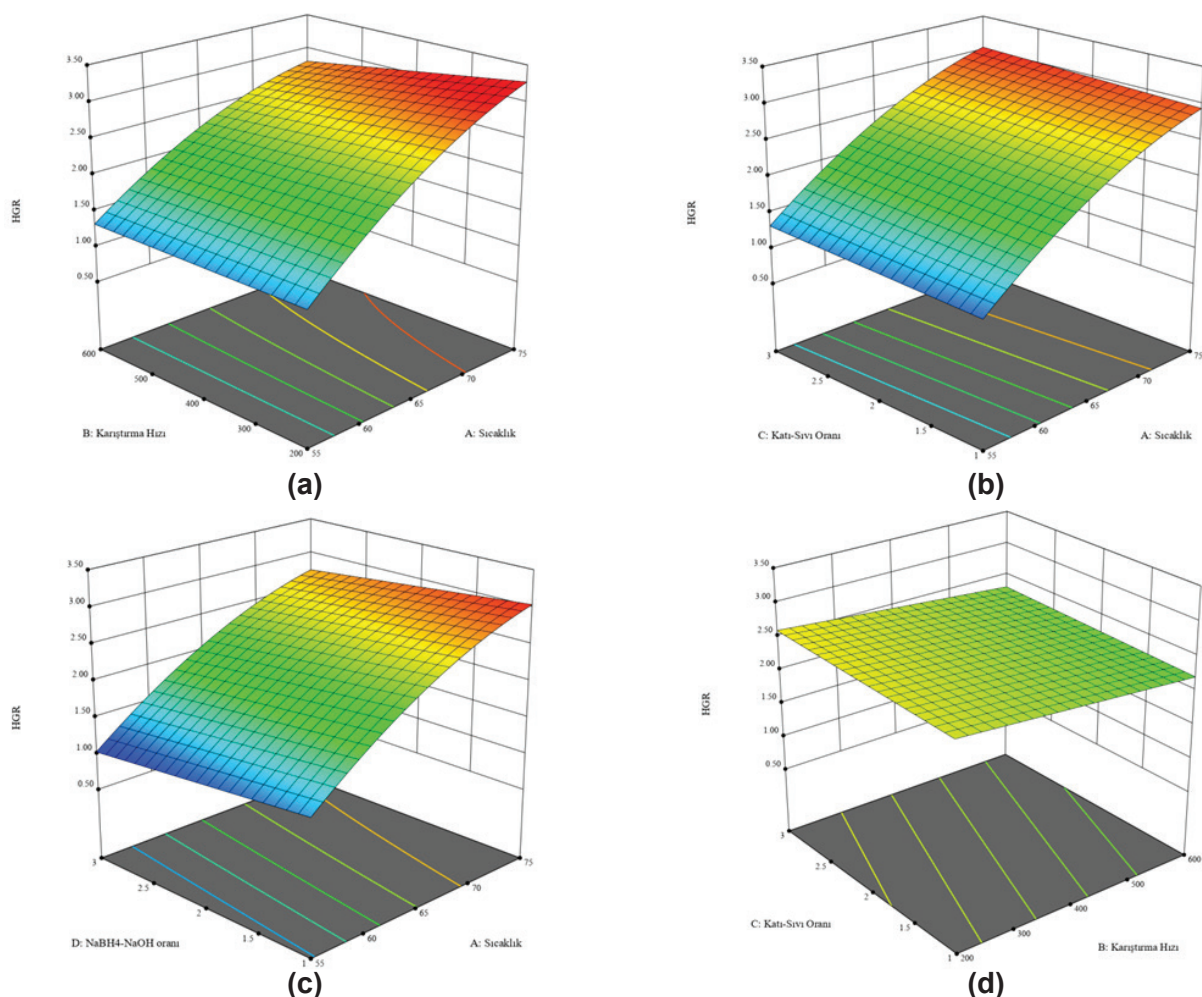
3.1. Girdi Parametrelerinin HGR Üzerindeki Etkisi (Effect of Input Parameters on HGR)

Şekil 3'te her bir parametrenin HGR üzerindeki etkisi gösterilmektedir. Bu grafiklerde, her parametre seviyesi için bir çizginin veya bir eğrinin ortalama tepkisi görülmektedir. Şekil 3'te görüldüğü gibi, HGR, reaksiyon sıcaklığının değişimi ile önemli farklılıklar gösterirken, karıştırma hızı, katı-sıvı oranı ve $\text{NaBH}_4\text{-NaOH}$ oranı gibi parametrelerin değişiminin HGR üzerinde önemli bir etkisinin olmadığı görülmektedir. Beklendiği gibi hidrojen üretim hızı, reaksiyon sıcaklığının 328°K'den 348°K'e artmasıyla ölçüde artış gösterirken buna karşılık katı-sıvı oranı değişiminin hidrojen üretim hızı üzerinde önemli bir etkisinin olmadığı görülmektedir.

Yanıt yüzey yöntemi kullanılarak oluşturulan deney tasarımına göre, reaksiyon sıcaklığı, karıştırma hızı, katı-sıvı oranı ve $\text{NaBH}_4\text{-NaOH}$ oranı değişkenlerin değişimin hidrojen üretim hızı (HGR) ile değişimlerini üç boyutlu olarak gösteren 3-boyutlu model eğrileri Şekil 4'de verilmiştir. Şekil 4a'da katı-sıvı oranı (3) ve karıştırma hızı (400 rpm) sabit tutularak, hidrojen üretim hızının reaksiyon sıcaklığı ve karıştırma hızına bağlı değişimi görülmektedir. Şekilden de açıkça görüldüğü üzere, karıştırma hızı sabit tutularak sıcaklık artırıldığında önemli ölçüde HGR değerinin artışı bununla bir-



Şekil 3. Girdi parametrelerine bağlı olarak HGR değerinin değişimi (Changing HGR value depending on input parameters).



Şekil 4. Girdi parametrelerine göre HGR değeri değişiminin üç boyutlu grafiği (3D surface plots of the HGR as a function of interaction with input parameters).

likte sıcaklık 348°K'de sabit tutulduğunda, karıştırma hızının artmasına bağlı olarak HGR değerinde azalmanın meydana geldiği ve maksimum HGR değerinin 348°K reaksiyon sıcaklığında ve 200 rpm karıştırma hızında elde edilmiştir. Şekil 4b'de katı-sıvı oranı ile sıcaklık değişiminin HGR üzerindeki etkisi görülmektedir ve bu grafiğe göre katı-sıvı oranı sabit bir değerde tutulduğunda sıcaklık değerinin artmasına bağlı olarak HGR değerinin önemli ölçüde arttığı görülmüştür. Bununla birlikte sıcaklık sabit bir değerde tutulduğunda, katı-sıvı oranının artması sonucunda HGR değerinin çok az miktarda artış gösterdiği ve maksimum HGR değerinin 348°K reaksiyon sıcaklığında ve 3 mg_{katalizör}/ml_{yakit} katı-sıvı oranında elde edildiği belirlenmiştir. Şekil 4c'de NaBH₄-NaOH oranı ile sıcaklık değişiminin HGR üzerindeki etkisi gösterilmektedir ve verilen yanıt yüzey eğrisine göre, tüm NaBH₄-NaOH oranı değerlerinde sıcaklık artışının HGR değişimi ile doğrusal olarak değiştiği görülmüştür. Bununla birlikte sıcaklığın sabit tutulduğu durumlarda, NaBH₄-NaOH oranı artışı ile birlikte HGR değerinin azaldığı gözlemlenmiştir. Sıcaklık artışı ile birlikte NaBH₄ hidroliz oranını önemli ölçüde artığı ve eşzamalı olarak HGR değerinin de artmasına neden olduğu belirlenmiştir. Karıştırma hızının

artması ile birlikte, mevcut katalizörün deney düzeneğindeki reaktörün cidarlarına yapışmasından kaynaklı performans kayıpları gerçekleşmiş ve katalizörün etkinliği tam olarak görülememiş olduğundan hidrojen üretim hızında da düşüş meydana gelmiştir. Bununla birlikte, çözelti içerisinde NaOH eklenmesi kendi kendine hidroliz reaksiyonunu önlemektedir ve artan NaOH konsantrasyonu ve dolayısıyla pH değerindeki artış hidroliz hızını azaltmaktadır [11]. Bununla birlikte OH⁻ iyon konsantrasyonu artış göstermekte ve katalizör yüzeylerini kaplayarak katalizör BH₄⁻ etkileşimini engellemektedir. Bilindiği üzere, konsantrasyonun artması reaksiyon ürünü olarak açığa çıkan NaBO₂ çözünürlüğünün azalmasına neden olmaktadır. Çözelti içerisinde çözünemeyen NaBO₂'ların çökelmeleri sonucunda katalizör yüzeyinde birikmeye neden olduğundan hidrojen oluşum hızı ölçüde azalma göstermektedir. Çözelti içerisinde NaBH₄ oranının belirli bir orana kadar artışı hidrojen üretim hızını artırırken, bu oranın daha yüksek değerlerde NaBH₄ konsantrasyonu olumsuz etki göstermektedir. Bu durum artan NaBH₄ konsantrasyonu ile birlikte, düşük çözünürlüğe sahip NaBO₂ oluşumunun ve viskozite değerinin artmasına neden olacaktır. Bunun sonucunda katalizör aktif

Tablo 4. Hidrojen üretim hızı için yanıtların optimizasyon kriterleri (Optimization criteria of responses for hydrogen generation rate).

Parametre	Hedef	Alt limit	Üst Limit	Alt ağırlık	Üst ağırlık	Önem derecesi
Sıcaklık	Aralıkta	328	348	1	1	3
Karıştırma Hızı	Aralıkta	200	600	1	1	3
Katı-Sıvı Oranı	Aralıkta	1	3	1	1	3
NaBH₄-NaOH oranı	Aralıkta	1	3	1	1	3
HGR	Maksimum	0,98	3,13	1	1	5

yüzeyine veya aktif yüzeyden çözelti içeresine kütle transferi daha yavaş gerçekleşecektir [9,39,40]. Bu çalışmada maksimum hidrojen üretim hızı kütlece %5 NaBH₄ ve %5 NaOH değerlerinde elde edilmiştir. Elde edilen bu sonucun literatür verileriyle uyum içerisinde olduğu görülmektedir [9]. Şekil 4d'de görülen yanıt yüzey eğrisine göre, karıştırma hızının katı-sıvı oranı ile değişimi verilmiştir ve Şekilden de görüldüğü üzere tüm katı-sıvı oranı değerlerinde karıştırma hızının artmasıyla hidrojen üretim hızı azalma göstermektedir. Aynı zamanda, karıştırma hızının sabit tutulması durumunda, katı-sıvı oranının artmasına bağlı olarak hidrojen üretim hızının çok fazla bir değişim göstermediği belirgin bir şekilde görülmektedir. Bu şartlar altında maksimum hidrojen üretim hızı için, katı-sıvı oranı 3, karıştırma hızı 200 rpm olarak belirlenmiştir.

Optimizasyon, amaç fonksiyonlarının 0,0 ile 1,0 arasında olduğu arzu edilebilirlik parametresi tarafından kontrol edilir [41]. Tablo 4, her bir çıktıının hedeflerini, alt ve üst limitleri, kullanılan ağırlık değerlerini ve değişkenlerin önem dereceleri olmak üzere optimizasyon kriterlerini vermektedir. Önem derecesi, sırasıyla en az önemi temsil edecek şekilde 1'den 5'e kadar değişmektedir. Ağırlıklar 0,1-10 aralığında değişmekte ve 1'den büyük bir ağırlık hedefe daha fazla vurgu yaparken 1'den küçük bir ağırlık daha az vurgu yapmaktadır. Hidrojen üretim hızının optimum koşullarını belirleyebilmek için girdi parametrelerine göre elde edilen tahmin verileri Tablo 5'te verilmiştir. Tahmin verilerinde

arzu edilebilirlik 1 olarak belirlenmiş ve maksimum hidrojen üretim hızı; reaksiyon sıcaklığı 347,17°K; karıştırma hızı 200,21 rpm; katı-sıvı oranı 2,86 mg_{katalizör} ml_{yanıt}⁻¹; ve NaBH₄-NaOH oranı 1,04 şartlarında bulunmuş ve maksimum hidrojen üretimi 3,22 L.dk⁻¹.g⁻¹ olarak hesaplanmıştır.

3.2. Sonuçların Doğrulanması (Validation of the Results)

Yanıt yüzey metodu sonucunda oluşturulan modellende elde edilen sonuçları doğrulamak amacıyla tahmin edilen koşullar altında deneyler gerçekleştirilmiştir. Optimize edilmiş sonuçların doğrulanması için hidrojen üretim hızının optimal bir koşulu seçilmiştir. Tablo 5'te birinci satırda yer alan deneysel çalışma parametreleri doğrulama deneyi için tercih edilmiştir. Bu şartlar altında iki deney gerçekleştirilmiş olup ve bu deneylerin ortalama değerleri kullanılmıştır. Elde edilen ortalama deney sonucu ve HGR'nın RSM tahminleri Tablo 6'da verilmiştir. Sonuçlar tahmin edilen sonuçların kabul edilebilir hata aralığında deneysel sonuçlarla iyi bir uyum içerisinde olduğunu göstermektedir. RSM modelinden elde edilen sonuçların deneysel sonuçlarla uyum içerisinde olduğunu ve bu çalışma koşullarında elde edilen regresyon modelinin %95 güven düzeyinde güvenilir olabileceğini göstermektedir. Yapılan deneylerde hidrojen üretim hızına ilişkin sonuçlar 3,13 L.dk⁻¹.g⁻¹ olarak bulunmuştur. Bulunan deneysel verinin kabul edilebilir tahmin aralığında (3,07 ile 3,37)

Tablo 5. Yanıt yüzey metoduna göre oluşturulan modelin tahmin sonuçları (Prediction results from response surface methodology).

No	Sıcaklık	Karıştırma Hızı	Katı-Sıvı Oranı	NaBH ₄ -NaOH Oranı	HGR	Arzu Edilebilirlik
1	347,17	200,21	2,86	1,04	3,22	1,000
2	347,40	221,39	2,86	1,09	3,20	1,000
3	347,38	211,93	2,60	1,11	3,19	1,000
4	347,70	239,27	2,72	1,07	3,19	1,000
5	347,49	210,10	1,61	1,00	3,17	1,000
6	347,80	214,46	2,41	1,16	3,19	1,000
7	347,70	204,55	2,50	1,22	3,20	1,000
8	347,86	214,71	2,80	1,20	3,21	1,000
9	347,80	214,46	2,41	1,16	3,19	1,000
10	347,47	235,72	2,62	1,04	3,18	1,000

olduğu belirlenmiştir.

Tablo 6. Tahmin edilen ve deneylerde ölçülen HGR değerlerinin karşılaştırılması (Validation results for comparison of the HGR predicted and experiments).

Cıktı	Tahmin Değeri	Std Sap.	95% PI alt	Deneysel	95% PI üst
HGR	3,22	0,03	3,07	3,13	3,37

4. Sonuçlar (Conclusions)

Bu çalışmada, alkali NaBH_4 çözeltisinin hidrolizi için kimyasal indirgeme yöntemi ile hazırlanan Ni-B katalizörünün kullanıldığı deney düzeneğindeki HGR üzerinde etkisi bilinen parametrelerin optimizasyonu Taguchi L9 ortogonal dizisi kullanılarak gerçekleştirilmiştir. Deney şartlarının optimizasyonu, reaksiyon sıcaklığı, karıştırma hızı, katı-sıvı oranı ve $\text{NaBH}_4\text{-NaOH}$ oranı parametreleri dikkate alınarak yanıt yüzey yöntemi (RSM) kullanılarak araştırılmıştır. RSM modelinden elde veriler ile deneysel verilerin birbiri ile uyum içerisinde olduğu ve bununla birlikte, yapılan doğrulama deneylerinde tutarlı sonuçların elde edildiği görülmüştür. Deneysel çalışmalar sonucunda elde edilen çıktılar aşağıda özetlenmiştir:

- Gerçekleştirilen ANOVA analizi sonucunda reaksiyon sıcaklığı, karıştırma hızı ve $\text{NaBH}_4\text{-NaOH}$ oranı parametrelerinin önemli olduğunu bununla birlikte çalışma deney koşullarında HGR üzerinde reaksiyon sıcaklığının ve $\text{NaBH}_4\text{-NaOH}$ oranının en önemli katkı yapan parametreler olduğunu göstermektedir.
- Deneysel çalışma parametreler aralığında, katı-sıvı oranı değişimlerinin HGR üzerinde önemli bir etkisinin olmadığı görülmüştür.
- Çalışma parametreleri içerisinde, maksimum HGR değeri; reaksiyon sıcaklığı 347,17°C; karıştırma hızı 200,21 rpm; katı-sıvı oranı 2,86 mg_{katalizör}/ml_{yakıt}; ve $\text{NaBH}_4\text{-NaOH}$ oranı 1,04 şartlarında bulunmaktadır. Maksimum hidrojen üretimi 3,22 L.dk⁻¹.g⁻¹ olarak hesaplanmıştır.
- Yapılan doğrulama deneyi sonuçlarında, modelden elde edilen tahmin verileri ile deneysel çalışmalarдан elde edilen verilerin birbiri ile uyum içerisinde olduğu ve ortaya çıkan hata değerinin kabul edilebilir sınırlar içerisinde olduğu görülmüştür.

Yanıt yüzey yöntemi, girdi parametrelerinin ve bu parametrelerin etkileşimlerinin çıktı parametresi üzerindeki etkinliğini tanımlamada istatistiksel olarak başarılı sonuçlar verdiği görülmüştür. Bununla birlikte yanıt yüzey yöntemi ile birlikte kullanılan Taguchi ortogonal deney tasarımı optimum parametrenin belirlenmesinde gerçekleştirilecek olan deney sayısını azaltması ile hem zamansal hem de ekonomik açıdan çok büyük kayıplar yaşanmasının önüne geçmektedir.

Kaynaklar (References)

- [1] Wong, I. C. K., Ng, Y. K., & Lui, V. W. Y. (2014). Cancers of the lung, head and neck on the rise: perspectives on the genotoxicity of air pollution. *Chinese Journal of Cancer*, 33(10), 476-480.
- [2] Gilliland, F. D., Berhane, K., Rappaport, E. B., Thomas, D. C., Avol, E., Gauderman, W. J., ... & Peters, J. M. (2001). The effects of ambient air pollution on school absenteeism due to respiratory illnesses. *Epidemiology*, 43-54.
- [3] Dincer, I. (2020). Covid-19 coronavirus: closing carbon age, but opening hydrogen age. *International Journal of Energy Research*, 44(8), 6093-6097.
- [4] Zoungrana, A., & Çakmakci, M. (2020). From non-renewable energy to renewable by harvesting salinity gradient power by reverse electrodialysis: A review. *International Journal of Energy Research*, 45(3), 3495-3522.
- [5] Mao, J., Zou, J., Lu, C., Zeng, X., & Ding, W. (2017). Hydrogen storage and hydrolysis properties of core-shell structured Mg-MFx (M= V, Ni, La and Ce) nanocomposites prepared by arc plasma method. *Journal of Power Sources*, 366, 131-142.
- [6] Ma, M., Duan, R., Ouyang, L., Zhu, X., Chen, Z., Peng, C., & Zhu, M. (2017). Hydrogen storage and hydrogen generation properties of CaMg2-based alloys. *Journal of Alloys and Compounds*, 691, 929-935.
- [7] Wang, Y., Shen, Y., Qi, K., Cao, Z., Zhang, K., & Wu, S. (2016). Nanostructured cobalt-phosphorous catalysts for hydrogen generation from hydrolysis of sodium borohydride solution. *Renewable Energy*, 89, 285-294.
- [8] Cui, Z., Guo, Y., & Ma, J. (2016). In situ synthesis of graphene supported Co-Sn-B alloy as an efficient catalyst for hydrogen generation from sodium borohydride hydrolysis. *International Journal of Hydrogen Energy*, 41(3), 1592-1599.
- [9] Aydin, M., Hasimoglu, A., Bayrak, Y., & Ozdemir, O. K. (2015). Kinetic properties of co-reduced Co-B/graphene catalyst powder for hydrogen generation of sodium borohydride. *Journal of Renewable and Sustainable Energy*, 7(1), 013117.
- [10] Rakap, M. (2015). PVP-stabilized Ru-Rh nanoparticles as highly efficient catalysts for hydrogen generation from hydrolysis of ammonia borane. *Journal of Alloys and Compounds*, 649, 1025-1030.
- [11] Xu, D., Wang, H., Guo, Q., & Ji, S. (2011). Catalytic behavior of carbon supported Ni-B, Co-B and Co-Ni-B in hydrogen generation by hydrolysis of KBH4. *Fuel Processing Technology*, 92(8), 1606-1610.
- [12] Tong, D. G., Han, X., Chu, W., Chen, H., & Ji, X. Y. (2007). Preparation of mesoporous Co-B catalyst via self-assembled triblock copolymer templates. *Materials Letters*, 61(25), 4679-4682.
- [13] Netskina, O. V., Kochubey, D. I., Prosvirin, I. P., Malykhin, S. E., Komova, O. V., Kanazhevskiy, V. V., ... & Simagina, V. I. (2017). Cobalt-boron catalyst for NaBH_4 hydrolysis: The state of the active component forming from cobalt chloride in a reaction medium. *Molecular Catalysis*, 441, 100-108.

- [14] Wang, X., Liao, J., Li, H., Wang, H., Wang, R., Pollet, B. G., & Ji, S. (2018). Highly active porous Co-B nano-alloy synthesized on liquid-gas interface for hydrolysis of sodium borohydride. *International Journal of Hydrogen Energy*, 43(37), 17543-17555.
- [15] Kojima, Y., Kawai, Y., Nakanishi, H., & Matsumoto, S. (2004). Compressed hydrogen generation using chemical hydride. *Journal of Power Sources*, 135(1-2), 36-41.
- [16] Demirci, U. B., & Garin, F. (2008). Promoted sulphated-zirconia catalysed hydrolysis of sodium tetrahydroborate. *Catalysis Communications*, 9(6), 1167-1172.
- [17] Özdemir, E. (2015). Enhanced catalytic activity of Co-B/glassy carbon and Co-B/graphite catalysts for hydrolysis of sodium borohydride. *International Journal of Hydrogen Energy*, 40(40), 14045-14051.
- [18] Schlesinger, H. I., Brown, H. C., Finholt, A. E., Gilbreath, J. R., Hoekstra, H. R., & Hyde, E. K. (1953). Sodium borohydride, its hydrolysis and its use as a reducing agent and in the generation of hydrogen1. *Journal of the American Chemical Society*, 75(1), 215-219.
- [19] Uzundurukan, A., & Devrim, Y. (2019). Hydrogen generation from sodium borohydride hydrolysis by multi-walled carbon nanotube supported platinum catalyst: A kinetic study. *International Journal of Hydrogen Energy*, 44(33), 17586-17594.
- [20] Özkar, S., & Zahmakıran, M. (2005). Hydrogen generation from hydrolysis of sodium borohydride using Ru(0) nanoclusters as catalyst. *Journal of Alloys and Compounds*, 404, 728-731.
- [21] Huff, C., Long, J. M., Heyman, A., & Abdel-Fattah, T. M. (2018). Palladium nanoparticle multiwalled carbon nanotube composite as catalyst for hydrogen production by the hydrolysis of sodium borohydride. *ACS Applied Energy Materials*, 1(9), 4635-4640.
- [22] Zabielaite, A., Balciūnaitė, A., Stalnionienė, I., Lichušina, S., Šimkūnaitė, D., Vaičiūnienė, J., ... & Norukus, E. (2018). Fiber-shaped Co modified with Au and Pt crystallites for enhanced hydrogen generation from sodium borohydride. *International Journal of Hydrogen Energy*, 43(52), 23310-23318.
- [23] Gao, Z., Ding, C., Wang, J., Ding, G., Xue, Y., Zhang, Y., ... & Gao, X. (2019). Cobalt nanoparticles packaged into nitrogen-doped porous carbon derived from metal-organic framework nanocrystals for hydrogen production by hydrolysis of sodium borohydride. *International Journal of Hydrogen Energy*, 44(16), 8365-8375.
- [24] Nie, M., Zou, Y. C., Huang, Y. M., & Wang, J. Q. (2012). Ni-Fe-B catalysts for NaBH₄ hydrolysis. *International Journal of Hydrogen Energy*, 37(2), 1568-1576.
- [25] Duman, S., & Özkar, S. (2018). Ceria supported manganese(0) nanoparticle catalysts for hydrogen generation from the hydrolysis of sodium borohydride. *International Journal of Hydrogen Energy*, 43(32), 15262-15274.
- [26] Balbay, A., & Saka, C. (2018). Effect of phosphoric acid addition on the hydrogen production from hydrolysis of NaBH₄ with Cu based catalyst. *Energy Sources, Part A: Recovery, Utilization, and Environmental Effects*, 40(7), 794-804.
- [27] Al-Fatesh, A. S., Naeem, M. A., Fakieha, A. H., & Abasaeed, A. E. (2014). Role of La₂O₃ as promoter and support in Ni/y-Al₂O₃ catalysts for dry reforming of methane. *Chinese Journal of Chemical Engineering*, 22(1), 28-37.
- [28] Hua, D., Hanxi, Y., Xiping, A., & Chuansin, C. (2003). Hydrogen production from catalytic hydrolysis of sodium borohydride solution using nickel boride catalyst. *International Journal of Hydrogen Energy*, 28(10), 1095-1100.
- [29] Lee, J., Shin, H., Choi, K. S., Lee, J., Choi, J. Y., & Yu, H. K. (2019). Carbon layer supported nickel catalyst for sodium borohydride (NaBH₄) dehydrogenation. *International Journal of Hydrogen Energy*, 44(5), 2943-2950.
- [30] Ghodke, N. P., Rayaprol, S., Bhoraskar, S. V., & Mathe, V. L. (2020). Catalytic hydrolysis of sodium borohydride solution for hydrogen production using thermal plasma synthesized nickel nanoparticles. *International Journal of Hydrogen Energy*, 45(33), 16591-16605.
- [31] Saka, C., Şahin, Ö., Demir, H., Karabulut, A., & Sarıkaya, A. (2015). Hydrogen generation from sodium borohydride hydrolysis with a Cu-Co-based catalyst: a kinetic study. *Energy Sources, Part A: Recovery, Utilization, and Environmental Effects*, 37(9), 956-964.
- [32] Ekinci, A., Cengiz, E., Kuncan, M., & Şahin, Ö. (2020). Hydrolysis of sodium borohydride solutions both in the presence of Ni-B catalyst and in the case of microwave application. *International Journal of Hydrogen Energy*, 45(60), 34749-34760.
- [33] Kazici, H. Ç., Yılmaz, Ş., Şahan, T., Yıldız, F., Er, Ö. F., & Kivrak, H. (2020). A comprehensive study of hydrogen production from ammonia borane via PdCoAg/AC nanoparticles and anodic current in alkaline medium: experimental design with response surface methodology. *Frontiers in Energy*, 14(3), 578-589.
- [34] Özkan, G., Akkuş, M. S., & Özkan, G. (2019). The effects of operating conditions on hydrogen production from sodium borohydride using Box-Wilson optimization technique. *International Journal of Hydrogen Energy*, 44(20), 9811-9816.
- [35] Wu, H. W., & Ku, H. W. (2012). Effects of modified flow field on optimal parameters estimation and cell performance of a PEM fuel cell with the Taguchi method. *International Journal of Hydrogen Energy*, 37(2), 1613-1627.
- [36] Wu, H. W., & Gu, H. W. (2010). Analysis of operating parameters considering flow orientation for the performance of a proton exchange membrane fuel cell using the Taguchi method. *Journal of Power Sources*, 195(11), 3621-3630.
- [37] Berkani, M., Kadmi, Y., Bouchareb, M. K., Bouhechlassa, M., & Bouzaza, A. (2020). Combination of a Box-Behnken design technique with response surface methodology for optimization of the photocatalytic mineralization of CI Basic Red 46 dye from aqueous solution. *Arabian Journal of Chemistry*, 13(11), 8338-8346.
- [38] Wang, H., Gan, H., Wang, G., & Zhong, G. (2020). Emission and performance optimization of marine four-stroke dual-fuel engine based on response surface

methodology. *Mathematical Problems in Engineering*, 2020, 1-9.

- [39] Patel, N., Fernandes, R., & Miotello, A. (2009). Hydrogen generation by hydrolysis of NaBH₄ with efficient Co-P-B catalyst: a kinetic study. *Journal of Power Sources*, 188(2), 411-420.
- [40] Fernandes, R., Patel, N., & Miotello, A. (2009). Hydrogen generation by hydrolysis of alkaline NaBH₄ solution with Cr-promoted Co-B amorphous catalyst. *Applied Catalysis B: Environmental*, 92(1-2), 68-74.
- [41] Hatami, M., Cuijpers, M. C., & Boot, M. D. (2015). Experimental optimization of the vanes geometry for a variable geometry turbocharger (VGT) using a Design of Experiment (DoE) approach. *Energy Conversion and Management*, 106, 1057-1070.



Zinc borate chemical garden and zinc borate powders from tincal mineral and zinc sulfate heptahydrate

Burcu Alp¹, Mehmet Gönen², Sevdiye Atakul Savrik³, Devrim Balkose^{4*}

¹Süleyman Demirel University, Department of Chemical Engineering, Isparta, 32260, Turkey,
ORCID orcid.org/0000-0002-0380-2020

²Süleyman Demirel University, Department of Chemical Engineering, Isparta, 32260, Turkey,
ORCID orcid.org/0000-0001-5780-4622

³Akzo Nobel, Izmir, 35410 Turkey, ORCID orcid.org/0000-0002-1402-0569

⁴Izmir Institute of Technology, Department of Chemical Engineering, Izmir, 35430, Turkey,
ORCID orcid.org/0000-0002-1117-9486

ARTICLE INFO

Article history:

Received October 12, 2020

Accepted January 2, 2021

Available online March 31, 2021

Research Article

DOI: 10.30728/boron.809041

Keywords:

Chemical garden
Osmotic pressure
Tincal
Zinc borate
Zinc sulfate

ABSTRACT

The formation of the first membrane, the swelling of the crystal by incoming water from the semipermeable membrane and the formation of irregular shaped branches were observed by optical microscopy, when zinc sulfate heptahydrate crystals were immersed in saturated borax solution. The powders obtained by mixing dilute aqueous borax and zinc sulfate solutions had B, O, Na, S and Zn elements. Presence of Na Zn_{1/2}B₄O₇·xH₂O was indicated by EDX analysis. The molar ratio of B₂O₃/ZnO in powders was around 2. FTIR analysis indicated the ratio of absorbance values of asymmetric stretching vibrations of B₍₃₎-O at 1351 cm⁻¹ to that of B₍₄₎-O at 1026 cm⁻¹ increased with their heating time at 90°C during their preparation. X-ray diffraction patterns indicated the presence of Zn(OH)₂ and Zn₄(OH)₆(SO₄)₄·4H₂O. The zinc borate compounds in the powders were not crystalline since no sharp peaks related to zinc borates were present in x-ray diffraction diagram. There were two mass loss steps in TG curves of the powders. The first step at 150-350°C and the second step at 700-950°C were due to elimination of water and due to decomposition of sulfate ions respectively. The submicron powders were a mixture of zinc borate, Zn(OH)₂, Zn₄(OH)₆(SO₄)₄·4H₂O and Na Zn_{1/2}B₄O₇·xH₂O and they could be used as lubricant additive due to their small particle size of 600 nm.

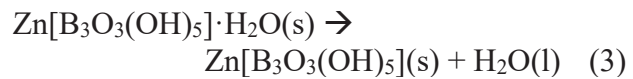
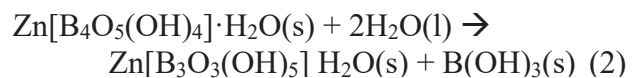
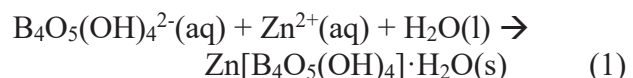
1. Introduction

Chemical gardens are the hollow fibers formed by immersion of a soluble metal-salt particle in an aqueous solution containing either of the silicate, phosphate, carbonate, oxalate, sulfide or hydroxide ions. The possible reactants in chemical gardens and their mechanism of formation are summarized by Barge et al. [1]. The gelatinous precipitate formed around the salt particle acts as a membrane and allows the passage of small water molecules and does not allow the passage of large metal ions [1]. Membrane bursts when the osmotic pressure inside becomes higher than its tensile strength. The metal-ion solution from crystal side ejects into outer solution and tubular precipitates form around the flow creating hollow chemical garden tubes [2]. Crystals of cations of group II [2] and the transition metals [3-7] were used as salts added to silicate solution. The kinetics of formation of silica garden tubes prepared using different metal salts were investigated by Glaab et al. [8]. Other solutions other than silicates

were also used in chemical gardens. Hexacyanoferate Fe(CN)₆⁻¹ [9,10], OH⁻ [11] anions are examples for this case. Real time X-ray fluorescence (XRF) movie technique was used to monitor chemical garden fiber formation [12].

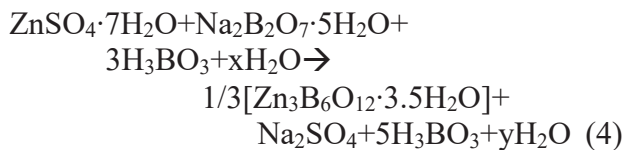
Zinc borates are commercially important chemicals [13]. They can be obtained either by reaction of ZnO and H₃BO₃ [14] or reaction of borax with zinc salts [15-23].

The reactions of borate anion with zinc cation are shown below:



*Corresponding author: devrimbalkose@iyte.edu.tr

Kıpçak et al. [19] synthesized zinc borate using tincalconite mineral according to the following reaction in Equation 4.



$\text{Zn}(\text{H}_2\text{O})\text{B}_2\text{O}_7 \cdot 0.12\text{H}_2\text{O}$ was obtained from $\text{ZnSO}_4 \cdot 7\text{H}_2\text{O}$, $\text{K}_2\text{B}_4\text{O}_7 \cdot 4\text{H}_2\text{O}$, and $\text{NH}_4\text{HB}_4\text{O}_7 \cdot 3\text{H}_2\text{O}$ in H_2O with pH regulated to 9.5 with 3 mol dm^{-3} NaOH solution by Liang et al. [22].

$4\text{ZnO} \cdot \text{B}_2\text{O}_3 \cdot \text{H}_2\text{O}$ having 2D and 3D nano/microstructures were obtained by hydrothermal method in the presence of surfactant polyethylene glycol-300 from $\text{Na}_2\text{B}_4\text{O}_7 \cdot 10\text{H}_2\text{O}$ and ZnSO_4 [21,24]. Nano discs of $2\text{ZnO} \cdot 3\text{B}_2\text{O}_3 \cdot 3\text{H}_2\text{O}$ were obtained from aqueous borax and zinc salt solutions by the addition of oleic acid [25]. Lubricant additive zinc borate nanoparticles were obtained from borax decahydrate and zinc nitrate hexahydrate solutions by addition of sodium dodecylbenzenesulfonate [15], PEG 4000 and Span 60 [26], phosphate ester [27] as templates.

Parallel to zinc borate formation the possibility of $\text{Zn}(\text{OH})_2$ formation according to Equation 5 was indicated by Savrik et al. [26].



Polat and Sayan [28] investigated the change of properties of zinc borate with stirring rate, temperature and reactant feed rate. For zinc borate crystallization, sodium tetraborate decahydrate and zinc sulfate heptahydrate were used as reactants. The results showed that the obtained crystals were in the form of $\text{Zn}_2\text{B}_6\text{O}_{11} \cdot 7\text{H}_2\text{O}$ and the operating conditions change the size, morphology, and filtration characteristics of the zinc borate crystals. Box-Behnken design with response surface methodology showed that the data sufficiently fit the second-order polynomial model for the variables of stirring rate, temperature, and reactant feed rate. The minimum particle size ($3.3 \mu\text{m}$) was obtained at 450 rpm stirring rate, 85°C temperature and $300 \text{ cm}^3 \text{ h}^{-1}$ reactant feed rate.

In this study, it was aimed to obtain and monitor the formation of chemical garden fibers by immersing zinc sulfate heptahydrate crystals in borax decahydrate solution prepared from purified Kırka tincal mineral. It was also aimed to characterize purified tincal mineral and to identify products in the powders formed by the reaction of dilute borax solution with dilute zinc sulfate heptahydrate solution. Elemental analysis (EDX), Fourier transform infrared spectroscopy (FTIR), X-ray dif-

fraction (XRD), thermal gravimetric (TG) analysis and scanning electron microscopy (SEM) techniques were used for this purpose.

2. Materials and Methods

2.1. Materials

Tincal mineral from Etibank Kırka Mines, anionic flocculant SP100A (American Cyanimid Company) and zinc sulfate heptahydrate (99%) from Merck were used in the experiments.

2.2. Purification of Tincal Mineral

Tincal mineral was purified from impurities by flocculation. 80 cm^3 20% tincal mineral solution was mixed with 3 cm^3 of 0.1% SP100A anionic flocculant at 80°C . 70 cm^3 of the clear solution on top of the settled particles were transferred to another beaker and the crystals obtained by cooling were separated by filtration. They were dried at 20°C and used in zinc borate synthesis. The flocculated particles were characterized as dolomite by Akdeniz et al. [29].

2.3. Chemical Garden Preparation and Characterization

Zinc sulfate heptahydrate crystals were immersed in saturated borax decahydrate solution at 20°C for the formation of zinc borate chemical garden. Since it was not possible to record the photographs of the very small diameter transparent fibers by conventional photography, the same process was repeated using an optical microscope. A small crystal of zinc sulfate heptahydrate was placed on a drop of saturated borax solution at 20°C having 4.71% borax on a microscope slide and its photographs were captured in transmission mode by a digital camera fitted to Olympus, CH40 optical microscope at different time intervals.

2.4. Preparation of Zinc Borate

50 cm^3 of $0.1 \text{ mol} \cdot \text{dm}^{-3}$ borax decahydrate solution was mixed with 50 cm^3 0.1 mol dm^{-3} with zinc sulfate heptahydrate at 90°C in a thermostatic shaking water bath up to 120 minutes. Samples withdrawn at different periods were filtered and the obtained precipitates were washed with water and dried at 105°C till constant mass was obtained.

2.5. Characterization Methods

FTIR of the samples were obtained with KBr disc method in $400\text{-}4000 \text{ cm}^{-1}$ wavenumber range by using Shimadzu 8601 PC FTIR spectrophotometer. Setaram LABSYS TGA/DTA was used for thermal gravimetric analysis of the samples. The samples were heated from room temperature to 1000°C at $10^\circ\text{C min}^{-1}$ rate under $40 \text{ cm}^3 \text{ min}^{-1}$ N_2 gas flow rate for this purpose. The powder X-ray diffraction (XRD) diagrams of the

samples were obtained by using Philips Xpert-Pro X-ray diffractometer. CuK_α radiation with 0.154 nm wavelength at 45 kV and 40 mA was used and the data was recorded in 2θ range of 2-70°. Philips XL30 SFEG scanning electron microscope was used at accelerating voltage of 5 or 6 kV to obtain the SEM micrographs of the samples coated with gold. EDX analyses of the pristine samples were made using the same instrument.

3. Results and Discussion

3.1. Characterization of Purified Borax

3.1.1. X-ray diffraction diagram of borax

X-ray diffraction diagram of borax sample used in the present study seen in Figure 1 had identical peaks with borax decahydrate (with JCPDS card number 01-75-1078) [30]. The 2θ values of the peaks were the same but their relative intensities were different than reported in the reference [30] due to orientation of the crystals. The most intense peak is at 2θ value of 34° indicated that crystals were oriented perpendicular to (024) plane [30].

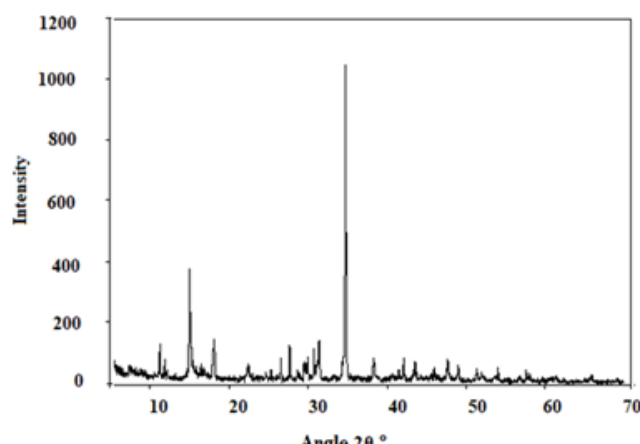


Figure 1. X-ray diffraction diagram of borax decahydrate.

3.1.2. FTIR spectrum of borax

The FTIR spectrum of borax from purified tincal mineral shown in Figure 2 confirms with the FTIR spectrum of borax decahydrate reported in literature [31,32].

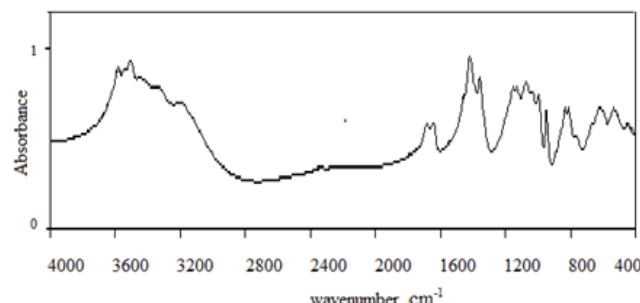


Figure 2. FTIR spectrum of borax decahydrate.

3.1.3. Morphology of borax

The SEM micrograph of borax decahydrate crystals seen in Figure 3 indicated they are in needle shape with length 5-10 μm and diameter 0.2-1 μm. The X-ray diffraction diagram also indicated one dimensional orientation of borax decahydrate crystals. This could be due to templating effect of the flocculant (Superfloc100A) used for the removal of impurities in borax mineral by flocculation.

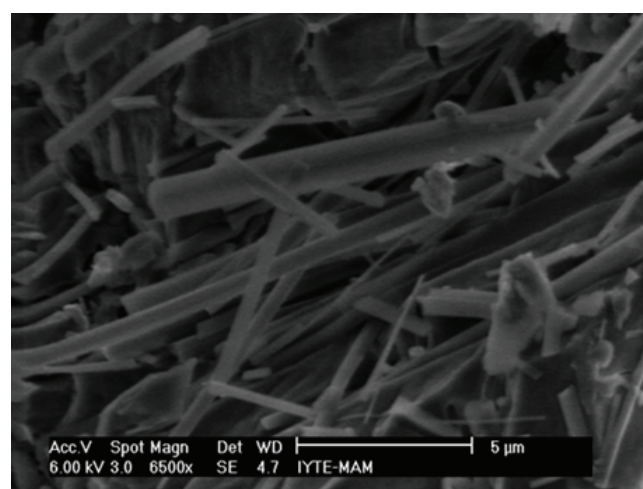


Figure 3. SEM micrograph of borax decahydrate.

3.2. Chemical Garden

Zinc sulfate heptahydrate particles were immersed in saturated borax solution at room temperature. Nearly transparent short chemical garden fibers formed in 30 minutes. Good photographs of the fibers could not be taken since they were transparent. Long fibers similar to the ones formed by immersion of zinc salts [5] and copper salts [11] to aqueous sodium silicate solution were not observed in the present case of aqueous borax zinc salt system. For this reason, it was attempted to monitor the fiber formation using an optical microscope. A small crystal of zinc sulfate heptahydrate was placed on top of a drop of saturated borax solution and the photographs were taken at different times. When zinc sulfate heptahydrate is placed in aqueous solution of borax solution it starts to dissolve to give Zn²⁺ and SO₄²⁻ ions which react with the OH⁻ and B₄O₇²⁻ ions in solution. A semipermeable membrane made out of possible solid reaction products such as Zn(OH)₂, Zn₄(OH)₆(SO₄)₂·4H₂O and 2ZnO·3B₂O₃·3H₂O covering the surface of sodium sulfate crystal is formed. Water can easily diffuse through the membrane creating a very high osmotic pressure in the crystal side. A saturated sodium sulfate solution forms on the surface of the crystals beneath the semipermeable membrane formed. Considering the solubility of sodium sulfate heptahydrate in water at 20°C (3.143 mol kg⁻¹) [33] the osmotic pressure created inside of the membrane is calculated as 22.95 MPa using Equation 6.

$$\pi = icRT \quad (6)$$

where π is osmotic pressure, i is number of ions formed by the dissociation of one mol substance, c is concentration in mol m⁻³, R is the gas constant in J mol⁻¹ K⁻¹ and T is temperature in K. This high osmotic pressure first swells, then ruptures the membrane and saturated salt solution flows through the holes created on its surface into borax solution resulting formation of a new membrane with the reaction of borax and zinc sulfate. The membrane ruptures and reforms repeatedly. In crystal side of the membrane there is a concentrated zinc sulfate solution and at the other side of the membrane aqueous borax solution is present. The inside solution is ejected into outside solution at points ruptured on the membrane and thus a new membrane emanating from the center membrane is formed. Thus hollow fibers with Zn(OH)₂, Zn₄(OH)₆(SO₄)₂·4H₂O and 2ZnO·3B₂O₃·3H₂O would form. The micrographs of the process taken from optical microscope at different time periods are shown in Figure 4. The crystal immersed in solution is covered immediately with a membrane. At zero time the size of the membrane coated crystal is 100 µm as observed in Figure 4a and 4b. The size expanded by swelling due to the inflow water through the membrane to 277 µm in 302 seconds as seen in Figure 4c. The surface of the membrane is not smooth. The growth is not the same in all directions. Two branches in 108 µm size emanated from a body of

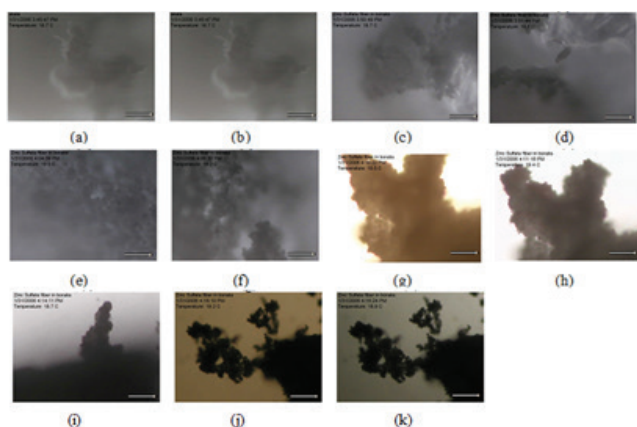


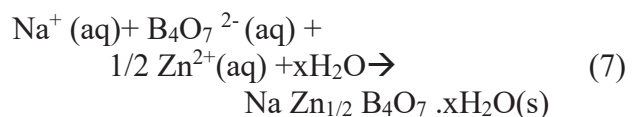
Figure 4. Optical micrographs of zinc sulfate hepta hydrate immersed in saturated borax solution at room temperature after immersion time of a and b. 0.0 , c. 302, d. 357, e. 1129, f. 1245, g.1475, h.1529, i. 1704, j.1823, k. 1837 seconds (scale bar represents 100 µm)

153 µm in 1475 s in Figure 4g. A branch with 107 µm at the bottom, 61 µm in the middle and 15 µm at the tip is seen in 1704 s in Figure 4i and particles having 31-138 µm with very tiny branches with 15 µm diameter forms in 1837 s in Figure 4k. The optical microscope had shown the formation and expansion of branches of with irregular shapes. Filtering of the fibers formed by immersing zinc sulfate heptahydrate in borax solution, washing and drying would give hallow fibers having zinc borates, Zn(OH)₂, Zn₄(OH)₆(SO₄)₂·4H₂O.

3.3. Characterization of Powders Obtained by Mixing Aqueous Tincal Mineral and Aqueous Zinc Heptahydrate Solutions

3.3.1. Elemental analysis of the powders

EDX analysis gives information about the elemental composition of the surface of the powders. The elemental composition of the samples excluding hydrogen is shown in Table 1. In the same table molar ratios of B₂O₃/ZnO, Na/S and Na/Zn are shown. Free water molecules in the surface of the powders would be separated since the system operates under vacuum. Thus the oxygen content of the surface would be lower due to water evaporation. The samples obtained by heating for different periods at 90°C during their preparation contained B, O, Na, S and Zn elements as shown in Table 1. The molar ratio of B₂O₃/ZnO was close to 2. The presence of S and Na elements in the samples could be due to incomplete removal of the by product sodium sulfate or due to formation of double salts. However, there was higher amount of sodium element than that is equivalent to S element to form sodium sulfate. This indicated that sodium element was present in double salts formed during the reactions. Equation 7 represents formation of a double salt by the reactants in the mixture.



3.3.2. FTIR analysis of the powders

The FTIR spectra of the powders are shown in Figure 5. The presence of the absorption maxima at 3400 cm⁻¹ for hydrogen bonded OH and at 1640 cm⁻¹ for H₂O

Table 1. The elemental composition of the samples heated for different time periods at 90°C during their preparation.

Time, minutes	B, mass (%)	O, mass (%)	Na, mass (%)	S, mass (%)	Zn, mass (%)	B ₂ O ₃ /ZnO Mol ratio	Na/S Mol ratio	Na/Zn
0	14.49	37.91	20.35	3.32	23.93	1.83	8.52	2.41
30	17.70	34.88	15.27	0.94	31.22	1.71	22.60	1.39
60	19.30	41.55	16.47	1.07	21.61	2.70	21.41	2.16
90	15.58	39.91	19.53	0.90	24.09	1.95	30.19	2.30
120	15.58	40.00	19.53	1.16	25.79	1.98	23.42	2.34

bending vibrations indicated presence of OH groups and H₂O in the samples. In the spectra of all samples the vibrations of O-B-O in planar ($B_{(3)}\text{-O}$) and vibrations of O-B-O in tetrahedral ($B_{(4)}\text{-O}$) geometries and vibrations of B-O-H are seen [19]. The ratio of absorbance of $B_{(3)}\text{-O}$ vibrations at 1351 cm⁻¹ to absorbance of $B_{(4)}\text{-O}$ vibrations at 1026 cm⁻¹ increased with heating period at 90°C during preparation of the powder samples as shown in Table 2. This indicated the formation of planar borate ions with the expense of tetrahedral borate ions with time. Bending vibrations of B-O-H that should be observed in 1221 and 1108 cm⁻¹ range overlapped with tetrahedral O-B-O vibrations. The bending vibration of planar O-B-O in ($B_{(3)}\text{-O}$) is observed at 660 cm⁻¹ [19].

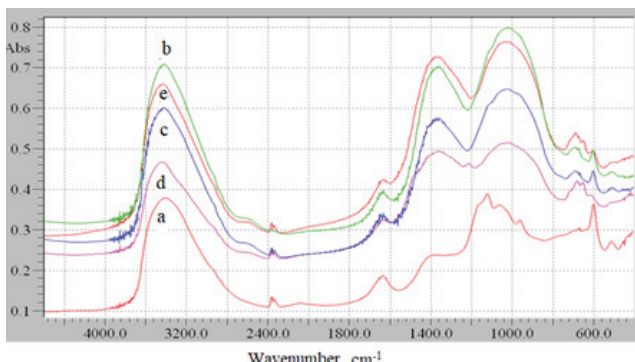


Figure 5. FTIR spectrum of the samples heated at 90°C during preparation for heating times of a) 0, b) 30, c) 60, d) 90, e) 120 minutes.

Table 2. The ratio of absorbance of $B_{(3)}\text{-O}$ asymmetric stretching vibrations at 1351 cm⁻¹ to $B_{(4)}\text{-O}$ asymmetric stretching vibrations at 1026 cm⁻¹ for samples heated for different time periods at 90°C during their preparation.

Time (minutes)	Intensity of 1351 cm ⁻¹ / Intensity of 1026 cm ⁻¹
0	0.67
30	0.88
60	0.88
90	0.98
120	0.99

The presence of the bands for Zn(OH)₂ at 1086 cm⁻¹ and 1029 cm⁻¹ due to asymmetric stretching vibrations of Zn-O-Zn and at 717 cm⁻¹ due to bending vibrations of OH groups in Zn(OH)₂ indicated that the Zn(OH)₂ was also present in the powders [34]. The small sharp band observed at 600 cm⁻¹ in Figure 5 could be attributed to the bending vibrations of sulfate ion that must be observed at 617 cm⁻¹ [35]. The antisymmetric stretching vibrations of sulfate groups that should be observed at 1106 cm⁻¹ [35] overlaps with the broad band observed for antisymmetric stretching vibrations of O-B-O in $B_{(4)}\text{-O}$.

FTIR spectroscopy indicated presence of planar and tetrahedral borate groups, Zn(OH)₂ and sulfate groups. The FTIR spectrum of the powder formed at the first instant of mixing two reactant solutions indicated higher sulfate content than the powders obtained by further heating.

3.3.3. X-ray diffraction

X-ray diffraction diagram of the samples obtained for different heating periods are depicted in Figure 6. Sharp peaks at 2θ values of 9.4°, 18.8°, 21.6°, 25.9°, 27.4°, 29.5°, 32.9°, 34.8°, and 59.8° were observed in the X-ray diffraction diagram (curve e in Figure 6) of the sample heated for 120 minutes in its preparation. The peaks for sodium sulfate by product were also investigated since the EDX analysis indicated the presence of sulfur element. The peaks expected at 22.5°, 23.6°, 25.5°, 37.9°, 46.3°, 48.9° for sodium sulfate (JCPDS card number 36-0397) [36] were not present in Figure 6. Thus sodium sulfate was present as only in small amount as impurity. The presence of peaks at 2θ values of 31.7°, 34.3°, 36.2° (JCPDS card number 79-0206) would indicate the presence of ZnO in the samples [37]. ZnO also was not present since these peaks were absent. Zn(OH)₂ crystals have peaks at 2θ values of 15.4°, 15.8°, 26.0°, 27.0°, 27.8°, 29.6°, 30.9°, 31.8°, 34.2°, 36.0°, 36.3°, 37.0°, 38.4°, 39.1°, 42°, 47.1°, 48.5° and 49.3° in its XRD pattern. [34]. β-Zn(OH)₂ was present in the samples since most of these peaks were present in the x-ray diffraction diagram in Figure 6.

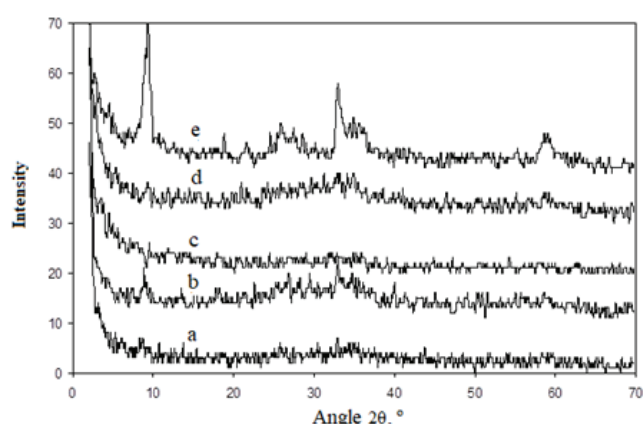
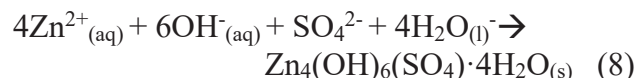


Figure 6. X-ray diffraction diagrams of the samples heated at 90°C during preparation for heating times of a) 0, b) 30, c) 60, d) 90, e) 120 minutes.

Formation of Zn₄(OH)₆(SO₄)·4H₂O [38] is another possibility in the system according to Equation 8.



The observed X-ray diffraction peaks of the samples partially coincides with X-ray diffraction peaks of

$\text{Zn}_4(\text{OH})_6(\text{SO}_4)_4 \cdot 4\text{H}_2\text{O}$ with ASTM Powder file 9-204 [39]. Also $2\text{ZnO} \cdot 3\text{B}_2\text{O}_3 \cdot 3\text{H}_2\text{O}$ and $2\text{ZnO} \cdot 3\text{B}_2\text{O}_3 \cdot 7\text{H}_2\text{O}$ peaks [40] were not present. X-ray diffraction diagrams of the samples indicated the presence of $\text{Zn}(\text{OH})_2$ and $\text{Zn}_4(\text{OH})_6(\text{SO}_4)_4 \cdot 4\text{H}_2\text{O}$ crystals in the samples. Even if $2\text{ZnO} \cdot 3\text{B}_2\text{O}_3 \cdot 3\text{H}_2\text{O}$ and $2\text{ZnO} \cdot 3\text{B}_2\text{O}_3 \cdot 7\text{H}_2\text{O}$ were present in the samples they were not in crystalline form or they had very small crystals that caused line broadening and overlapping.

3.3.4. Thermal analysis of the samples

The TG curves of the samples in Figure 7 showed two steps of mass decrease as tabulated in Table 3. The first step in 150-350°C range is most probably due to elimination of H_2O from $\text{Zn}(\text{OH})_2$ and $\text{Zn}_4(\text{OH})_6(\text{SO}_4)_4 \cdot 4\text{H}_2\text{O}$ and possible zinc borate hydrates. The second step in 700-950°C range could be due to decomposition of sulfate ions as shown below [38].

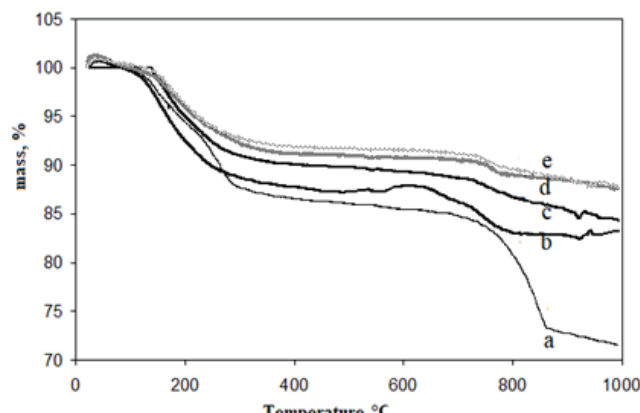
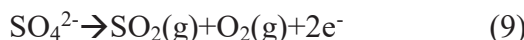


Figure 7. TG curves of crystals obtained after heating at 90°C during preparation for heating times of a) 0, b) 30, c) 60, d) 90, e) 120 minutes.

TG analysis showed that the compounds with high water and sulfate content forms at the first instant of the reaction and the water content and sulfate content decrease as the heating period at 90°C increases. The change in the water content of the compounds is small-

er than the decrease in sulfate content with heating period. While the water content decreases from 12% to 9%, the sulfate content decreases from 10 to 1%.

3.3.5. Morphology of the samples

The SEM micrograph of the sample heated for 30 minutes at 90°C in Figure 8 showed that it consists of agglomerated primary particles of 600 nm average diameter. The primary particles should have adhered to each other during drying process.

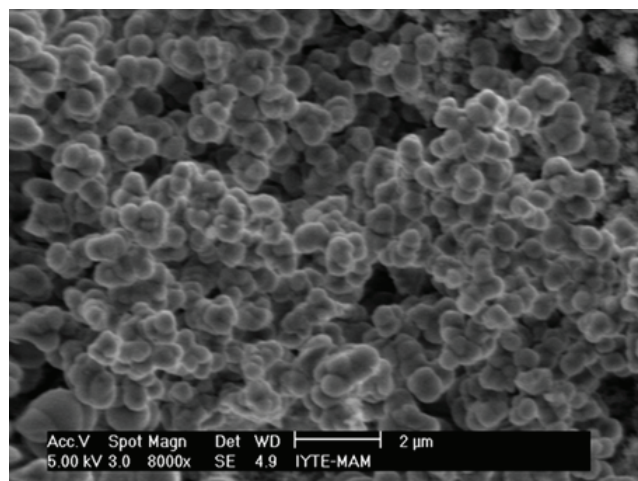


Figure 8. SEM micrograph of the sample heated for 30 minutes at 90°C during its preparation.

3.4. Discussion

Producing zinc borates either in hollow fiber form or powder form from tincal mineral and zinc sulfate heptahydrate was investigated in this work. Since in the aqueous reaction medium OH^- , Na^+ , SO_4^{2-} were also present besides $\text{B}_4\text{O}_7^{2-}$ and Zn^{2+} ions the formed powders were not pure zinc borates but they also contained $\text{Zn}(\text{OH})_2$, $\text{Zn}_4(\text{OH})_6(\text{SO}_4)_4 \cdot 4\text{H}_2\text{O}$ and $\text{Na Zn}_{1/2} \text{B}_4\text{O}_7 \cdot x\text{H}_2\text{O}$. The x-ray diffraction diagrams showed the presence of crystalline $\text{Zn}(\text{OH})_2$ and $\text{Zn}_4(\text{OH})_6(\text{SO}_4)_4 \cdot 4\text{H}_2\text{O}$ phases and FTIR spectroscopy and EDX analysis indicated presence of hydrated zinc borates and $\text{Na Zn}_{1/2} \text{B}_4\text{O}_7 \cdot x\text{H}_2\text{O}$. Using dilute borax decahydrate and dilute

Table 3. The temperature range and the mass % range for the step 1 and step 2 in TG curves in Figure 7 for the samples heated for different periods at 90°C during their preparation.

Heating time minutes	Step 1			Step 2		
	Temperature range (°C)	Mass Range (%)	Mass Loss (%)	Temperature Range (°C)	Mass range (%)	Mass Loss (%)
0	150-300	100-88	12	700-850	84-74	10
30	150-260	100-91	9	650-760	88-84	4
60	150-350	100-93	7	730-940	88-85	3
90	150-350	100-92	8	730-760	91-90	1
120	150-350	100-91	9	730-760	92-91	1

zinc sulfate heptahydrate solutions (0.1 mol dm^{-3}) in the present study resulted in formation of submicron particles since there were not enough borate, zinc and OH^- ions for the growth of the nucleated zinc borate, $\text{Zn}(\text{OH})_2$ and $\text{Zn}_4(\text{OH})_6(\text{SO}_4)_4 \cdot 4\text{H}_2\text{O}$ particles. In studies made with higher of borax concentrations resulted well defined micron sized crystals of $\text{Zn}_3\text{B}_6\text{O}_{12} \cdot 3.5\text{H}_2\text{O}$ [24,40] or $\text{Zn}_2\text{B}_6\text{O}_{11} \cdot 7\text{H}_2\text{O}$ [27]. When boric acid was added to the mixture of aqueous sodium sulfate and borate with excess zinc ions resulted in well-defined crystals of $\text{Zn}_3\text{B}_6\text{O}_{12} \cdot 3.5\text{H}_2\text{O}$ were obtained by sonoc hemical method [40]. Even if the submicron particles obtained in the present study was not pure zinc borate, they can be easily dispersed in mineral oil to increase the lubrication efficiency of the mineral oil for reduction of wear of metal parts as in the study of Savrik et al [26].

4. Conclusions

The formation of chemical garden from zinc sulfate heptahydrate crystals immersed in saturated borax solution was monitored with optical microscope. The formation of the first membrane, the swelling of the crystal by incoming water from the semipermeable membrane and the formation of branches with irregular shapes were observed by optical microscopy. Thus it would be possible to obtain hallow zinc borate fibers by immersing zinc sulfate heptahydrate in saturated borax solution.

The solid reaction products obtained by mixing dilute aqueous borax and zinc sulfate solutions were attempted to be characterized in the present study. Elemental analysis indicated the presence of B, O, Na, S and Zn elements. The $\text{B}_2\text{O}_3/\text{ZnO}$ ratio was changing around 2. Double salt formation was also possible as indicated by the high Na content of the powders. FTIR analysis showed that the ratio of absorbance of asymmetric stretching vibrations of $(\text{B}_{(3)}-\text{O})$ at 1351 cm^{-1} to absorbance of asymmetric stretching vibrations of $(\text{B}_{(4)}-\text{O})$ at 1026 cm^{-1} increased during heating of the powder during its preparation indicating tetrahedral borate ions were transformed to trihedral borate ions. Presence of $\text{Zn}(\text{OH})_2$ and SO_4^{2-} ions in the first precipitate formed was indicated by FTIR analysis. The samples contained $\text{Zn}_4(\text{OH})_6(\text{SO}_4)_4 \cdot 4\text{H}_2\text{O}$ as indicated by TG analysis. X-ray diffraction confirmed the presence of $\text{Zn}(\text{OH})_2$ and additionally presence of $\text{Zn}_4(\text{OH})_6(\text{SO}_4)_4 \cdot 4\text{H}_2\text{O}$. The zinc borate compounds formed were not crystalline or had very small crystals since no sharp x-ray diffraction peaks of zinc borate species were observed. The two mass loss steps at $150-350^\circ\text{C}$ and $700-950^\circ\text{C}$ ranges were due to elimination of water and the decomposition of sulfate ions respectively. The precipitate formed initially had 10% sulfate and the sulfate content decreased to 1% for the sample produced in 90 minutes heating time at 90°C . The precipitated powder from tincal mineral and zinc heptahydrate solution was

not pure. Its composition was changing with heating time during its preparation and it contained $\text{Zn}(\text{OH})_2$, $\text{Zn}_4(\text{OH})_6(\text{SO}_4)_4 \cdot 4\text{H}_2\text{O}$, $\text{Na Zn}_{1/2}\text{B}_4\text{O}_7 \cdot x\text{H}_2\text{O}$ besides zinc borates. The powder could be used as a lubricant additive, since it could be easily dispersed in mineral oil due to 600 nm diameter primary particles.

Acknowledgements

The authors thank to Turkish Scientific and Technological Research Council for supporting this study with project number 105M358.

References

- [1] Barge, L. M., Cardoso, S. S., Cartwright, J. H., Cooper, G. J., Cronin, L., De Wit, A., ... & Thomas, N. L. (2015). From chemical gardens to chemobionics. *Chemical Reviews*, 115(16), 8652-8703.
- [2] Cartwright, J. H., Escribano, B., & Sainz-Díaz, C. I. (2011). Chemical-garden formation, morphology, and composition. I. Effect of the nature of the cations. *Langmuir*, 27(7), 3286-3293.
- [3] Cartwright, J. H., Escribano, B., Khokhlov, S., & Sainz-Díaz, C. I. (2011). Chemical gardens from silicates and cations of group 2: a comparative study of composition, morphology and microstructure. *Physical Chemistry Chemical Physics*, 13(3), 1030-1036.
- [4] Glaab, F., Kellermeier, M., Kunz, W., Morallon, E., & García-Ruiz, J. M. (2012). Formation and evolution of chemical gradients and potential differences across self-assembling inorganic membranes. *Angewandte Chemie*, 124(18), 4393-4397.
- [5] Balköse, D., Özkan, F., Köktürk, U., Ulutan, S., Ülkü, S., & Nişli, G. (2002). Characterization of hollow chemical garden fibers from metal salts and water glass. *Journal of Sol-Gel Science and Technology*, 23(3), 253-263.
- [6] Parmar, K., & Bhattacharjee, S. (2017). Energetically benign synthesis of lanthanum silicate through "silica garden" route and its characterization. *Materials Chemistry and Physics*, 194, 147-152.
- [7] Makki, R., Al-Humiari, M., Dutta, S., & Steinbock, O. (2009). Hollow microtubes and shells from reactant-loaded polymer beads. *Angewandte Chemie*, 121(46), 8908-8912.
- [8] Glaab, F., Rieder, J., Klein, R., Choquesillo-Lazarte, D., Melero-Garcia, E., García-Ruiz, J. M., ... & Kellermeier, M. (2017). Precipitation and crystallization kinetics in silica gardens. *ChemPhysChem*, 18(4), 338-345.
- [9] Bormashenko, E., Bormashenko, Y., Grynyov, R., Pogreb, R., & Schechter, A. (2015). How to grow a movable mini-garden in a droplet: Growing chemical gardens in a water and aqueous ethanol solutions droplets deposited on a superhydrophobic surface. *Colloids and Interface Science Communications*, 7, 12-15.
- [10] Bormashenko, E., Bormashenko, Y., Stanevsky, O.,

- Pogreb, R., Whyman, G., Stein, T., & Barkay, Z. (2006). Template-assisted growth of chemical gardens: Formation of dendrite structures. *Colloids and Surfaces A: Physicochemical and Engineering Aspects*, 289(1-3), 245-249.
- [11] Escamilla-Roa, E., Cartwright, J. H., & Sainz-Díaz, C. I. (2019). Chemobrionic fabrication of hierarchical self-assembling nanostructures of copper oxide and hydroxide. *ChemSystemsChem*, 1(3), e1900011.
- [12] Zhao, W., & Sakurai, K. (2017). Realtime observation of diffusing elements in a chemical garden. *ACS Omega*, 2(8), 4363-4369.
- [13] Schubert, D. M. (2019). Hydrated zinc borates and their industrial use. *Molecules*, 24(13), 2419.
- [14] Eltepe, H. E., Balköse, D., & Ülkü, S. (2007). Effect of temperature and time on zinc borate species formed from zinc oxide and boric acid in aqueous medium. *Industrial & Engineering Chemistry Research*, 46(8), 2367-2371.
- [15] Gao, P., & Zhang, Y. (2015). Synthesis and characterization of zinc borate nanowhiskers and their inflaming retarding effect in polystyrene. *Journal of Nanomaterials*, 2015.
- [16] Gao, Y. H., & Liu, Z. H. (2009). Hydrothermal synthesis and standard molar enthalpy of formation of zinc borate of $4\text{ZnO}\cdot\text{B}_2\text{O}_3\cdot\text{H}_2\text{O}$. *Journal of Chemical & Engineering Data*, 54(9), 2789-2790.
- [17] Gao, Y. H., & Liu, Z. H. (2009). Synthesis and thermochemistry of two zinc borates, $\text{Zn}_2\text{B}_6\text{O}_{11}\cdot 7\text{H}_2\text{O}$ and $\text{Zn}_3\text{B}_{10}\text{O}_{18}\cdot 14\text{H}_2\text{O}$. *Thermochimica Acta*, 484(1-2), 27-31.
- [18] Kipcak, A. S., Senberber, F. T., Derun, E. M., Tugrul, N., & Piskin, S. (2015). Characterization and thermal dehydration kinetics of zinc borates synthesized from zinc sulfate and zinc chloride. *Research on Chemical Intermediates*, 41(11), 9129-9143.
- [19] Kipcak, A. S., Senberber, F. T., Yildirim, M., Yuksel, S. A., Derun, E. M., & Tugrul, N. (2016). Characterization and physical properties of hydrated zinc borates synthesized from sodium borates. *Main Group Metal Chemistry*, 39(1-2), 59-66.
- [20] Kipcak, A. S., Acarali, N., Senberber, F. T., Yildirim, M., Koc, S. N. T., Yuksel, S. A., ... & Tugrul, N. (2016). Synthesis of dehydrated zinc borates using the solid-state method: Characterization and investigation of the physical properties. *Main Group Chemistry*, 15(4), 301-313.
- [21] Shi, X., Li, M., Yang, H., Chen, S., Yuan, L., Zhang, K., & Sun, J. (2007). PEG-300 assisted hydrothermal synthesis of $4\text{ZnO}\cdot\text{B}_2\text{O}_3\cdot\text{H}_2\text{O}$ nanorods. *Materials Research Bulletin*, 42(9), 1649-1656.
- [22] Liang, P., Tuoheti, Z., & Liu, Z. H. (2017). Controlling the structure and morphology of zinc borate by adjusting the reaction temperature and pH value: formation mechanisms and luminescent properties. *RSC Advances*, 7(7), 3695-3703.
- [23] Nies, N. P., & Hulbert, R. W. (1970). U.S. Patent No. 3,549,316. Washington, DC: U.S. Patent and Trademark Office.
- [24] Shi, X., Xiao, Y., Yuan, L., & Sun, J. (2009). Hydrothermal synthesis and characterizations of 2D and 3D $4\text{ZnO}\cdot\text{B}_2\text{O}_3\cdot\text{H}_2\text{O}$ nano/microstructures with different morphologies. *Powder Technology*, 189(3), 462-465.
- [25] Tian, Y., Guo, Y., Jiang, M., Sheng, Y., Hari, B., Zhang, G., ... & Wang, Z. (2006). Synthesis of hydrophobic zinc borate nanodiscs for lubrication. *Materials Letters*, 60(20), 2511-2515.
- [26] Savruk, S. A., Alp, B., Üstün, F., & Balköse, D. Nano Zinc Borate as a Lubricant Additive. *Journal of the Turkish Chemical Society Section A: Chemistry*, 5(1), 45-52.
- [27] Zheng, Y., Tian, Y., Ma, H., Qu, Y., Wang, Z., An, D., ... & Gao, X. (2009). Synthesis and performance study of zinc borate nanowhiskers. *Colloids and Surfaces A: Physicochemical and Engineering Aspects*, 339(1-3), 178-184.
- [28] Polat, S., & Sayan, P. Box-Behnken experimental design for zinc borate $\text{Zn}_2\text{B}_6\text{O}_{11}\cdot 7\text{H}_2\text{O}$. *Journal of Boron*, 5(3), 152-161.
- [29] Akdeniz, Y., Özmihci, F., Duvarcı, O. Ç., Balköse, D., Ülkü, S. (2003, September 3-6). *Kırka tinkel mineralinin sulu çözeltilerindeki kolloidal fazın karakterizasyonu [Characterization of colloidal phase of Kırka tinkel mineral solution in water]*. In 11th Symposium of Clay, İzmir, Turkey.
- [30] Goel, N., Sinha, N., & Kumar, B. (2013). Growth and properties of sodium tetraborate decahydrate single crystals. *Materials Research Bulletin*, 48(4), 1632-1636.
- [31] Jun, L., Shuping, X., & Shiyang, G. (1995). FT-IR and Raman spectroscopic study of hydrated borates. *Spectrochimica Acta Part A: Molecular and Biomolecular Spectroscopy*, 51(4), 519-532.
- [32] Polat, S., & Sayan, P. Effects of polyelectrolytes on the hardness of borax decahydrate crystals. *Journal of Boron*, 4(4), 172-179.
- [33] Steiger, M., & Asmussen, S. (2008). Crystallization of sodium sulfate phases in porous materials: the phase diagram $\text{Na}_2\text{SO}_4\text{-H}_2\text{O}$ and the generation of stress. *Geochimica et Cosmochimica Acta*, 72(17), 4291-4306.
- [34] Top, A., & Çetinkaya, H. (2015). Zinc oxide and zinc hydroxide formation via aqueous precipitation: Effect of the preparation route and lysozyme addition. *Materials Chemistry and Physics*, 167, 77-87.
- [35] Zhou, J., Santambrogio, G., Brümmer, M., Moore, D. T., Wöste, L., Meijer, G., ... & Asmis, K. R. (2006). Infrared spectroscopy of hydrated sulfate dianions. *Journal of Chemical Physics*, 125(11), 111102-111102.
- [36] Linnow, K., Zeunert, A., & Steiger, M. (2006). Investigation of sodium sulfate phase transitions in a porous material using humidity-and temperature-controlled X-ray diffraction. *Analytical Chemistry*, 78(13), 4683-4689.

- [37] Egbuchunam, T., & Balkose, D. (2012). Effect of super-critical ethanol drying on the properties of zinc oxide nanoparticles. *Drying Technology*, 30(7), 739-749.
- [38] Staminirova, T., Petrova, N., & Kirov, G. (2016). Thermal decomposition of zinc hydroxy-sulfate-hydrate minerals. *Journal of Thermal Analysis and Calorimetry*, 125(1), 85-96.
- [39] Bevins, R. E., Turgoose, S., & Williams, P. A. (1982). Namuwite, $(\text{Zn}, \text{Cu})_4\text{SO}_4(\text{OH})_6 \cdot 4\text{H}_2\text{O}$, a new mineral from Wales. *Mineralogical Magazine*, 46(338), 51-54.
- [40] Ersan, A. C., Kipcak, A. S., Ozen, M. Y., & Tugrul, N. (2020). An accelerated and effective synthesis of zinc borate from zinc sulfate using sonochemistry. *Main Group Metal Chemistry*, 43(1), 7-14.



The role of B_2O_3 in lithium-zinc-calcium-silicate glass for improving the radiation shielding competencies: A theoretical evaluation via Phy-X/PSD

Recep Kurtuluş¹, Taner Kavas^{2*}

¹Afyon Kocatepe University, Faculty of Engineering, Department of Materials Science and Engineering, Afyonkarahisar, 03200, Turkey, ORCID orcid.org/0000-0002-3206-9278

²Afyon Kocatepe University, Faculty of Engineering, Department of Materials Science and Engineering, Afyonkarahisar, 03200, Turkey, ORCID orcid.org/0000-0003-1070-8451

ARTICLE INFO

Article history:

Received December 16, 2020

Accepted January 28, 2021

Available online March 31, 2021

Research Article

DOI: 10.30728/boron.841726

Keywords:

B_2O_3
Glass

Gamma-rays

Phy-X/PSD

Radiation shielding

ABSTRACT

In this study, a preliminary theoretical investigation on lithium-zinc-calcium-silicate (LZCS) glass with a composition of $(15-x)Li_2O-10ZnO-10CaO-65SiO_2-xB_2O_3$ where $x: 0, 3, 6, 9, 12$, and 15 mol\% was performed to understand the effect of B_2O_3 on physical, optical, and radiation shielding properties. For this purpose, the L15B0 to L0B15 glass series was designed for evaluating glass density (ρ_{glass}), refractive index (n), mass attenuation coefficient (μ_m), and half-value layer ($\Delta_{0.5}$) parameters. The theoretical calculations showed that the increasing amount of B_2O_3 increased the overall ρ_{glass} from 2.9195 to 2.9865 g/cm³. Further, the addition of B_2O_3 in substitution for Li_2O enhanced the n parameter from 1.6882 to 1.7626. Additionally, BatchMaker software aided to investigate viscosity behavior with the increasing temperature. We found out that the melting point of LZCS glass series ascends with the addition of B_2O_3 , namely from 1309 to 1624 °C. On the other hand, the newly developed Phy-X/PSD software computations paved the way for ascertaining μ_m and $\Delta_{0.5}$. According to the μ_m computations, one can clearly state that an increasing trend is observable against the increasing photon energy, but the L0B15 possessed an enhanced shielding ability than that of the remaining at all photon energies. Moreover, we found out that the $\Delta_{0.5}$ increased with respect to the ascending photon energies, however, the $\Delta_{0.5}$ was effectively improved with the addition of B_2O_3 in the order of L0B15<L3B12<L6B9<L9B6<L12B3<L15B0. Lastly, a comparison for $\Delta_{0.5}$ variations between L0B15 and commercially available RS253 G18 evidently demonstrated that L0B15 achieves 4.11 cm while RS253 G18 fulfills 4.95 which in turn confirms that the proposed glass system can be utilized in radiation shielding applications. All in all, B_2O_3 has promising effects on radiation shielding features in LZCS glass series.

1. Introduction

In today's world, the radiation term has become a major concern among the scientific community since artificial radiation sources have been exponentially increasing with the developing technological areas [1,2]. From medical diagnosis to industrial non-destructive tests, or from food sterilizations to communication systems the humanity has been facing with variety of irradiation including alpha, beta, gamma, or the like [3-5]. In fact, these rays have a strong probability of damage to human health with respect to time, exposure, and duration parameters. DNA mutations, skin burns, or even cancer problems may raise as a result of exposure to these irradiations [6,7]. From this point of view, the usage of a radiation shielding material against incoming rays has become a major action in order to be protected from the above-mentioned health risks.

Radiation shielding material can, therefore, minimize the incoming photon energy thanks to the attenuation characteristics they have, and thus workers and/or patients can be safeguarded [8].

Conceptually, attenuation of incoming photon energy is directly associated with the atomic mass, atomic radius, and density value of the substance used. This is because higher molecular mass or higher atomic radius can contribute enhancing the attenuation competencies of the radiation shielding material, which in turn facilitating the interaction between incoming rays and materials. Within the scope of practically preferred radiation shielding materials, metallic lead finds a broad application area due to its appreciable density value (11.32 g/cm³) [9,10]. The rooms where these devices with the capability of irradiations are placed have been covered with the use of metallic lead in accordance

*Corresponding author: tkavas@aku.edu.tr

with the regulations. Despite the great benefits of metallic lead in terms of advanced attenuating characteristics in particular to the higher photon energies (i.e. gamma-rays), the toxicity issue on humans and the environment has recently begun to be restricted its wide preference [11]. An alternative material, heavy-weight concrete containing aggregates, has become of interest because the building blocks can be fabricated by considering the possible effects of photon energies [12,13]. In fact, heavy-weight aggregates such as barite can be inserted in concrete blends for improving radiation shielding features [14]. Nevertheless, the cracking problem during operation is the primary deficiency of heavy-weight concrete materials. Even though the mentioned problems are valid for these shielding materials the employment has still in progress due to the lack of alternative materials. That's why scientists have extensively been continuing to search for more options.

Glass materials offer spectacular features in many different applications including from daily needs to advanced optical fibers. One of the most essential properties of glass materials is the transparent appearance which metallic lead and heavy-weight concrete could not have. Additionally, compositional flexibility, being environmentally-friendly, well-known melting and shaping techniques, as well as relatively lower production costs make glass materials preferable in radiation shielding applications [15]. Commercially, there are diverse glass types involving silicates, borates, phosphates, and so on. Among these, lithium-zinc-silicate (LZS) glass is regarded as an essential system for various applications such as sealing, dental, and dielectrics. This is because, wide thermal expansion range (5 to $20 \times 10^{-6} \text{ }^{\circ}\text{C}^{-1}$), ability for glass-ceramic formations, relatively good glass viscosity behavior, high electrical insulation, and considerable density values can be obtained with the use of LZS glasses which in turn possessing great potential for radiation shielding applications [16,17]. Furthermore, calcium oxide (CaO) which has a relatively high density value (3.34 g/cm^3) can aid to improve radiation shielding characteristics in the LZS glass system since its positive effect on different glass system has been confirmed by numerous literature studies [18,19]. On the other hand, boron oxide (B_2O_3) can ensure a lot of benefits including low thermal expansion coefficient, facilitating melting conditions, increasing chemical durability, and good glass formation ability [20]. From the perspectives of radiation shielding features, B_2O_3 presents superior shielding abilities, particularly against neutron scatterings. Additionally, Turkey is the leading country in terms of boron reserves, and hence value-added applications involving boron compounds can bring countless benefits both economically and strategically [21, 22]. In conclusion for the selection of LZS glass system and B_2O_3 content, it is worth to investigate the role of B_2O_3 in the LZS glass systems for enhancing radiation

shielding competencies.

Literature is generally focused on the understanding the characteristics of LZS glass system with respect to physical, chemical, mechanical, and thermal properties. However, it is evident that the radiation shielding competencies is lack of investigation, in this regard. From the perspective of lithium-zinc-added glass systems, we come forward numerous studies on radiation shielding properties [23-25]. Moreover, silicate-based glass systems are of interest by many researchers for doping and adding various oxide contents [26-28]. As can be appreciated from the literature works, no further investigations have been made on LZS or LZCS glass systems. Indeed, the role of B_2O_3 in the LZCS glass system has not been experienced both theoretically and experimentally. Therefore, the authors strongly believe that any findings will make difference in the literature for further explorations.

In the present study, a lithium-zinc-calcium-silicate (LZCS) glass system reinforced with B_2O_3 was examined with the use of Phy-X/PSD software. For this, the dopant was designed in the glass system of $(15-x) \text{Li}_2\text{O}-10\text{ZnO}-10\text{CaO}-65\text{SiO}_2-x\text{B}_2\text{O}_3$ where $x: 0, 3, 6, 9, 12$, and 15 mol\% to obtain the L15B0 to L0B15 glass series. Glass density (ρ_{glass}) and refractive index (n) calculations were conducted to determine the possible alterations. Furthermore, viscosity versus temperature profiles was drawn with the use of BatchMaker software for understanding glass melting characteristics. Lastly, a comparison between the LZCS series and commercial radiation shielding materials were done to make a deeper sense for our study. As a result, this study reported the new results on LZCS containing B_2O_3 glass system which has not previously been investigated in the literature studies.

2. Materials and Methods

2.1. Compositional Design

To understand the role of B_2O_3 in LZCS glass system, we designed a distinct composition series as listed in Table 1. L15B0 represents the oxide content with molar percentage for lithium oxide and boron oxide as 15 and 0 mol%, respectively. The remainings are also signified with respect to these codes.

Table 1. The compositional design for LZCS glass system in mol%.

Code	Li_2O	ZnO	CaO	SiO_2	B_2O_3
L15B0	15,00	10,00	10,00	65,00	0,00
L12B3	12,00	10,00	10,00	65,00	3,00
L9B6	9,00	10,00	10,00	65,00	6,00
L6B9	6,00	10,00	10,00	65,00	9,00
L3B12	3,00	10,00	10,00	65,00	12,00
L0B15	0,00	10,00	10,00	65,00	15,00

2.2. Calculations for Physical and Optical Properties

Glass density (ρ_{glass}) parameter plays an essential characteristics on the investigated glass systems. To find out the changes in ρ_{glass} with the insertion of B_2O_3 in LZCS glass system, it is beneficial to apply empirical relation stated by Inaba and Fujino [29] as expressed in Equation 1. Here, M_i , V_i and x_i indicate molecular weight (g/mol), packing density factor (cm^3/mol), and molar fraction of i^{th} component, respectively.

$$\rho = (0.53) \cdot \frac{(\sum M_i \cdot x_i)}{(\sum V_i \cdot x_i)} \quad (1)$$

Another essential parameter, refractive index (n), is the key factor determining optical properties of glass materials. To calculate this parameter, energy band gap (E_g) values of each oxide is employed throughout the Equation 2 [30].

$$\frac{n^2-1}{n^2+2} = 1 - \sqrt{\frac{E_g}{20}} \quad (2)$$

2.3. Glass Viscosity Behavior

Estimating the glass viscosity behavior with respect to temperature changes takes great importance before experimental studies. In literature, there are few works focusing on viscosity alterations for glass systems in the perspective of computational aspects. For this reason, BatchMaker software which utilizes numerous property calculations based on glass oxide contents emerges as an efficient tool for determining viscosity versus temperature profiles [31]. The software takes into consideration the findings of Lakatos et al. [32] and Fluegel [33] in this respect. We employed a calculation set up for our LZCS glass series, and drew viscosity versus temperature profiles to make a deeper understanding on B_2O_3 insertion in substitution for Li_2O .

2.4. Radiation Shielding Computations

Owing to the newly developed user-friendly software, Phy-X/PSD, the radiation shielding parameters can be computed in an efficient way. Within the scope of Phy-X/PSD, one can simply input glass composition and the related glass density to the software. After this, the software begins for computing the variables for figuring out the different radiation shielding parameters [19]. Here, we evaluated some essential parameters including mass attenuation coefficient (μ_m) and half-value layer ($\Delta_{0.5}$). As is known, the μ_m defines the interaction between incoming ray and the matter of unit mass per unit region whereas $\Delta_{0.5}$ indicates the thickness where the energy of incoming photon is attenuated to its half value. Equations 3 and 4 were used

aid to calculate the parameters.

$$\mu_m = \frac{\mu}{\rho_{glass}} \quad (3)$$

where μ is the linear attenuation coefficient, and ρ_{glass} is the overall glass density for each samples.

$$\Delta_{0.5} = \frac{\ln 2}{\mu} \quad (4)$$

3. Results and Discussion

3.1. Physical and Optical Properties

In literature, almost all researchers have identified the one of the most important parameter, glass density (ρ_{glass}). This is because radiation shielding competencies are straight-forwardly associated with the ρ_{glass} value. As a general concept, it is expected to have higher ρ_{glass} value as possible for enhancing the radiation shielding features [34,35]. From this point of view, the authors calculated the theoretical ρ_{glass} values for the examined glass series. On the other hand, refractive index (n) is a measure of the interaction between incident ray and the matter. The incident ray may be encountered with refraction, absorption, or transmission with respect to the interaction phenomenon. We know that the higher the n value for the glass system the more efficient the radiation shielding will [36]. For understanding the possible alteration in n value for our glass systems, we evaluated the theoretical n calculations for each glass samples. Furthermore, since both ρ_{glass} and n parameters have a parallel behavior Figure 1 depicts the changes in these properties with regard to the B_2O_3 addition. One can firmly deduce that both parameters are in increasing trend with the increasing insertion ratio of B_2O_3 . For instance, L15B0 sample has a ρ_{glass} value of 2.9195 g/cm^3 whereas L0B15 sample gains 2.9865 g/cm^3 . This situation may be attributed to the higher molecular mass of B_2O_3 (69.62

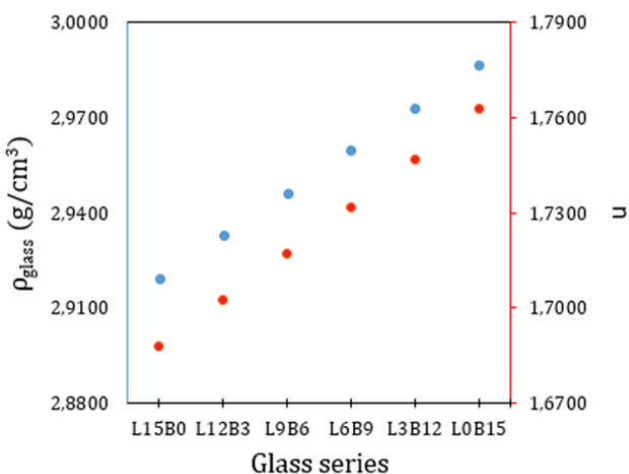


Figure 1. Alteration of ρ_{glass} (blue dots) and n (red dots) with respect to the B_2O_3 addition for the investigated LZCS glass series.

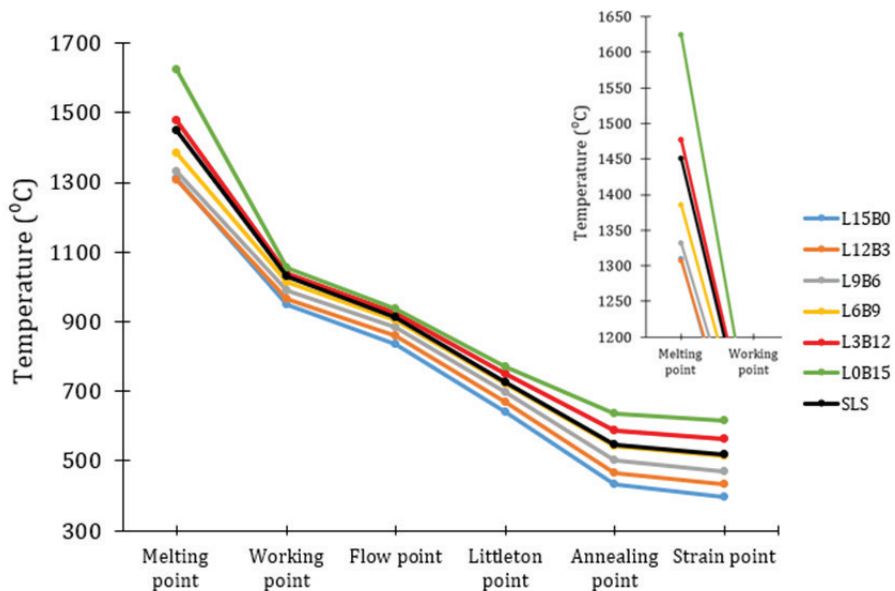


Figure 2. Viscosity versus temperature profiles for the investigated LZCS glass series.

g/mol) in comparison to Li_2O (29.88 g/mol). Similar findings were also stated with some literature studies conducted by [37,38]. On the other hand, the contribution of B_2O_3 in place of Li_2O enhance the n parameter in the order of L0B15>L3B12>L6B9>L9B6>L12B3>L15BO. This is because the E_g value for B_2O_3 -added series are becoming lower, and thus the incident rays could not transmitted throughout the glass substance. In other words, much more incoming photon energy becomes interacted with the glass substance, particularly, herein, boron atoms. Therefore, the insertion of B_2O_3 possesses successful conclusions on both parameters.

3.2. Viscosity versus Temperature Profiles

The investigated LZCS glass series are evaluated in terms of viscosity behaviour with respect to the varying temperature via using BatchMaker software in Figure 2. For making a sensible comments on the behavior of the LZCS series, a well-known glass type as soda-lime-silica (SLS) is also depicted. From the profiles, it is obvious that the increasing amount of B_2O_3 has an adverse effect on melting temperature. To exemplify, L15B0 specimen has a value of 1309°C for melting point whereas L0B15 acquires 1624°C. At this point, SLS glass possesses nearly 1450°C as a melting point. The reason behind this phenomenon may be referred to the glass-forming characteristics of B_2O_3 rather than fluxing agent behavior of Li_2O . The decrease in the amount of fluxing agent in the LZCS glass system ascends the liquidus point through lack of sufficient liquid phase. Therefore, we can report that the insertion of B_2O_3 in substitution for Li_2O in the LZCS glass system elevates the glass melting point.

3.3. Radiation Shielding Features

For highlighting the radiation shielding features of the

examined LZCS glass series, we evaluated the most essential parameters as μ_m and $\Delta_{0.5}$. Figure 3 displays the mass attenuation coefficients (μ_m) with respect to incoming photon energies. It can be observed that the μ_m is found to be in increasing trend as a function of the increasing photon energy. In the lower photon energy levels, i.e. <0.015 MeV, the μ_m values range around 15 cm²/g. However, a sudden decrease can be observable towards the increasing photon energy, i.e. 0.1 MeV. In this case, the μ_m descends through 0.20 cm²/g. For the higher photon energies, i.e. >1 MeV, we gain the μ_m around 0.02 cm²/g. Such a behavior may be attributed to the well-known three mechanisms as photoelectric absorption at low energy, Compton scattering at intermediate energy, and pair production process at high energy. On the other hand, when it comes to evaluate the effect of B_2O_3 in replacement for Li_2O , it is apparent that the B_2O_3 is directly enhancing the μ_m values at all photon energy levels. The μ_m is increased from 0.628 to 0.631 cm²/g with the insertion ratio of B_2O_3 from 0 to 15 mol% at 1.30 MeV. This

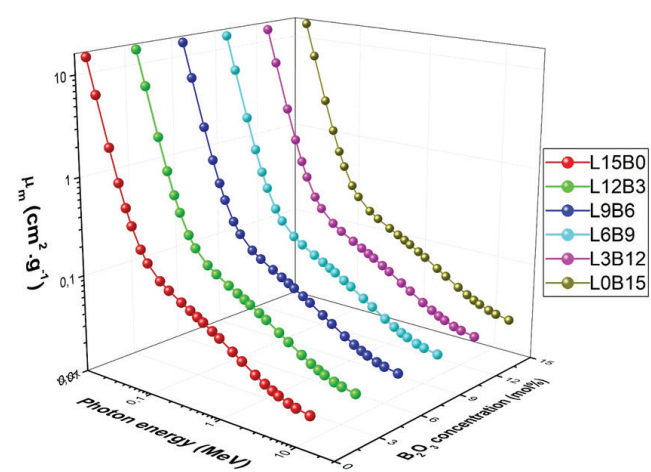


Figure 3. Mass attenuation coefficient of LZCS glass series with respect to photon energies.

increase is associated with the higher density value of B_2O_3 (2.46 g/cm³) than that of Li_2O (2.01 g/cm³). The higher the glass density the better the radiation shielding competencies were confirmed by various studies in the literature [39,40]. Since an increasing trend is required for improving radiation shielding competencies we can report that B_2O_3 can provide this enhancement in an efficient way.

Yet another significant parameter, half-value layer ($\Delta_{0.5}$), signifies the required thickness value to attenuate the half of incoming energy. From this perspective, Figure 4 reveals the variations in $\Delta_{0.5}$ for different photon energies. It is clear that the required thickness value for all LZCS glass series ascends with the increasing photon energy. However, L0B15 dominates over the remaining in all photon energies. For instance, L15B0 requires the $\Delta_{0.5}$ value of 3.39 cm while L0B15 yields 3.30 cm. That means the lesser thickness can attenuate the half of the incoming energy owing to the contribution of B_2O_3 . In fact, the higher molecular mass of B_2O_3 (69.62 g/mol) compared to Li_2O (29.88 g/mol) is the reason facilitating this advancement. Moreover, a comparison between L0B15 and commercial radiation shielding glasses (*i.e.* Schott RS series) can make a better understanding of the figured out $\Delta_{0.5}$ values. Schott RS series have distinct type of glasses for the required photon energies [41]. Here, it may be more plausible to highlight the higher energy levels such as gamma-rays occurred at 1.25 MeV (⁶⁰Co). Besides, it may be more meaningful to select the lead-free RS series such as RS 253 G18 since our LZCS glass series do not contain any lead oxide substance. When it comes to compare $\Delta_{0.5}$ values, L0B15 specimen provides 4.11 cm while RS 253 G18 ensures 4.95 cm. From these values, we can firmly report that L0B15 sample achieves better radiation shielding features than that of commercially available RS 253 G15 glass. Therefore, our glass system can make a difference in a commercial manner.

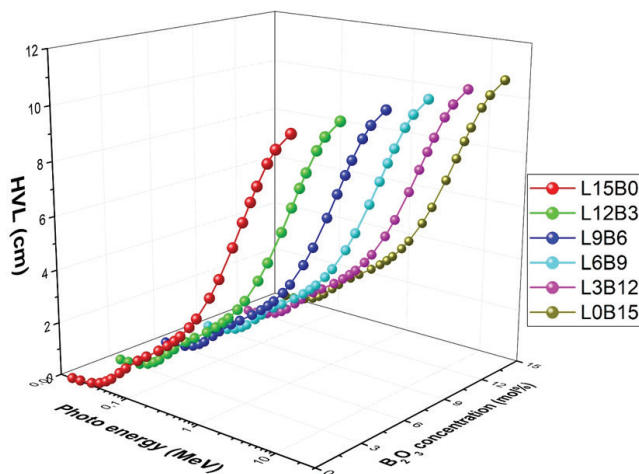


Figure 4. Half-value layer alterations with respect to photon energies for the LZCS series.

4. Conclusions

The present study focused on the theoretical calculations for evaluating the effects of B_2O_3 addition on the physical, optical, and radiation shielding properties of the lithium-zinc-calcium-silicate (LZCS) glass system. For this, $(15-x)Li_2O-10ZnO-10CaO-65SiO_2-xB_2O_3$ where x : 0, 3, 6, 9, 12, and 15 mol% glass system was designed, and L15B0 to L0B15 glass series were examined. The glass density (ρ_{glass}) calculations presented that B_2O_3 insertion is an efficient way to increase the overall ρ_{glass} . Additionally, the refractive index (n) value was enhanced owing to the B_2O_3 contribution. For understanding the viscosity behavior of the investigated glass series, BatchMaker software was utilized. It showed that the addition of B_2O_3 increased the melting point of the glass series due to the glass-forming role. In the perspective of radiation shielding features, the newly developed Phy-X/PSD software provided to compute mass attenuation coefficient (μ_m) and half-value layer ($\Delta_{0.5}$). We found out that the increasing content of B_2O_3 increased the μ_m and decreased the $\Delta_{0.5}$. These alterations ensured to improve radiation shielding characteristics for B_2O_3 -reinforced LZCS series. More essentially, the L0B15 sample can compete with the commercial radiation shielding glass, particularly the lead-free series of RS 263 G18. In conclusion, the authors reported that the insertion of B_2O_3 is a good candidate for the LZCS glass system for the obtainment of advanced physical, optical, and radiation shielding features in comparison to the undoped situation.

References

- [1] Gökmen, U., Özkan, Z., Jamalgzari, L. E., & Ocak, S. B. (2020). Investigation of radiation attenuation properties of Al-Cu matrix composites reinforced by different amount of B4C particles. *Journal of Boron*, 5(3), 124-130.
- [2] Rammah, Y. S., Olarinye, I. O., El-Agawany, F. I., & El-Adawy, A. (2020). Environment friendly La³⁺ ions doped phosphate glasses/glass-ceramics for gamma radiation shielding: Their potential in nuclear safety applications. *Ceramics International*, 46(17), 27616-27626.
- [3] Bektasoglu, M., & Mohammad, M. A. (2020). Investigation of radiation shielding properties of TeO₂-ZnO-Nb₂O₅-Gd₂O₃ glasses at medical diagnostic energies. *Ceramics International*, 46(10), 16217-16223.
- [4] Jawad, A. A., Demirkol, N., Gunoglu, K., & Akkurt, I. (2019). Radiation shielding properties of some ceramic wasted samples. *International Journal of Environmental Science and Technology*, 16(9), 5039-5042.
- [5] Saddeek, Y. B., Issa, S. A., Guclu, E. A., Kilicoglu, O., Susoy, G., & Tekin, H. O. (2020). Alkaline phosphate glasses and synergistic impact of germanium oxide (GeO₂) additive: mechanical and nuclear radiation shielding behaviors. *Ceramics International*, 46(10), 16781-16797.
- [6] Gaikwad, D. K., Sayyed, M. I., Botewad, S. N., Obaid,

- S. S., Khattari, Z. Y., Gawai, U. P., ... & Pawar, P. P. (2019). Physical, structural, optical investigation and shielding features of tungsten bismuth tellurite based glasses. *Journal of Non-Crystalline Solids*, 503, 158-168.
- [7] Aly, P., El-Kheshen, A. A., Abou-Gabal, H., & Agamy, S. (2020). Structural investigation and measurement of the shielding effect of borosilicate glass containing PbO, SrO, and BaO against gamma irradiation. *Journal of Physics and Chemistry of Solids*, 145, 109521.
- [8] Vighnesh, K. R., Ramya, B., Nimutha, S., Wagh, A., Sayyed, M. I., Sakar, E., ... & Kamath, S. D. (2020). Structural, optical, thermal, mechanical, morphological & radiation shielding parameters of Pr³⁺ doped ZAlFB glass systems. *Optical Materials*, 99, 109512.
- [9] Al-Hadeethi, Y., & Sayyed, M. I. (2019). Analysis of borosilicate glasses doped with heavy metal oxides for gamma radiation shielding application using Geant4 simulation code. *Ceramics International*, 45(18), 24858-24864.
- [10] Mirji, R., & Lobo, B. (2017). 24. Radiation shielding materials: A brief review on methods, scope and significance. In *National Conference on 'Advances in VLSI and Microelectronics.'* In PC Jabin Science College, Hubballi, India (pp. 96-100).
- [11] Ara, A., & Usmani, J. A. (2015). Lead toxicity: a review. *Interdisciplinary Toxicology*, 8(2), 55-64.
- [12] Demir, F., Budak, G., Sahin, R., Karabulut, A., Oltulu, M., Şerifoğlu, K., & Un, A. (2010). Radiation transmission of heavyweight and normal-weight concretes containing colemanite for 6 MV and 18 MV X-rays using linear accelerator. *Annals of Nuclear Energy*, 37(3), 339-344.
- [13] Maslehuddin, M., Naqvi, A. A., Ibrahim, M., & Kalakada, Z. (2013). Radiation shielding properties of concrete with electric arc furnace slag aggregates and steel shots. *Annals of Nuclear Energy*, 53, 192-196.
- [14] Saidani, K., Ajam, L., & Ouezdou, M. B. (2015). Barite powder as sand substitution in concrete: Effect on some mechanical properties. *Construction and Building Materials*, 95, 287-295.
- [15] Kurtulus, R., & Kavas, T. (2020). Investigation on the physical properties, shielding parameters, glass formation ability, and cost analysis for waste soda-lime-silica (SLS) glass containing SrO. *Radiation Physics and Chemistry*, 176, 109090.
- [16] Shen, Z., Zhu, L., Zhang, Y., Chen, Y., Yang, D., & Song, X. (2017). Effect of CuO addition on crystallization and thermal expansion properties of Li₂O-ZnO-SiO₂ glass-ceramics. *Ceramics International*, 43(9), 7099-7105.
- [17] Goswami, M., Deshpande, S. K., Kumar, R., & Kothiyal, G. P. (2010). Electrical behaviour of Li₂O-ZnO-SiO₂ glass and glass-ceramics system. *Journal of Physics and Chemistry of Solids*, 71(5), 739-744.
- [18] Al-Hadeethi, Y., Sayyed, M. I., & Rammah, Y. S. (2019). Investigations of the physical, structural, optical and gamma-rays shielding features of B₂O₃-Bi₂O₃-ZnO-CaO glasses. *Ceramics International*, 45(16), 20724-20732.
- [19] Singh, K., Singh, H., Sharma, G., Gerward, L., Khanina, A., Kumar, R., ... & Sahota, H. S. (2005). Gamma-ray shielding properties of CaO-SrO-B₂O₃ glasses. *Radiation Physics and Chemistry*, 72(2-3), 225-228.
- [20] Abouhaswa, A. S., & Kavaz, E. (2020). A novel B₂O₃-Na₂O-BaO-HgO glass system: Synthesis, physical, optical and nuclear shielding features. *Ceramics International*, 46(10), 16166-16177.
- [21] *Boron in the world.* (2020). Etimaden. Retrieved December 15, 2020 from <https://www.etimaden.gov.tr/en/boron-in-the-world>.
- [22] Reserves. (2018). TENMAK BOREN. Retrieved December 15, 2020 from <https://www.boren.gov.tr/Sayfa/reserves/103>.
- [23] Yalcin, S., Aktas, B., & Yilmaz, D. (2019). Radiation shielding properties of Cerium oxide and erbium oxide doped obsidian glass. *Radiation Physics and Chemistry*, 160, 83-88.
- [24] Sayyed, M. I., Lakshminarayana, G., Moghaddasi, M., Kityk, I. V., & Mahdi, M. A. (2018). Physical properties, optical band gaps and radiation shielding parameters exploration for Dy³⁺-doped alkali/mixed alkali multi-component borate glasses. *Glass Physics and Chemistry*, 44(4), 279-291.
- [25] Rashad, M., Ali, A. M., Sayyed, M. I., Somaily, H. H., Algarni, H., & Rammah, Y. S. (2020). Radiation attenuation and optical features of lithium borate glasses containing barium: B₂O₃·Li₂O·BaO. *Ceramics International*, 46(13), 21000-21007.
- [26] Khodadadi, A., & Taherian, R. (2020). Investigation on the radiation shielding properties of lead silicate glasses modified by ZnO and BaO. *Materials Chemistry and Physics*, 251, 123136.
- [27] Çetin, B., Yalcin, S., & Albaşkara, M. (2017). Investigation of radiation shielding properties of soda-lime-silica glasses doped with different food materials. *Acta Physica Polonica A*, 132(3), 988-990.
- [28] Sayyed, M. I., Elmahroug, Y., Elbashir, B. O., & Issa, S. A. (2017). Gamma-ray shielding properties of zinc oxide soda lime silica glasses. *Journal of Materials Science: Materials in Electronics*, 28(5), 4064-4074.
- [29] Inaba, S., & Fujino, S. (2010). Empirical equation for calculating the density of oxide glasses. *Journal of the American Ceramic Society*, 93(1), 217-220.
- [30] Thombare, M., Joat, R., THombre, D., & Mahavidyalaya, V. B. (2016). Glasses study physical properties of sodiumborophosphate. *International Journal of Engineering Science*, 8482.
- [31] *BatchMaker® Batch Calculation & Glass Development.* (2020). ilis GmbH. Retrieved December 15, 2020 from <https://www.ilis.de/en/batchmaker.html>.
- [32] Lakatos, C., Johansson, L. G., & Simmingskold, B. (1972). Viscosity temperature relations in the glass system SiO₂-Al₂O₃-Na₂O-K₂O-CaO-MgO in the composition range of technical glasses. *Glass Technology-European Journal of Glass Science and Technology Part A*, 13(3), 88-95.
- [33] Fluegel, A. (2007). Glass viscosity calculation based on a global statistical modelling approach. *Glass Technology-European Journal of Glass Science and Technology Part A*, 48(1), 13-30.
- [34] Al-Hadeethi, Y., & Sayyed, M. I. (2020). A comprehensive study on the effect of TeO₂ on the radiation shielding properties of TeO₂-B₂O₃-Bi₂O₃-LiF-SrCl₂ glass system using Phy-X/PSD software. *Ceramics In-*

- ternational, 46(5), 6136-6140.
- [35] Al-Hadeethi, Y., Sayyed, M. I., Kaewkhao, J., Askin, A., Raffah, B. M., Mkawi, E. M., & Rajaramakrishna, R. (2019). Physical, structural, optical, and radiation shielding properties of B_2O_3 - Gd_2O_3 - Y_2O_3 glass system. *Applied Physics A*, 125(12), 1-7.
- [36] Wahab, E. A., Shaaban, K. S., & Elsaman, R. (2019). Radiation shielding and physical properties of lead borate glass-doped ZrO_2 nanoparticles. *Applied Physics A*, 125(12), 1-15.
- [37] Susoy, G. (2020). Effect of TeO_2 additions on nuclear radiation shielding behavior of Li_2O - B_2O_3 - P_2O_5 - TeO_2 glass-system. *Ceramics International*, 46(3), 3844-3854.
- [38] Kumar, A. (2017). Gamma ray shielding properties of PbO - Li_2O - B_2O_3 glasses. *Radiation Physics and Chemistry*, 136, 50-53.
- [39] Lakshminarayana, G., Elmahroug, Y., Kumar, A., Dong, M. G., Lee, D. E., Yoon, J., & Park, T. (2020). TeO_2 - B_2O_3 - ZnO - La_2O_3 glasses: γ -ray and neutron attenuation characteristics analysis by WinXCOM program, MCNP5, Geant4, and Penelope simulation codes. *Ceramics International*, 46(10), 16620-16635.
- [40] Al-Hadeethi, Y., Sayyed, M. I., Mohammed, H., & Rimondin, L. (2020). X-ray photons attenuation characteristics for two tellurite based glass systems at dental diagnostic energies. *Ceramics International*, 46(1), 251-257.
- [41] Radiation Shielding Glasses for Industrial Applications. (2020). Schott AG. Retrieved December 15, 2020 from https://www.schott.com/advanced_optics/english/products/optical-materials/specialmaterials/radiation-shielding-glasses/index.html.



Kolemanit katkısının kordiyerit cam-seramiklerin kristalizasyon davranışının üzerindeki etkilerinin araştırılması

Süleyman Akpinar¹, Atilla Evcin^{2*}

¹Afyon Kocatepe Üniversitesi, Mühendislik Fakültesi, Malzeme Bilimi ve Mühendisliği Bölümü, Afyonkarahisar, 03200, Türkiye, ORCID orcid.org/0000-0002-7959-3464

²Afyon Kocatepe Üniversitesi, Mühendislik Fakültesi, Malzeme Bilimi ve Mühendisliği Bölümü, 03200, Afyonkarahisar, 03200, Türkiye, ORCID orcid.org/0000-0002-0163-5097

MAKALE BİLGİSİ

Makale Geçmişti:

İlk gönderi 11 Mart 2020

Kabul 11 Şubat 2021

Online 31 Mart 2021

Araştırma Makalesi

DOI: 10.30728/boron.702171

Anahtar kelimeler:

Cam-seramik

Kordiyerit

Kolemanit

Müllit kristalizasyon

ÖZET

Kordiyerit esaslı cam-seramikler, yüksek termal direnç özelliklerini ile birlikte düşük dielektrik sabiti ve düşük termal genleşme katsayısına sahip mühendislik malzemeleridir. Düşük maliyetlerde üretilmesi ve iyi elektriksel özelliklere sahip olması dolayısıyla, kordiyerit cam-seramikler elektronik endüstrisinde alümina yerine altıkkal malzeme olarak kullanılabilir ve ayrıca çok katmanlı devre kartlarının, katalitik konvertörlerin ve ısı yalıtılmalzemelerinin üretiminde alternatif bir malzeme olarak değerlendirilebilmektedir. Kordiyerit esaslı camlar dar bir sinterleme sıcaklık aralığına ve yüksek viskoziteye sahip olduklarıdan, çekirdeklenme katalisti olmadan 1000°C'nin altında kristalleştirilebilmeleri zordur. Düşük sıcaklıkta ve yüksek yoğunlukta cam-seramiklerin üretimi için viskoziteyi azaltıcı flukslaştırıcı özellikteki ve çekirdeklenmeyi sağlayan katkıların (ZrO_2 , TiO_2 , CeO_2 , Y_2O_3 , CaO , ZnO , P_2O_5 , B_2O_3 gibi) ve miktarlarının seçimi oldukça önem arz etmektedir. Bu çalışmada, kordiyerit sitokiyometrisine uygun bileşimde hazırlanan karışımın camlaşdırıldıktan sonraki kristalleşebilme kabiliyeti üzerinde kolemanit katkısının etkileri araştırılmıştır. Magnezya, kaolen ve kuvars hammaddelerine ağırlıkça % 0, 1, 2 ve 3 oranlarında kolemanit ilavesi ile oluşturulan karışımın endüstriyel koşullarda 1500°C'de ergitilerek sonrasında ani soğutma ile cam yapı elde edilmiştir. Kırmızı ve öğütme işlemlerinden geçirilerek elde edilen cam tozlarının termal analiz tekniği ile camsı geçiş (T_g) ve kristalizasyon (T_c) sıcaklıklarını belirlenmiştir. 1000°C'de yapılan sinterleme sonrasında cam-seramik faz yapısındaki değişimler incelenmiştir.

Investigation of the effects of colemanite addition on the crystallization behaviour of cordierite glass-ceramics

ARTICLE INFO

Article history:

Received March 11, 2020

Accepted February 11, 2021

Available online March 31, 2021

Research Article

DOI: 10.30728/boron.702171

Keywords:

Glass-ceramic

Cordierite

Colemanite

Mullite crystallisation

ABSTRACT

Cordierite based glass-ceramics are engineering materials with high thermal resistance properties, as well as low dielectric constant and low thermal expansion coefficient. Cordierite glass-ceramics can be produced at low costs and have good electrical properties. They can be used as a substrate instead of alumina in the electronics sector, as well as an alternative material in the production of multilayer circuit boards, catalytic converters, and thermal insulation materials. Since cordierite based glasses have a narrow sintering temperature range and high viscosity, it is difficult for them to be crystallized below 1000°C without a nucleation catalyst. For the production of low temperature and high-density glass-ceramics, it is crucial to select the additives (ZrO_2 , TiO_2 , CeO_2 , Y_2O_3 , CaO , ZnO , P_2O_5 , B_2O_3 , etc.) and their amounts that have the fluxing properties that reduce viscosity and provide nucleation. In this study, the effects of colemanite addition on the crystallization ability after vitrification of mixtures prepared in a composition suitable for cordierite stoichiometry were investigated. Colemanite at 0, 1, 2 and 3% wt. ratios were added to the mixtures of magnesia, kaolin, and quartz raw materials were melted at 1500°C in industrial conditions, and then glass structure was obtained by sudden cooling. Glass transition (T_g) and crystallization (T_c) temperatures of glass powders obtained by crushing and grinding were determined by thermal analysis technique. The changes in the phase structure of glass-ceramic after sintering at 1000°C were examined.

*Sorumlu yazar: evcin@aku.edu.tr

1. Giriş (Introduction)

1950'lerin ortalarında keşfedilen cam-seramikler, camın kontrollü çekirdeklenmesi ve kristalizasyonu yoluyla oluşan polikristalin seramik malzemelerdir [1]. Cam-seramikler, uygun bileşimdeki bir cam harmanının kontrollü ısıl işlemler neticesinde kalıntı cam matris içerisinde elde edilen çok kristalli katılar olarak da tanımlanır. Çoğu durumda kristallizasyon prosesi tamamen gerçekleşse de bazı durumlarda küçük kristallerin yanı sıra, ısıl işlem koşullarına ve camın bileşimine bağlı olarak, kalıntı cam fazı da (<%50) bulunmaktadır. ısıl işlem, amorf yapıdaki camdan bir veya daha fazla kristal fazın çekirdeklenmesine ve büyümeye neden olur. Cam-seramiklerin geleneksel çok kristalli seramiklere göre sıfır gözenekli yapıda üretilmeleri, daha iyi termal, mekanik ve kimyasal dirence sahip olmaları gibi bazı önemli avantajları vardır [1,2].

Cam-seramiklerin üretimi için öncelikle istenilen kompozisyonu oluşturacak hammaddelerden homojen bir cam harmanının hazırlanması gereklidir. Mikron altı boyutta kristal fazların gelişimi, yüksek sıcaklıkta kristal büyümeye aşaması öncesi bir çekirdeklenme aşaması ile sağlanır. Bu aşama, iyi mekanik mukavemet için gerekli ince boyutlu kristallerin cam matriste homojen dağılımını sağlamak için dikkatli bir kontrol aşaması gerektirir. Çekirdeklenme, ana cam yapının kontrollü bir oranda ve gerekli sayıda çekirdek oluşana kadar tutulduğu önceden belirlenmiş bir çekirdeklenme sıçaklığına ısitılmasıyla gerçekleştirilir [2,3].

Yeterli çekirdeklenme bölgeleri sağlamak için katalist görevi üstlenen bazı katkı maddeleri gerekebilir. Bu katkı maddeleri çekirdeklenici ajanlar olarak da adlandırılır. Çekirdeklenici ajanların bazı örnekleri TiO_2 , ZrO_2 , ZnO , CaO , B_2O_3 ve P_2O_5 'tir. Çekirdeklenici ajanlar cam içinde çözünür, ancak soğutulduktan veya tekrar ıstıldıktan sonra kristal büyümeyinin meydana gelebileceği çekirdeklenme bölgeleri olarak çökeltilerabilir ve hareket edebilir [2]. Çekirdeklenmenin ardından işlem sıcaklığı kristal fazların optimal büyümeyini sağlamak için artırılır ve hedeflenen kristalleşme derecesine ulaşılınca kadar o sıcaklıkta tutulur. Çekirdeklenme ve kristalleşme için ıstıma rejimleri cam bileşimlerine göre değişir ve aşamaları çekirdek ve kristal büyümeli kontrolünün yanı sıra işlem zamanlarını ve maliyetlerini iyileştirmek için optimize edilebilir [3].

Cam-seramiklerin karakteristik özellikleri, kristallerin türü ve boyutu değiştirilerek, taneler arasında bağlanma, kristal yönü ve kristalleşme derecesi veya yüzdesi ile kontrol edilebilir. Bu özellikler, ana cam bileşimindeki değişiklikler, çekirdeklenme katkı maddesinin seçimi ve ısıl işlem rejiminin ayarlanması ile belirlenebilir [4].

Cam-seramikler genellikle ya tek aşamalı ısıl işlem (çekirdeklenme ve kristal büyümeyinin aynı anda

gerçekleştiği) veya iki aşamalı ısıl işlem (çekirdeklenmenin ardından kristal büyümeyinin gerçekleştiği) kullanılarak ana camdan elde edilir. Camların bazıları homojen, yani hacimsel kristalleşme sergilerken, bazıları da heterojen, yani cam yığınındaki kristallerin çekirdeklenmesinin zor olduğu yüzey çekirdeklenmesi davranışları sergiler [5].

Cam-seramiklerin kristal boyutları genel olarak mikron altı seviyesinde olup ortalama kristal boyutları 20-30 nm dolaylarındadır. Geleneksel seramiklerin aksine cam-seramikler, üretildikleri camın gaz kabarcıklarından tamamen arındırılması dolayısıyla gözenek içermezler. Camdan seramiğe dönüşüm aşamasında gözenek oluşmaz, toplam hacimdeki değişiklik ise çok küçüktür. Çoğu zaman camın seramiğe dönüşümünde hacimsel değişim küçülme şeklinde gerçekleşse de, hacim artışı durumunda bile malzeme içinde gözenekler oluşmaz. Cam-seramiklerde gözeneklerin olmayacağı, iyi özelliklerin gelişmesine yardımcı olan bir özelliktir, çünkü gözenekler, malzemenin yararlı kesit alanını azaltarak mekanik mukavemeti azaltmaktadır [2].

Cam-seramikler fırın altılıkları, sofra takımı, elektrik yalıtkanları, inşaat malzemeleri ve protez malzemeleri gibi uygulamalar için cam şekillendirme teknikleri kullanılarak seri üretilmekte dir [6,7]. Cam-seramikler aynı zamanda yüksek teknoloji uygulamaları için de kullanılır. Örneğin, uçak ve füzeler için radomlar, yoğun atmosferlerde yüksek hızlı uçuş için ısıl şok direnci ve mekanik dayanım gereksinimini karşılayabildiklerinden cam-seramikten imal edilmişdir [2].

Kordiyerit ve kordiyerit esaslı cam-seramikler, düşük termal genleşme, düşük dielektrik sabiti ve yüksek mekanik mukavemet gibi eşsiz özellikler sergilemektedir. Bu tür cam-seramikler radar uygulamalarından elektronik altığa kadar birçok alanda kullanılırlar [8].

Kordiyerit ($2MgO \cdot 2Al_2O_3 \cdot 5SiO_2$), $MgO \cdot Al_2O_3 \cdot SiO_2$ sisteminde yer alan fazlardan birisidir. Kordiyerit, düşük dielektrik sabitine ($\epsilon=4,8-6$), yüksek elektrik direncine ($\rho>10^{12} \Omega cm$) ve çok düşük termal genleşme katsayısına ($\alpha=1-2 \times 10^{-6}/^{\circ}C$) sahiptir [9]. Kordiyeritin bilinen üç polimorfik formu (α , β ve μ -kordiyerit) vardır. Hekzagonal α -kordiyerit (indiyalit) $1450^{\circ}C$ ile $1460^{\circ}C$ arasında stabildir ve yüksek sıcaklık polimorfu olarak da adlandırılır. Ortorombik β -kordiyerit, $1450^{\circ}C$ 'nin altında stabildir ve düşük sıcaklık polimorfu olarak da adlandırılır. Yarı kararlı form olan μ -kordiyerit ise elde edilmesi zor bir fazdır ve $800^{\circ}C$ ile $900^{\circ}C$ arasında kristalleşmesi için saatler gereklidir [10].

İnorganik malzemeler arasında en düşük dielektrik sabitine sahip malzemeler SiO_2 bakımından zengin olanlardır. Kristalin ve amorf formdaki SiO_2 , çok düşük dielektrik sabitine ($\epsilon\approx4$) sahiptir. Ancak, SiO_2 'nın en önemli dezavantajı, sinterleme sonrası soğutma sırasında faz dönüşümlerinin eşlik ettiği büyük hacim değişiklerinden kaynaklı kırılganlığıdır. Kordiyerit, mül-

lit, willemit, diyopsit gibi düşük dielektrik sabitine sahip diğer seramik malzemelerin çoğunun dezavantajı ise yüksek sinterleme sıcaklığıdır. Hem istenen dielektrik hem de mekanik özelliklerin elde edilmesini ve sinterleme sıcaklığının düşürülmesini sağlayan iyi bir çözüm, cam-seramik kompozitlerde seramik bileşenlerin uygun bir cam ile birleştirilmesidir [11].

Kordiyerit ($\epsilon=4,8-6$) ve müllit ($\epsilon=6-7,2$), düşük dielektrik sabitli cam-seramik kompozitlerin seramik bileşenleri için en iyi adaylardır. Kordiyeritin ıslı genleşme katsayısı $1-2 \times 10^{-6}/^{\circ}\text{C}$ iken, müllitin ıslı genleşme katsayısı $4,5-6 \times 10^{-6}/^{\circ}\text{C}$ dir [11]. Kordiyeritin ıslı, kimyasal ve elektriksel olarak üstün özelliklerine rağmen, bazı yüksek sıcaklık uygulamalarında yetersiz mekanik özellikler gösterir, diğer yandan göreceli yüksek ıslı genleşme katsayısı nedeniyle müllit bazı uygulamalar için düşük ıslı şoka dayanım gösterir. Ayrıca, düşük dielektrik sabiti, yüksek elektrik direnci ve iyi termo-mekanik özellikleri ile kordiyerit, elektronik endüstrisinde alümina substratların ($\epsilon=9-10$) yerini almaya uygun bir aday malzemedir, ancak silikon çip ile karşılaşıldığında çok düşük termal genleşme katsayısı bir dezavantajdır. Bu da, olası yonga ayrılımasına ve cihaz arızasına neden olabilir. Müllitin kordiyerite eklenmesinin, kompozit malzemelerin ıslı genleşme katsayısının silikonla eşleşecek şekilde daha iyi uyarlanması izin verdiği ve ayrılma sorunlarını önlediği görülmüştür [12]. Ayrıca, uygun oranlarda müllit ve kordiyeritin mikroyapıda birlikte bulunması yoğunlaşmayı kolaylaştırır, gözenekliliği azaltır ve kompozitin mekanik özelliklerini iyileştirir. Bu tür kompozitler, silikonunkine çok yakın olan düşük dielektrik sabiti ($4,7-5,8$) ve düşük ıslı genleşme katsayısı ($3,8-4,2 \times 10^{-6}/^{\circ}\text{C}$) nedeniyle elektronik paketlenme malzemesi için umut vericidir [11].

Ancak, bu iki malzemenin yüksek refrakterliği nedeniyle, kordiyerit-müllit kompozitlerinin geleneksel sinterleme yolu ile üretimi zordur. Sinterleme katkıları, kompozit malzemenin termal ve elektriksel özelliklerini olumsuz etkileyebilir. Cam-seramik üretim süreci, kordiyerit-müllit kompozitlerinin üretimi için çok ilginç bir alternatif sunabilir, çünkü bu süreçte gözenekliliğin ortadan kaldırılması, tane büyümesinin engellenmesi ve mikroyapısal özelliklerin kontrolü sayesinde sorunlar daha kolay ve etkili bir şekilde çözülebilir [12].

Mikro elektronik sistemler için paketleme yöntemlerinden birisi olan "Düşük sıcaklıkta beraber sinterlenen seramik (LTCC)" uygulamaları esas olarak $\text{MgO-Al}_2\text{O}_3-\text{SiO}_2$, $\text{CaO-Al}_2\text{O}_3-\text{SiO}_2$, $\text{CaO-B}_2\text{O}_3-\text{SiO}_2$ vb. cam-seramik sistemlerine dayanmaktadır. Kordiyerit esaslı cam-seramikler, düşük dielektrik sabiti ve tek kristal silikonun termal genleşme katsayısına uyumluluğu nedeniyle LTCC uygulamaları için ilgi çekici malzemelerdir. Ancak, kordiyerit camlar yüksek erime sıcaklığına ($\geq 1600^{\circ}\text{C}$), yüksek viskoziteye ve dar bir sinterleme sıcaklık aralığına sahip olduğundan 1000°C 'nin altında yoğun cam-seramik eldesi zordur

[13-15]. Yüksek mekanik dayanım ve düşük dielektrik sabiti değeri elde etmek için tam yoğunlaştırma gereklidir. Bununla birlikte, μ -kordiyerit oluşumu, cam-seramığın mekanik, termal ve dielektrik özelliklerini kötüleştirir. Bu nedenle, düşük sıcaklıkta tamamen yoğunlaşmış α -kordiyerit cam-seramik eldesinde sinterleme kabiliyetini geliştirmek için sinterleme yardımcılarının eklenmesi ve stokiyometrik olmayan camların kullanılmasıyla ilgili araştırmalar yapılmıştır [14]. Cam tozlarının sinterlenmesi viskoz akışla ilerlediğinden, azalan cam viskozitesi sinterlenebilirlik üzerinde iyi bir etki gösterir. Yoğun cam-seramik üretimi için, uygun cam bileşimi ve cam viskozitesini azaltan eriyik seçimi kritik bir faktördür [15]. Literatürde, kordiyerit cam-seramiklerin çekirdeklenme, kristalizasyon ve düşük sıcaklıkta sinterleme davranışları üzerine ZrO_2 [16], TiO_2 [17], CeO_2 [18,19], Y_2O_3 [19, 20], CaO [15,21], ZnO [22,23], P_2O_5 [24], Na_2O [25] ve B_2O_3 [26] gibi katkıların etkileri araştırılmıştır.

Chen çalışmasında [15], CaO içeren $\text{MgO-Al}_2\text{O}_3-\text{SiO}_2$ sistemindeki cam-seramiklerin sinterleme ve kristalleşme davranışlarını incelemiştir. MgO 'nın CaO ile değiştirilmesi cam-seramiklerin erime sıcaklığını (T_e) ve camsı geçiş sıcaklığını (T_g) azaltmıştır. Kristalize α -kordiyerit ve az miktarda anortit içeren tam yoğun cam-seramik, düşük bir sıcaklıkta ($\leq 900^{\circ}\text{C}$) başarıyla üretilmiştir. Düşük sıcaklıkta sinterlenebilirlik, düşük termal genleşme katsayısı, yüksek eğilme dayanımı ve düşük dielektrik özellikler, ağırlıkça %5 CaO içeren $\text{MgO-Al}_2\text{O}_3-\text{SiO}_2$ sistemindeki cam-seramik tozundan hazırlanan yoğun numunede başarıyla elde edilmiştir.

Chen ve Liu çalışmasında [23], $\text{MgO-Al}_2\text{O}_3-\text{SiO}_2$ cam sistemini incelemiştir ve ZnO katkısının camın erime ve kristalleşme sıcaklıklarını azalttığını gözlemlemiştir. İnceленen cam sistemindeki en önemli kristal fazlardan birisinin willemit (Zn_2SiO_4) olduğu ve willemit fazının yaklaşık $2,6 \times 10^{-6}/^{\circ}\text{C}$ gibi düşük bir termal genleşmeye sahip olması ile LED uygulamaları için uygun olduğu rapor edilmiştir.

Oprea ve arkadaşları [27], kaolinit, kalsine alümina ve talktan hazırlanan karışımlara ilave edilen TiO_2 , ZrO_2 , CeO_2 gibi bazı çekirdeklesitici ajanların kordiyerit cam-seramığın ıslısal genleşme katsayısını değerini azalttığını tespit etmişlerdir. Sarıgül ve Günay [26] çalışmasında, kaolin, talk ve alümina karışımına %3'e kadar B_2O_3 ilavesinin kordiyerit cam-seramığın camsı geçiş sıcaklığını (T_g) artttığını ve termal genleşme katsayısını da azalttığını tespit etmişlerdir.

Torres ve Alarcón [29], $\text{CaO-MgO-Al}_2\text{O}_3-\text{SiO}_2$ cam sisteminde B_2O_3 katkısının α -kordiyerit kristalizasyonu üzerindeki etkisini araştırmışlardır. B_2O_3 katkısının kristalleşme öncesi viskoz akışla yoğunlaştırmayı kolaylaştırarak μ -kordiyerit oluşumunu baskıladığı ve α -kordiyerite dönüşümde olumlu etki yaptığı belirtilmiştir. 1160°C 'de ısıtılan camdaki α -kordiyerit kristal-

leşme oranı yaklaşık %70 olarak tespit edilmiş ve artık cam fazındaki hekzoganal α -kordiyerit kristallerinin 3 μm dolaylarında olduğu rapor edilmiştir. Aynı yazarlar bir başka çalışmasında [30], $\text{CaO}-\text{MgO}-\text{Al}_2\text{O}_3-\text{SiO}_2$ sisteminde oluşan kristal fazları anortit, kordiyerit, müllit ve diyopsit fazları olarak tanımlamışlardır.

Synkiewicz ve arkadaşlarının çalışmasında [31], kordiyerit, $\text{CaO}-\text{B}_2\text{O}_3-\text{Al}_2\text{O}_3-\text{SiO}_2$ camı ve grafit içeren bir süspansiyondan şerit döküm/laminasyon/pişirme yöntemiyle üretilen çok katmanlı LTCC yapıları için, 1 MHz'de dielektrik sabiti (ϵ) 3-5,6 olarak rapor edilmiştir. Bu düşük dielektrik sabiti değeri LTCC malzemelerde silikonunkine çok benzerlik göstermektedir.

Torres ve arkadaşları [32], $\text{CaO}-\text{MgO}-\text{Al}_2\text{O}_3-\text{SiO}_2$ sistemindeki bir cam bileşiminde Al_2O_3 'ün B_2O_3 ile yer değiştirmesinin etkisi incelenmiştir. Artan bor oksit miktarı ile camların erime özelliklerinin iyileştiği görülmüş ve %6'dan fazla B_2O_3 içerikli camlarda 1160°C'de hızlı ısıtma ile sadece müllitin kristalleştiği görülmüştür. 1160°C'de hızlı ısıtılan %9 B_2O_3 içeren camda gelişen müllit fazı miktarı Rietveld analizi ile %19,5 olarak belirlenmiştir.

Wu ve Hwang çalışmasında [33], kordiyerit cama B_2O_3 ilavesinin artık camın kristalleşmesini ve μ -kordiyeritin α -kordiyerite dönüşümünü teşvik ettiğine dikkat çekmişlerdir.

Literatür çalışmalarında elde edilen bulgular özellikle B_2O_3 'ün kordiyerit cam-seramiklerin kristalizasyon davranışını üzerinde olumlu etkileri olduğunu göstermektedir. Literatür bulguları CaO 'un da kordiyerit esaslı cam-seramiklerin erime sıcaklığını ve camsı geçiş sıcaklığını azaltmasına dikkat çekmektedir. Ayrıca B_2O_3 'ün μ -kordiyeritin α -kordiyerite dönüşümünü ve cam-seramik yapısında kordiyerite ilaveten müllit fazı oluşumunu da desteklediği anlaşılmıştır. Tüm bu bulgular özellikle mikro elektronik endüstrisinde LTCC uygulamaları için düşük dielektrik ve termal genleşme katsayısına sahip ve mekanik olarak dayanıklı kordiyerit-müllit kompozit cam-seramiklerin üretiminin kordiyerit stokiyometrisindeki cam bileşimine B_2O_3 ve CaO katkıları ile mümkün olabileceği göstermiştir. Ancak kordiyerit sitokiyometrisindeki cam bileşimine B_2O_3 ve CaO katkılarının birlikte gerçekleştirildiği ve kristalleşme davranışının incelendiği bir çalışmaya literatürde rastlanılmamıştır. Bu çalışmada ise literatür çalışmalarından farklı olarak bor oksit (B_2O_3) ve kalsiyum oksit (CaO) kaynağı olarak kolemanit hammaddesinin kordiyerit cam-seramiklerin eldesinde camsı geçiş sıcaklığı ve kristalizasyon sıcaklıklarını üzerine etkileri araştırılmıştır.

2. Malzemeler ve Yöntemler (Materials and Methods)

2.1. Hammaddeler (Raw Materials)

Bu çalışmada kordiyerit esaslı cam-seramik malzeme

üretimi için seramik fabrikalarından temin edilen Kaojen ve Kuvars ile Konya-Krom Manyezit işletmesinden temin edilen Sinter Magnezya hammaddeleri kullanılmıştır. Katkı maddesi olarak ise Eti Maden İşletmeinden temin edilen 75 mikron altı tane boyutuna sahip Kolemanit hammaddesi kullanılmıştır. Deneysel çalışmalarda kullanılan hammaddelerin kimyasal bileşimi ve bazı özellikleri Tablo 1'de sunulmuştur.

Tablo 1. Hammaddelerin kimyasal bileşimleri ve bazı özellikleri (Chemical composition and some properties of raw materials).

Oksit (%)	Kaolen	Magnezya	Kuvars	Kolemanit
SiO_2	47,30	3,23	97,50	4,00
Al_2O_3	36,30	0,17	1,21	0,40
Fe_2O_3	0,85	0,49	0,05	0,08
TiO_2	0,05	-	0,05	-
CaO	0,10	3,73	0,02	27,00
K_2O	2,29	-	0,03	-
Na_2O	0,05	-	0,02	0,50
MgO	0,38	92,31	0,48	3,00
B_2O_3	-	-	-	40,00
<hr/>				
Kızdırma Kaybı	12,21	-	0,28	25,00
Tane boyutu (d₅₀)	5,57	23,34	15,83	-
Yüzey Alanı (m²/g)	11,8	1,98	0,59	-

2.2. Reçeteler (Recipes)

Kordiyerit cam-seramik üretiminde kullanılan hammaddelerin karışım oranı kordiyerit sitokiyometrisine ($2\text{MgO} \cdot 2\text{Al}_2\text{O}_3 \cdot 5\text{SiO}_2$) uygun olarak tasarlanmıştır. Bu tasarımda hammaddelerin bileşimindeki sadece MgO , Al_2O_3 ve SiO_2 dikkate alınmıştır. Magnezya, kaolen ve kuvars içeren üçlü karışıntılar, hem teorik kordiyerit bileşimindeki oksit oranlarına ve hem de hammaddelerin kimyasal bileşimine (Tablo 1'de görüldüğü gibi) bağlı olarak hazırlanmıştır. Teorik hesaplamaya ilişkin olarak, karışımındaki $\text{MgO}:\text{Al}_2\text{O}_3:\text{SiO}_2$ ağırlık oranı 13,7:34,9:51,4 olarak belirlenmiştir. Başlangıç hammaddeleri olarak, karışıntıların hazırlanmasında ağırlıkça %82,71 Kaolen, %12,42 Magnezya ve %4,87 Kuvars hammaddeleri kullanılmıştır.

Kordiyerit sitokiyometrisine göre oluşturulan karışımlara ağırlıkça %0, 1, 2 ve 3 oranlarında kolemanit hammaddesi ilave edilerek katkılı reçeteler oluşturulmuştur. CaO ve B_2O_3 cam-seramik üretiminde çekirdeklenme katalisti/flukslaştırıcı olarak etkileri ayrı ayrı araştırılmış olması ve ayrıca her iki oksitin seramik sırlarında ergitici özellikleri dolayısıyla kullanılması bu çalışmada her iki oksitin cam-seramik üretimindeki etkilerini incelemek için itici güç oluşturmuştur. Kolemanit, bileşiminde CaO ve B_2O_3 oksitlerini birlikte bulundurması nedeni ile bu çalışma ile kordiyerit cam-seramik üretiminde ilk kez kullanılmış ve etkileri araştırılmıştır. Kolemanit katkısı ile oluşturulan reçetelerin karışım oranları Tablo 2'de sunulmuştur.

Tablo 2. Kordiyerit cam-seramik üretimi için oluşturulan reçeteler
(Recipes for cordierite glass-ceramic production).

Hammadde	R0	R1	R2	R3
Kaolen (%)	82,71	81,88	81,06	80,23
Magnezya (%)	12,42	12,30	12,17	12,05
Kuvars (%)	4,87	4,82	4,77	4,72
Kolemanit (%)	0	1	2	3

2.3. Cam-Seramik Üretimi (Glass-Ceramic Production)

Kolemanit katkısının kordiyerit cam-seramiklerin camı geçiş (T_g) ve kristalleşme (T_c) sıcaklıklarını üzerindeki etkilerini araştırmak için kordiyerit sitokiyometirisine uygun oranda karıştırılan başlangıç hammaddelerine %0, 1, 2 ve 3 kolemanit ilavesi ile katkılı reçeteler oluşturulmuştur. Hammaddeler tırtımları alındıktan sonra kuru olarak karıştırılmıştır. Hazırlanan nihai karışımalar alümina pota içerisinde doldurularak Gizem Frit (Sakarya, Türkiye) fabrikasına ait fritteştirme fırınında ergitilmiştir. Ergitme sıcaklığı, katkısız karışım için daha önceden DTA-TG analizi ile 1440°C olarak belirlenmiş ve tüm karışımaların homojen bir eriyik hale dönüştürilebilmesi için 1500°C olarak seçilmiştir. Pota içerisindeki eriyik haldeki karışımalar sonrasında anı soğutma ile soğutularak cam yapı elde edilmiştir. Şekil 1'de elde edilen cam yapı görülmektedir.



Şekil 1. Kolemanit katkılı kordiyerit esaslı karışımın 1500°C'de ergitte sonrası anı soğutma ile elde edilen cam yapı görüntüsü (Glass structure image of colemanite-added cordierite-based mixture obtained by instant cooling after melting at 1500°C).

2.4. Karakterizasyon (Characterization)

Ergitilerek oda sıcaklığına soğutulmuş kolemanit katkılı camlar, dijital mikroskop altında görüntüleri çekilerek karşılaştırılmış olarak görünüşteki farklılıklar incelenmiştir. Daha sonra, cam örneklerin Arşimed prensibiyle yoğunlukları hesaplanmıştır. Yoğunlık hesaplamaları için cam numunelerin kütlesi öncelikle hava ortamında kuru ağırlıkları tırtılarak ölçülmüştür. Daha sonra saf su içerisinde daldırılan cam numunelerin su içindeki

ağırlıkları ölçülmüştür. Cam örneklerin havadaki ağırlığının, hava ve su ortamındaki kütle farkına oranlanması ve sonrasında saf suyun yoğunluk değeri ile çarpımı sonrası cam örneklerinin yoğunlukları hesaplanmıştır.

Karakterizasyon çalışmaları için cam örnekleri bilyalı dejirmende etanol ortamında 1 saat süre ile tane boyutları 100 mikron altı inceliğe öğütülmüştür. Öğütme işlemi sonrası tozlar kurutma işlemeye tabi tutulmuştur. Kurutulmuş cam tozlarının Netzsch marka Diferansiyel Taramalı Kalorimetre (DSC) cihazı ile 20°C ısıtma hızında normal atmosfer koşullarında 1250°C'ye kadar ısıtılarak camsı geçiş (T_g) ve kristalizasyon sıcaklıkları (T_c) belirlenmiştir. DSC analizi ile kristalleşme başlangıç sıcaklığı belirlenen cam tozlarından kuru presleme yöntemiyle tablet numuneler şekillendirilmiş (Şekil 2) ve DSC analizi ile belirlenen uygun bir kristalleşme sıcaklığında sinterleme ile ıslı işlem uygulanmıştır. Pişirme işlemi sonrasında numunelerdeki kristal faz oluşumu X-işınları kırınımı (XRD) analizleri ile incelenmiştir. Analizler Bruker marka D8 Advance model cihazda 2θ tarama açısı 5-70° arasında, Cu Ka=1,54 Å dalga boynuna sahip X-işını kullanarak ve 0,02 derece/dakika tarama hızı şartlarında gerçekleştirilmiştir.

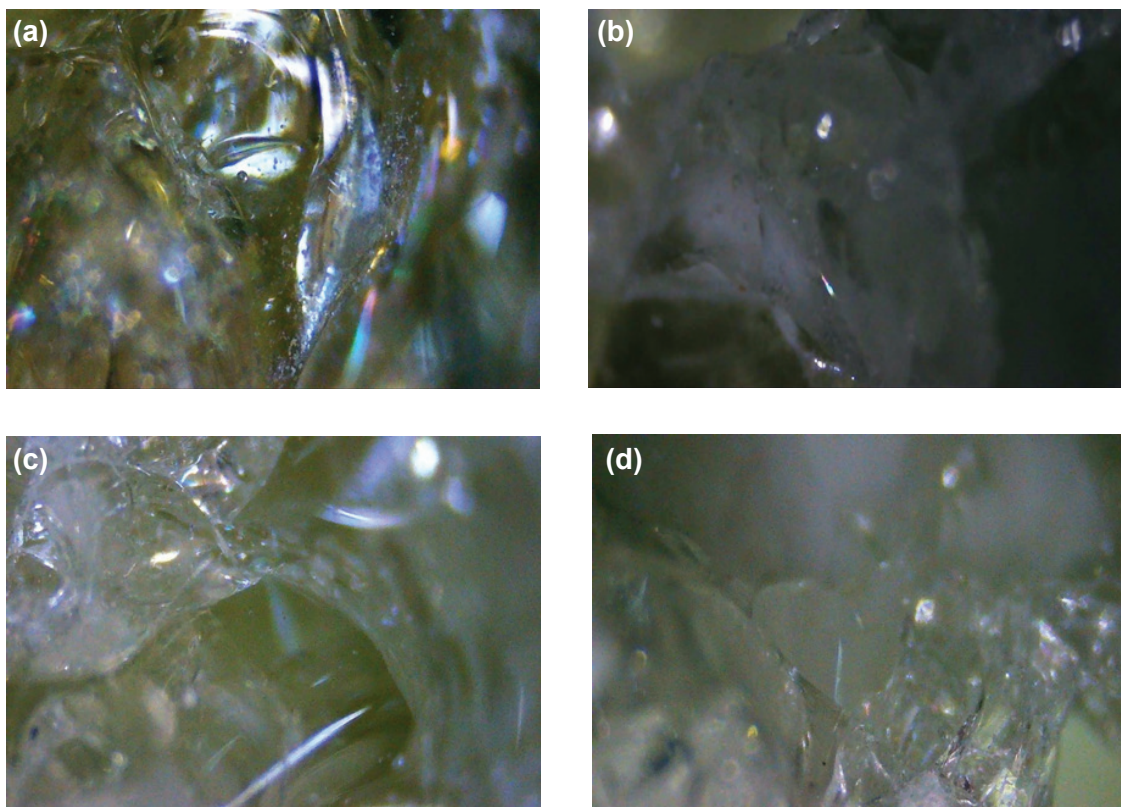
3. Sonuçlar ve Tartışma (Results and Discussion)

Kolemanit katkılı cam örneklerin Inskam-315 dijital mikroskop (40X, 7 inch IPS HD display, 4032x3024 P) altında çekilen görüntüleri Şekil 3'de verilmiştir. Mikroskop görüntülerinden R0 kodlu katkısız cam örneğinin transparan görünümde, kolemanit katkılı R1, R2 ve R3 kodlu cam örneklerinin ise kısmen opak görünümde olduğu anlaşılmıştır.

Kolemanit katkılı cam örneklerinin Arşimed prensibiyle hesaplanan yoğunluk değerleri sırası ile, katkısız cam örneği için (R0) 2,55 g/cm³, %1 kolemanit katkılı cam örneği için (R1) 2,45 g/cm³, %2 kolemanit katkılı cam örneği için (R2) 2,46 g/cm³ ve %3 kolemanit katkılı



Şekil 2. Kolemanit katkılı kordiyerit esaslı cam tozlarının sinterleme sonrası görüntüleri (Images of colemanite-added cordierite-based glass powders after sintering).



Şekil 3. Kolemanit katkılı cam örneklerin mikroskop görüntüler; a) R0, b) R1, c) R2, d) R3 (Microscope images of colemanite-added glass samples).

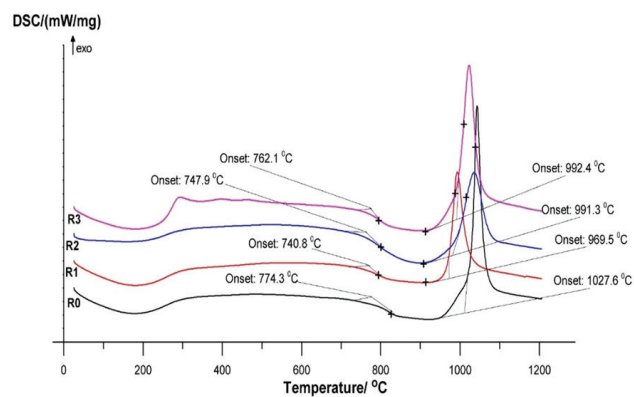
cam örneği için (R3) $2,51 \text{ g/cm}^3$ 'dür. Kolemanit katkılı cam örneklerinde yoğunluk değerlerinin $2,45\text{-}2,55 \text{ g/cm}^3$ aralığında değiştiği, kolemanit katkısı ile birlikte önce azaldığı, sonra ise katkısız cam yoğunluğu degerine doğru arttığı görülmüştür.

3.1. Diferansiyel Taramalı Kalorimetri (DSC) Analizi (Differential Scanning Calorimetry Analysis)

Kordierit bileşiminde hazırlanan cam örneklerinin camsı geçiş ve kristalleşme sıcaklıklarını belirleyebilmek için yapılan DSC analizi sonuçları Şekil 4'de verilmiştir. Şekilde görüldüğü gibi kolemanit katkısı ile numunelerin camsı geçiş sıcaklıklarının %2 katkısına kadar azaldığı belirlenmiştir. %2 katkısından itibaren camsı geçiş sıcaklıklarının arttığı görülmektedir. Katkısız kordierit numunesinin camsı geçiş sıcaklığı (T_g) $774,3^\circ\text{C}$ olarak ölçülmüş iken kolemanit katkılı numunelerin T_g sıcaklıkları sırası ile $740,8^\circ\text{C}$ (%1 katkılı), $747,9^\circ\text{C}$ (%2 katkılı) ve $762,1^\circ\text{C}$ (%3 katkılı) olarak belirlenmiştir. Tablo 3'de numunelerin ölçülen cam geçiş sıcaklıkları (T_g) ve kristalizasyon sıcaklıkları (T_c) ayrıntılı olarak verilmiştir.

Cam örneklerinin kristalizasyon sıcaklıklarını incelediğinde camsı geçiş sıcaklığına benzer şekilde %2 kolemanit katkısına kadar kristalleşme sıcaklığının azaldığı ve bu katkı miktarından sonra tekrar artmaya başladığı belirlenmiştir. Tablo 3'de görüldüğü gibi katkısız cam numunenin kristalizasyon sıcaklığı 1027°C den %1 kolemanit katkısı ile $969,5^\circ\text{C}$ 'ye azaldığı ve böylece %1 oranında kolemanit katkısının cam-seramik kristalleş-

me sıcaklığını yaklaşık 60°C azalttığı anlaşılmıştır. %1'den fazla kolemanit ilavesinde ise katkısız haldekiye göre kristalleşme sıcaklığında yine de azalma gözlenmekle birlikte ($\sim 35^\circ\text{C}$) katkı madde miktarı arttıkça katkısız cam örneğin kristalleşme sıcaklığına doğru yaklaşığı anlaşılmaktadır. Sonuç olarak %1



Şekil 4. Kolemanit katkılı cam örneklerinin DSC grafikleri (DSC graphs of colemanite-added glass samples).

Tablo 3. Kolemanit katkılı cam örneklerinin cam geçiş (T_g) ve kristalizasyon (T_c) sıcaklıkları (T_g and T_c temperatures of colemanite-added glass samples).

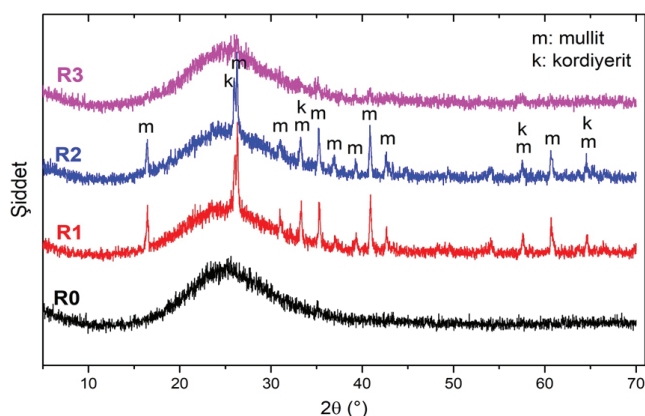
Numune Kodu	T_g , ($^\circ\text{C}$)	T_c , ($^\circ\text{C}$)
R0	774,3	1027,6
R1	740,8	969,5
R2	747,9	991,3
R3	762,1	992,4

kolemanit katkısının kordiyerit esaslı cam-seramik malzemenin hem camsı geçiş sıcaklığını hem de kristalleşme sıcaklığını azalttığı belirlenmiştir.

Literatürdeki benzer konulu çalışmalarında, kordiyerit esaslı cam sisteminde CaO [15], ZnO [16] ve CeO_2 [19] katkılarının camdan seramiğe geçişteki T_g sıcaklığını azaltırken B_2O_3 ve Y_2O_3 katkılarının ise arttırdığı belirtilmiştir. Bu çalışmada ise B_2O_3 ve CaO içerikli kolemanit katkısının düşük oranda (%1) kullanıldığından T_g sıcaklığını azalttığı ancak %2 ve üzeri katkı oranında kullanıldığından ise arttırdığı görülmüştür. Bu sonuç, kolemanit bileşimindeki B_2O_3 'ün T_g sıcaklığını artan yönde CaO 'nın ise azalan yönde etkilediğini ortaya koymaktadır. Literatür bulgularında ZnO [23] ilavesi ile kordiyerit esaslı cam-seramiklerin kristalizasyon sıcaklığı (T_c) azalırken, CeO_2 [19], Y_2O_3 [20] ve CaO [21] ilaveleri ile kristalizasyon sıcaklığının arttığı sonucuna ulaşılmıştır. Bu çalışmadaki %2 ve üzeri oranda kolemanit katkısı ile T_c sıcaklığının artışı irdelendiğinde, kolemanitteki CaO 'nın bu artışta etkili olduğu söylenebilir. Diğer yandan, %1 kolemanit katkısında en düşük T_c değerinin elde edilmesinde de B_2O_3 'ün etkili olduğu düşünülebilir.

3.2. X-Işınları Kırınımı (XRD) Analizi (X-ray Diffraction Analysis)

Cam-seramik yapısında elde edilen numunelerin DSC analizleri ile belirlenen kristalizasyon sıcaklıklarına dayanarak cam tozlarından şekillendirilmiş tabletler 1000°C'de sinterlendikten sonra numunelerin faz yapısının belirlenmesi için XRD analizleri yapılmıştır. Kolemanit katkılı cam-seramik örneklerinde tespit edilen kristalin fazlar Şekil 5'deki XRD sonuçlarında verilmiştir.



Şekil 5. Kolemanit katkılı cam-seramiklerin X-işınları kırınımı (XRD) analiz sonuçları (X-ray diffraction (XRD) analysis results of colemanite-added glass-ceramics).

XRD analizlerine göre faz analizi değerlendirmesi yapıldığında 1000°C'de sinterleme sonrası katkısız cam örneğinin kristalleşmediği görülmektedir. Kolemanit katkısı ile % 1 ve 2 katkılarında kristalleşmenin gerçekleştiği ancak %3 katkısında ise kristalleşmenin

katkısız cam örneğinde olduğu gibi gerçekleşmediği görülmektedir. Bu sonuçlar hem DSC analizi ile belirlenen kristalleşme sıcaklıklarını hem de %2'ye kadar kolemanit ilavesinin kordiyerit cam-seramik eldesinde kristalleşme sıcaklığını azalttığını doğrulamaktadır. XRD analizi ile %1 ve 2 kolemanit katkılı cam-seramik örneklerinde belirlenebilen kristal fazlar müllit (PDF-00-001-0613) ve α -kordiyerittir (PDF-00-048-1600). Diğer taraftan, kordiyerit esaslı cam yapıdan sinterleme ile ilk olarak daha çok müllit kristallerinin oluştuğu görülmektedir.

Kolemanit katkılı cam örneklerinden sinterleme ile elde edilen cam-seramik tozlarında kordiyerit fazından ziyade daha çok müllit fazının oluşması, benzer konuda yapılmış bir çalışmada ifade edildiği gibi cam faz içerisinde CaO varlığının [28] düşük sıcaklıkta kordiyerit kristalleri oluşumunu baskıladığı sonucu ile örtüşmektedir. Ayrıca yine bir başka çalışmada [22] kordiyerit sitokiyometrisindeki bir cam yapının düşük sıcaklıklarda cam seramiğe dönüşümünde ilk olarak müllit kristallerinin oluştuğu görülmüştür.

Torres ve Alarcón [29] ile Wu ve Hwang [33], kordiyerit esaslı cam sisteminde B_2O_3 katkısının kristalleşme öncesi viskoz akışla yoğunlaştırmayı kolaylaştırarak μ -kordiyerit oluşumunu baskıladığı ve α -kordiyerite dönüşümde olumlu etki yaptığı belirtmiştir. Torres ve arkadaşları [32], kordiyerit esaslı cam sisteminde, artan bor oksit miktarı ile camların erime özelliklerinin iyileştiğini görmüş ve B_2O_3 içerikli camlarda artan kristalizasyon sıcaklığının cam fazda müllitin kristalleşmesini artırdığı sonucuna ulaşmışlardır. Tüm bu sonuçlar, bu çalışmadaki elde edilen bulguları desteklemektedir.

Kolemanit katkısının %1'den 2'ye arttırdığında kristal fazlara ait pik şiddetlerinin çok az azalması dışında yapısal bir değişim gözlenmemiştir. Sonuç olarak %1 oranında kolemanit katkısının kordiyerit sitokiyometrisindeki bir cam harmanının kristalleşme sıcaklığını önemli derecede azaltarak cam-seramik eldesinde önemli bir fayda sağladığı anlaşılmıştır.

4. Sonuçlar (Conclusions)

Bu çalışmada kolemanit katkısın $\text{MgO}-\text{Al}_2\text{O}_3-\text{SiO}_2$ sistemi cam-seramiklerinin sinterleme ve kristalizasyon davranışları üzerine etkileri araştırıldı. %1 oranındaki kolemanit katkısının kordiyerit sitokiyometrisine sahip cam harmanının camsı geçiş sıcaklığını yaklaşık 25°C, kristalizasyon sıcaklığını da yaklaşık 60°C azalttığı belirlenmiştir. Ayrıca kolemanit katkısının 1000°C'de kordiyerit cam-seramik yapıda kristalleşmeyi sağladığı görülmüştür. Bu sonuç özellikle mikro elektronik endüstrisinde LTCC uygulamaları için kordiyerit ile müllitin kristal faz olarak bir arada yer aldığı cam-seramik kompozit malzemelerin eldesi açısından önem arz etmektedir. Sonuç olarak kolemanit hammadesinin kordiyerit cam-seramik üretiminde katkı maddesi olarak değerlendirilebileceği sonucuna ulaşılmıştır.

Teşekkür (Acknowledgment)

Yazarlar bu çalışmayı destekleyen Afyon Kocatepe Üniversitesi, Bilimsel Araştırmalar Proje Koordinasyon Birimine (AKÜ, BAPK, Proje No: 15.MUH.10), Eti Maden İşletmeleri'ne ve Gizem Frit A.Ş'ye teşekkür ederler.

Kaynaklar (References)

- [1] Komatsu, T. (2015). Design and control of crystallization in oxide glasses. *Journal of Non-Crystalline Solids*, 428, 156-175.
- [2] McMillan, P.W. (1964). *Glass-Ceramics*, Academic Press Inc. ISBN 9780124856608.
- [3] Dimech, C. J. (2009). *The Production of novel glass-ceramics from problematic UK wastes using borates* [PhD Thesis, Imperial College London].
- [4] McColm, I. J. (1983). *Ceramic Science for Materials Technologists* (pp. 204-234), L. Hill. ISBN 9780412003516.
- [5] Singh, G., Sharma, M., & Vaish, R. (2020). Emerging trends in glass-ceramic photocatalysts. *Chemical Engineering Journal*, 126971.
- [6] Holand, W., & Beall, G.H. (2002). *Glass-Ceramic Technology* (pp. 57-72), Wiley. ISBN 9781574981070.
- [7] Vogel, V. (1994). *Glass Chemistry* (pp. 102-127), Springer-Verlag Berlin Heidelberg. DOI 10.1007/978-3-642-78723-2.
- [8] Stookey, S. D. (1959). Catalyzed crystallization of glass in theory and practice. *Industrial & Engineering Chemistry*, 51(7), 805-808.
- [9] Akpinar, S., Kuşoğlu, İ. M., Ertugrul, O., & Onel, K. (2015). *Microwave assisted sintering of in-situ cordierite foam*. *Ceramics International*, 41(7), 8605-8613.
- [10] Akpinar, S., Kusoglu, I. M., Altun, I. A., & Onel, K. (2009). Microwave Sintering: The Effect of Microwave Sintering on In-Situ Synthesis of Cordierite Powder. In *European Congress and Exhibition on Powder Metallurgy. European PM Conference Proceedings* (p. 1). The European Powder Metallurgy Association.
- [11] Szwagierczak, D., Synkiewicz, B., & Kulawik, J. (2018). Low dielectric constant composites based on B₂O₃ and SiO₂ rich glasses, cordierite and mullite. *Ceramics International*, 44(12), 14495-14501.
- [12] Marghussian, V. K., Balazadegan, O. U., & Eftekhari-Yekta, B. (2009). Crystallization behaviour, microstructure and mechanical properties of cordierite–mullite glass ceramics. *Journal of Alloys and Compounds*, 484(1-2), 902-906.
- [13] Song, L., Wu, J., Li, Z., Hao, X., & Yu, Y. (2015). Crystallization mechanisms and properties of α-cordierite glass-ceramics from K₂O-MgO-Al₂O₃-SiO₂ glasses. *Journal of Non-Crystalline Solids*, 419, 16-26.
- [14] Wu, J., Li, Z., Huang, Y., Li, F., & Yang, Q. (2014). Fabrication and characterization of low temperature co-fired cordierite glass-ceramics from potassium feldspar. *Journal of Alloys and Compounds*, 583, 248-253.
- [15] Chen, G. H. (2008). Sintering, crystallization, and properties of CaO doped cordierite-based glass-ceramics. *Journal of Alloys and Compounds*, 455(1-2), 298-302.
- [16] Dittmer, M., Yamamoto, C. F., Bocker, C., & Rüssel, C. (2011). Crystallization and mechanical properties of MgO/Al₂O₃/SiO₂/ZrO₂ glass-ceramics with and without the addition of yttria. *Solid State Sciences*, 13(12), 2146-2153.
- [17] Zdaniewski, W. (1973). Crystallization and structure of a MgO-Al₂O₃-SiO₂-TiO₂ glass-ceramic. *Journal of Materials Science*, 8(2), 192-202.
- [18] Gawronski, A., Patzig, C., Höche, T., & Rüssel, C. (2015). Effect of Y₂O₃ and CeO₂ on the crystallisation behaviour and mechanical properties of glass-ceramics in the system MgO/Al₂O₃/SiO₂/ZrO₂. *Journal of Materials Science*, 50(4), 1986-1995.
- [19] Kim, B. H., & Lee, K. H. (1994). Crystallization and sinterability of cordierite-based glass powders containing CeO₂. *Journal of Materials Science*, 29(24), 6592-6598.
- [20] Singh, K., Gupta, N., & Pandey, O. P. (2007). Effect of Y₂O₃ on the crystallization behavior of SiO₂-MgO-B₂O₃-Al₂O₃ glasses. *Journal of Materials Science*, 42(15), 6426-6432.
- [21] Chen, G. H. (2007). Effect of replacement of MgO by CaO on sintering, crystallization and properties of MgO-Al₂O₃-SiO₂ system glass-ceramics. *Journal of Materials Science*, 42(17), 7239-7244.
- [22] Chen, G. H. (2007). Effect of ZnO addition on properties of cordierite-based glass-ceramics. *Journal of Materials Science: Materials in Electronics*, 18(12), 1253-1257.
- [23] Chen, G. H., & Liu, X. Y. (2007). Sintering, crystallization and properties of MgO-Al₂O₃-SiO₂ system glass-ceramics containing ZnO. *Journal of Alloys and Compounds*, 431(1-2), 282-286.
- [24] Katzschmann, A., & Wange, P. (1995). Processability, crystallization and mechanical strength of P₂O₅-modified glasses and glass-ceramics in the system MgO-Al₂O₃-SiO₂-TiO₂. *Glastech BerGlass*, 68, 111-116.
- [25] Winter, W. (1997). Sintering and crystallization of volume-and surface-modified cordierite glass powders. *Journal of Materials Science*, 32(6), 1649-1655.
- [26] Sarıgül, M., & Günay, E. (2010). Glass formation and properties of cordierite compositions from talc-based natural raw materials with boron oxide addition. *Anadolu University Journal of Science and Technology-A Applied Sciences and Engineering*, 11, 115-124.
- [27] Oprea, C., Stan, C., Rotiu, E., & Popescu, C. (1999). Non-isothermal crystallization of cordierite glasses. *Journal of Thermal Analysis and Calorimetry*, 56(2), 1-5.
- [28] Torres, F. J., & Alarcón, J. (2005). Effect of MgO/CaO ratio on the microstructure of cordierite-based glass-ceramic glazes for floor tiles. *Ceramics International*, 31(5), 683-690.
- [29] Torres, F. J., & Alarcón, J. (2004). Microstructural evolution in fast-heated cordierite-based glass-ceramic glazes for ceramic tile. *Journal of the American Ceramic Society*, 87(7), 1227-1232.
- [30] Torres, F. J., & Alarcón, J. (2003). Effect of additives on the crystallization of cordierite-based glass-ceramics as glazes for floor tiles. *Journal of the European Ceramic Society*, 23(6), 817-826.

- [31] Synkiewicz, B., Szwagierczak, D., & Kulawik, J. (2017). Multilayer LTCC structures based on glass-cordierite layers with different porosity. *Microelectronics International*, 34(3), 110-115.
- [32] Torres, F. J., de Sola, E. R., & Alarcón, J. (2006). Effect of boron oxide on the microstructure of mullite-based glass-ceramic glazes for floor-tiles in the CaO-MgO-Al₂O₃-SiO₂ system. *Journal of the European Ceramic Society*, 26(12), 2285-2292.
- [33] Wu, J. M., & Hwang, S. P. (2000). Effects of (B₂O₃, P₂O₅) additives on microstructural development and phase-transformation kinetics of stoichiometric cordierite glasses. *Journal of the American Ceramic Society*, 83(5), 1259-1265.



Synthesis and characterization of carborane-functionalized hyperbranched polyester for boron neutron capture therapy

Gülten Özçayan^{1*}, Yüksel Şahin², Ernur Söylemez³, M. Elif Ünsal⁴

¹Turkish Energy, Nuclear and Mineral Research Authority, Nuclear Energy Research Institute, Ankara, 06983, Turkey,
ORCID orcid.org/0000-0001-9773-4569

²Department of Chemistry, Faculty of Art & Sciences, Adnan Menderes University, Aydin, 09100, Turkey,
ORCID orcid.org/0000-0001-5620-2064

³Roketsan Missiles Inc. Ankara, 06780, Turkey, ORCID orcid.org/0000-0001-9009-7915

⁴Middle East Technical University, R&D Training and Measure Center, Ankara, 06580, Turkey,
ORCID orcid.org/0000-0003-3284-098X

ARTICLE INFO

Article history:

Received July 3, 2020

Accepted February 20, 2021

Available online March 31, 2021

Research Article

DOI: [10.30728/boron.763317](https://doi.org/10.30728/boron.763317)

Keywords:

BNCT

Boron

Carborane

Esterification

Hyperbranched polyester

ABSTRACT

The purpose of this study is to synthesize new boron containing carrier compound for Boron Neutron Capture Therapy (BNCT) which is two-component radiation therapy method that especially is promising for the treatment of brain tumors and is being actively researched in many countries. For this research hyperbranched polyester (HBP), bifunctional p-carborane and carborane-functionalized HBP were synthesized. Dipentaerythritol was chosen as a core molecule of the HBP and esterified with dimethylol propionic acid. Observed characteristic ester bands and OH stretching band in the FTIR spectrum and the methyl & methylene peaks in the ¹H NMR spectrum of HBP indicated that hyperbranched polyester synthesis was done successfully. A bifunctionalized p-carborane containing an acid group and a benzyl ether protected alcohol was prepared in three-step reactions. As a result of these reactions, a bifunctionalized p-carborane compound was produced with 60% yield. Then, the HBP was esterified with the bifunctional p-carborane. The characterization of the synthesized compounds was determined by FTIR and NMR spectra. The synthesis of carborane-functionalized HBP was confirmed by disappearance of HBP's OH groups and B-H stretching band observed in the FTIR spectrum of carborane-functionalized HBP and in addition, appearance of proton signals of HBP core, carborane linker and peripheral-protecting groups in the ¹H-NMR spectrum. Finally, synthesized water-soluble carborane-containing HB carrying many boron atoms should be served as potential BNCT agents.

1. Introduction

Carboranes are polyhedral clusters consisting of carbon, hydrogen and boron. They have been widely used in many areas such as carboraneous nano-material in electrochemical, semiconductor, drug delivery, boron neutron capture therapy (BNCT), molecular imaging, molecular sensors, catalysis and gas storage applications. Carboranes have a highly electron-delocalized hydrophobic surface, spherical geometry and convenient molecular size. Carboranes can readily be reacted with other organic groups because of relatively acidic protons of the two carbon atoms of carborane. Besides, carboranes are notably charming because of their high stability and charge neutrality. In particular, use of carborane derivatives in the field of medicinal chemistry has become more attractive day by day. Carboranes are mainly used to design BNCT agents in medicinal applications [1-2].

Boron neutron capture therapy is a binary radiation therapy method which becomes a significant treatment for numerous types of tumors. Boron compound is the main component of BNCT method. The basis of BNCT is neutron capture and fission reactions. Nonradioactive boron-10 (¹⁰B) compounds accumulated in tumor cells are irradiated with low energy thermal neutrons. As a result of neutron capture reaction, alpha particles (⁴He) and lithium-7 (⁷Li) nuclei are released. In order to be successful, boron compound containing approximately 20-50 µg/g (~109 atoms/cell) of ¹⁰B must be selectively delivered to the tumor and adequate amount of thermal neutrons must be absorbed by ¹⁰B atoms. Thus, a lethal ¹⁰B(n,a)⁷Li capture reaction is occurred. High LET particles (⁴He) have limited path lengths in tissue, so destructive effects of these particles are restrained to boron in tumor cells.

*Corresponding author: gulten.ozcayan@tenmak.gov.tr

Boron delivery agents such as (L)-4-dihydroxy-boryl-phenylalanine (BPA) and sodium mercaptoundehydro-closododecaborate (BSH) are used in clinical BNCT trials. Lots of boron delivery agents have been designed and synthesized over the last few decades but only a few have been approved in preclinical trials. As a result of clinical experiences and outcomes in the development of BNCT delivery agents, many researchers have described five golden principles for ideal BNCT agents. These are: (1) ^{10}B atoms/tumor cell are required more than 10^9 (2) boron tumor/normal tissue and high tumor/blood concentration ratios ≥ 3 (3) low intrinsic toxicity (4) clearance rate from normal tissue and blood is fast and tumor retention is enhanced (5) good with hydrophobic and hydrophilic balance [2-5]. Functional delivery agents containing functional end groups which are associated with tumor targeting moieties such as receptor, peptides, folic acid, amino acids, monoclonal antibodies (MAbs), lipids, nucleosides, carbohydrates, liposomes have become the most interesting compounds among synthesized new BNCT agents.

Recently, the conjugation of carborane to dendritic molecule has been investigated to fulfill these requirements. The synthesis of dendrimer and hyperbranched polymers of dendritic molecules is one of the most studied topics because these highly branched polymers have a large number of branching points and functional end groups that can be easily modified with functional groups [6-14]. The dendrimers have well-defined shape and size. Multi-step reactions and complicated purifying processes are used in the preparation of dendrimers [15-18]. In contrast, their structures of the hyperbranched polymers are not organized as properly as dendrimers'. They contain randomly branched and some linear structures. They were firstly synthesized by simple one-pot polymerizations. Later, a chain growth mechanism e.g self-condensing vinyl polymerization and self-condensing ring-opening polymerization were used in the preparation of hyperbranched polymers [7,19-22]. Reaction strategies in the preparation of hyperbranched polymer resemble polymerization reactions of classical linear polymers rather than dendrimers. The production of dendrimers is very complex for use as engineering materials and large scale industrial purposes and also costly. On the other hand, the preparation of large quantities of hyperbranched polymers is much easier and cheaper than dendrimers but control cost of their structure and molar mass is high [22]. However, hyperbranched polymers are very attractive for industrial applications such as blend, resin and additive components and also, high-tech fields like nanomaterials in electric and electronic device, catalysis, biomedicine, etc. [22]. Terminal functional groups of hyperbranched polymers can be easily modified with other compounds to obtain new materials for specific applications [23]. These modifications bring in extra dissolution, thermal, elec-

trochemical and luminescence properties of synthesized new materials.

Various hyperbranched polymers are obtained from different core and chain extender molecules. Hyperbranched polyester (HBP) based on 2,2 bis(hydroxymethyl)propanoic acid, which is one of the first synthesized hyperbranched polymers, has been commercially available over years [22,24]. Mishra et. al. [25] studied the modification of second generation aliphatic hyperbranched polyester polyol with isoformediisocyanate for coating film. Kutyreva et. al. [26] synthesized 2nd generation HBP polyol with succinic anhydride used as a chelating agent. Murillo and co-workers [27] synthesized hyperbranched alkyd resins from 4th generation HBP modified with tall oil fatty acids. Murillo and Mesias [28] also modified second generation HBP with polylactic acid to obtain a compatibilizer agent for plasticized tapioca starch/polylactic acid blends. Hyperbranched polyesters having end hydroxyl groups were combined with fatty acids or acrylate used as various resins in coating applications [6,29-31]. As most of the studies published in the literature have concentrate on the synthesis and characterization of aliphatic hyperbranched polyester for various applications, it can't be seen any literature study about modifying aliphatic hpyerbranched polyester with carborane as a biomaterial. But, many studies about use of dendrimers as boron carriers have been found in the literature. Firstly, Barth and coworkers [32] attached isocyanato polyhedral borane [$\text{Na}(\text{CH}_3)_3\text{NB}_{10}\text{H}_8\text{NCO}$] to the outer shells of second- and fourth-generation poly(amidoamine) (PAMAM) dendrimers. In subsequent studies, dendrimers, aimed to attach it with the epidermal growth factor receptor, were designed by using boron compounds and PAMAM [33-35]. Carboranes modified to outermost groups of various dendrimers such as PAMAM [32], poly(propylene imine) [36], carbosilane [37], polylysine [38] and metallocendrimers [39] were investigated. On the other hand, these are not an ideal boron delivery agent because of their solubility and cytotoxicity. Newkome and co-workers reported that dendrimers functionalized with water-soluble carborane were synthesized [40]. Aqueous solubility was accomplished by using peripheral sulfate groups and thus, a unimolecular micelle-type structure was synthesized. Aliphatic polyester dendrimers synthesized from 2,2-bis(hydroxymethyl) propanoic acid [41] by Frechet and coworkers were biocompatible, nonimmunogenic, nontoxic and water-soluble as drug delivery agents [42-44]. Parrott et. al. studied the development of alike aliphatic polyester dendrimers for the incorporation of functionalized carborane compound [2]. In the study, the least amount of peripheral alcohol groups required per carborane was determined to evaluate the aqueous solubility of each of their synthesized structures for potential therapeutic applications of carborane-containing compounds. Carborane modified second generation dendron contain-

ing forty boron atoms from a 2,2 bis(hydroxymethyl) propanoic acid scaffold for BNCT were synthesized by Galie and coworkers. The outer shells of these dendrimers were designed to combine with targeting functionality which would be provided at the focal point or solubilizing groups [45]. Later, the tricarboranyl building block was also attached to 2,2-bis(hydroxymethyl) propionic acid with a succinimidyl linker and thus, a hexacarborane modified dendron containing 60 boron atoms was synthesized by Molland and Zharov [46].

The terminal groups (such as peripheral alcohol) of dendrimers or hyperbranched polymers provide an attractive platform to modify these with other compounds for synthesizing new specific application materials like diagnostic and therapeutic modalities into tumors. Trifunctional theranostic agent which has diagnostic and therapeutic modalities was synthesized for targeting solid tumors by Dubey et.al. In this study, photophysical properties of dendritic molecule modified with carborane, a monomethine cyanine dye and an integrin ligand were evaluated. Thus, these dendritic molecule has been acquired modalities both diagnostic such as visible-light fluorescent imaging and therapeutic such as BNCT [47].

Studies about the synthetization of aliphatic hyperbranched polyesters containing carborane have not been enough although hyperbranched polymers are prepared much easier and cheaper than dendrimers [22]. Taking all of these factors into consideration, we described the synthesis and characterization of carborane-functionalized hyperbranched aliphatic polyester in this study. Firstly, aliphatic hyperbranched polyester was synthesized with dipentaerythritol as the core molecule that was twice esterified with dimethylol propionic acid as the chain extender according to study of Bat et. al. [30]. Afterwards, this aliphatic hyperbranched polyester was modified with functionalized *p*-carborane. *p*-carborane was bifunctionalized with n-butyllithium and trimethylene oxide by three-step reaction taken into the consideration of previous study [2] in order to easily incorporation into the synthesized hyperbranched polyester. Finally, the peripheral alcohols of these synthesized hyperbranched were reacted with carboxylic acid of bifunctional *p*-carborane by esterification reaction to obtain carborane-functionalized hyperbranched polyester. All synthesized compounds were characterized by FTIR and NMR techniques.

Hydroxy functional aliphatic hyperbranched polyesters synthesized from a dimethylol propionic acid monomer and a dipentaerythritol core molecule have mostly been studied to be used as resin in coating applications [6,29-30] but not to evaluate as biomaterial carrier. The important part of our work is that the hydroxyl groups at the outer shells of aliphatic hyperbranched polyester were modified with functionalized *p*-carborane compound by esterification to be evaluated as a

biomaterial. As a result of this study, carborane-containing hyperbranched polyester carrying many boron atoms and functional groups is successfully synthesized as a candidate BNCT agent.

2. Materials and Methods

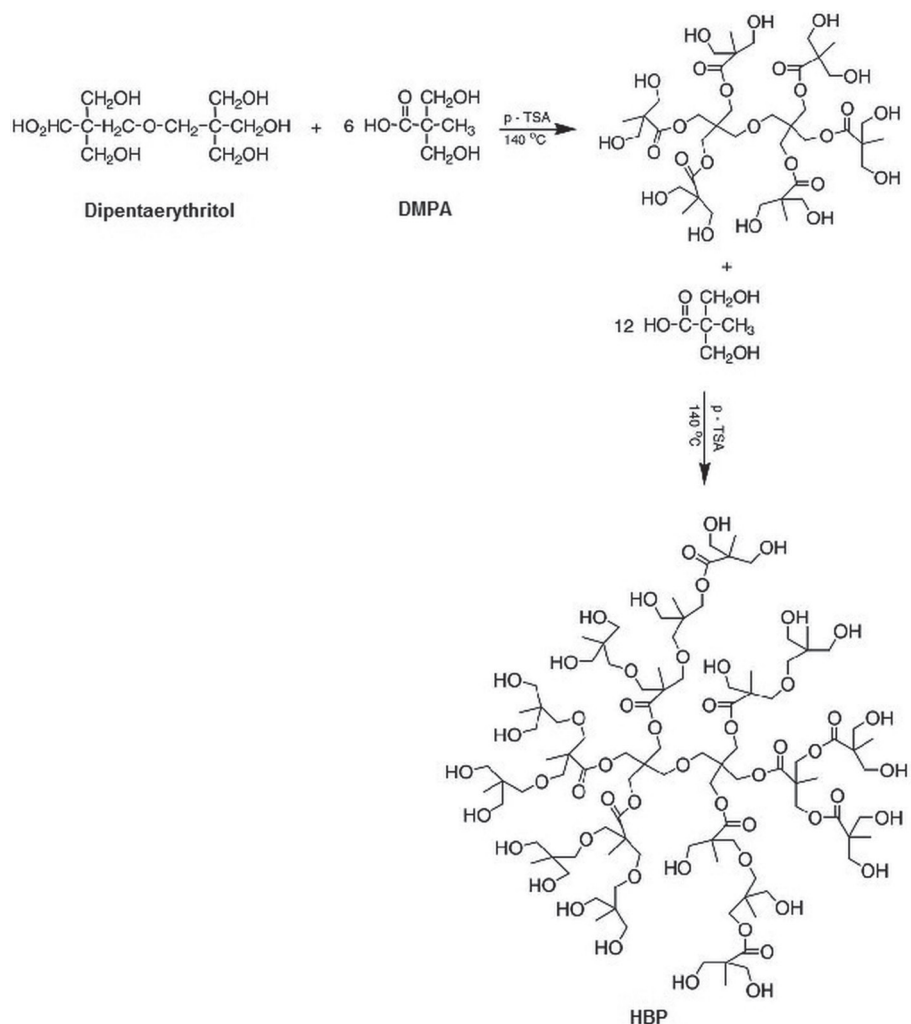
2.1. Materials

Dipentaerythritol and dimethylol propionic acid (DMPA) (synonym: bis(hydroxymethyl)propanoic acid, bis-MPA) were supplied by Aldrich. *p*-Carborane, (1,12-D-dicarbadodecarane, 1,12-C₂B₁₀H₁₂) (MA=144.23) was purchased by KATCHEM spol. s r.o., Czech Republic. Butyllithium solution (n-BuLi) (Aldrich) was used as 1.6M solution in hexanes. N,N-Dimethylformamide (anhydrous-99.8%) (DMF), Ethyl acetate, TEMPO (2,2,6,6-Tetramethyl-1-piperidinyloxy, free radical), Iodobenzene 1,1-diacetate, pyridine, sodium hydride (NaH) and benzyl bromide were supported from Aldrich. Trimethylene oxide, magnesium sulphate anhydrous and metallic sodium were purchased from Fluka. 4-(Dimethylamino)pyridine (DMAP) and Tetra-butylammonium iodide, ≥99% were supplied by Sigma. *p*-toluene sulfonic acid and *N*-Ethyl-*N*-(3-dimethylaminopropyl)carbodiimide hydrochloride (EDAC) as a catalyst was supported from Aldrich-Sigma. All solvents and reagents were of analytical grade and used without purification.

Fourier transform infrared (FTIR-ATR) spectra were recorded using FTIR Nicolet 8700 spectrometer model in the 3700–600 cm⁻¹ range. ¹H and ¹³C NMR spectra were performed on a Bruker Avance (300 MHz) and Varian (400 MHz) spectrometer with Deutero dimethyl sulfoxide(DMSO-d₆) or Deutero chloroform (CDCl₃) as a solvent at 25°C.

2.2. Synthesis of Aliphatic Hyperbranched Polyester

Aliphatic hyperbranched polyester was synthesized from dipentaerythritol and DMPA according to the literature [30-31]. In this research, the aliphatic hyperbranched polymer was synthesized by a pseudo-one step polymerization. Dipentaerythritol as core molecule and dimethylol propionic acid as chain extender were used. Appropriate quantities of dipentaerythritol, dimethylol propionic acid and *p*-toluene sulfonic acid as a catalyst were placed in a five necked flask. The flask was placed in an oil bath preheated to 140°C. After all of materials were melted, the reaction was carried out under nitrogen atmosphere and the mechanical stirrer was started (Reaction condition: Mole of DMPA=50 mmol, Mole of Dipentaerythritol=5.55 mmol, m_{catalyst}=0.5 wt% of DMPA). After 2 h, the nitrogen gas stream was turned off, vacuum line was connected to the flask and vacuum was applied from time to time in an hour. After the pressure was increased to atmospheric, the required amount of DMPA (66.7

**Figure 1.** Synthesis of 2nd generation aliphatic HBP.

mmol) and p-TSA (44.8 mg) were added and the nitrogen gas flow was restarted for 2 h and vacuum was applied for an hour. Then prepared powder product was dried at 50°C under vacuum (Yield=83.75%). The reaction scheme of the aliphatic HBP synthesis is given in Figure 1. FTIR-ATR spectrum of aliphatic HBP, cm⁻¹: 3500-3200 (strong, broad) O-H stretching, 2960-2885 (weak, broad) C-H stretching vibration in CH₃ and CH₂, 1710 (very strong C=O stretching vibration, 1459 (medium) C-H stretching vibration in CH₃, 1362 (medium) C-H deformation in CH₃ and 1227-1024 (medium) C-O-C stretching vibration.

2.3. Preparation of the Bifunctional Carborane

p-carborane was bifunctionalized as a carboxylic acid and a protected alcohol in order to incorporation of p-carborane cages with the peripheral alcohols of this synthesized aliphatic hyperbranched polyester. Then, the protected alcohols of carborane-functionalized hyperbranched polyester would subsequently be opened, and polyethylene glycol and targeting moieties should be attached to regeneration peripheral alcohol groups for use in BNCT.

The bifunctional p-carborane was prepared in three steps according to the literature procedures [2] (Figure 2).

2.3.1. 1st step: Synthesis of 1,12-bis(3-hydroxypropyl)-1,12-dicarbadodecarborane (compound 1):

Two carbon vertices of p-carborane were reacted with two equivalents of n-butyllithium and trimethylene oxide to obtain long tails containing diol group. The reaction in THF (tetrahydrofuran) solution medium (50 mL) carried out in a well dried round bottom flask in a magnetic stirrer under argon atmosphere. The reaction mixture was stirred approximately 14 h at room temperature. THF was evaporated in vacuum at the end of reaction time and crude product was dissolved with 1M hydrochloric acid (HCl). The organic layer was separated, washed with 80 ml of acid and dried in vacuum. At the end of the 1st step procedure, product was obtained as white needles with 70% yield. ¹H-NMR (400 MHz, CDCl₃, 300 K): δ=1.3 and 1.4 (dd, 4H, CH₂-p-Carbor.), 1.6 and 1.7 (dd, 4H, CH₂CH₂OH), 1.9-3.2 (br., H, p-Carbor.) and 3.3 and 3.4 (s, 4H, CH₂OH) (Figure 3).

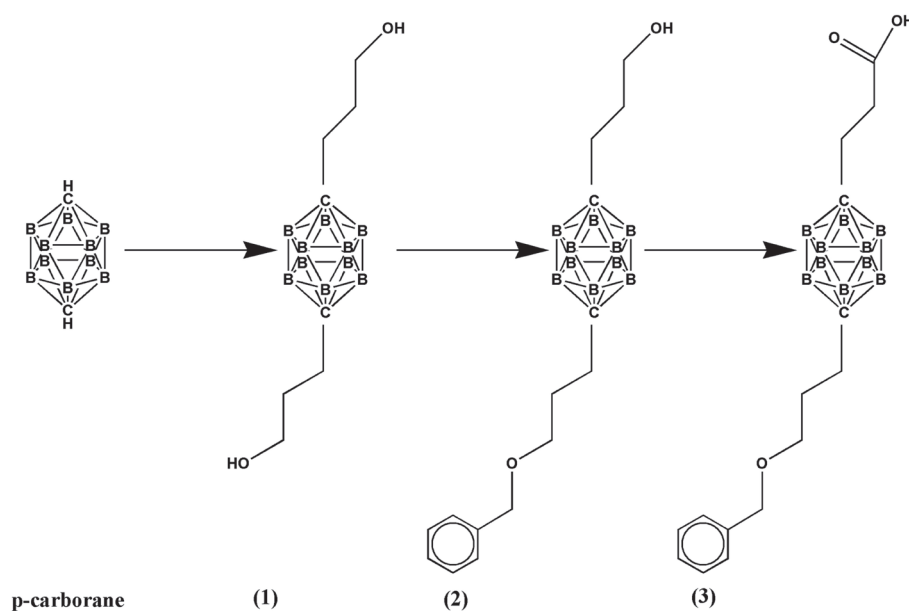


Figure 2. Synthesis steps of bifunctional p-carborane.

2.3.2. 2ndstep: Synthesis of 1-(3-(benzyloxy)propyl)-12-(3-hydroxypropyl)-1,12-dicarbadodecaborane (compound 2):

One hydroxyl group of the compound 1 was protected using NAH, Tetra-butylammonium iodide and benzyl bromide according to the literature [2]. The protected alcohol of the resulting product would be opened to re-build peripheral alcohol functionalities or attach to targeting moieties for its intended purpose. In this step, the reaction solution was firstly cooled down to 0°C and stirred for 2 h. All necessary chemicals were added.

the mixture was kept until it reached room temperature and stirred for an additional 12 h. After all volatiles were removed by vacuum, the residue was taken up in 80 mL of diethyl ether and transferred into a separatory funnel. Then, 80 mL of HCl was rigorously added to dissolve crude product. After drying procedure, 1-(3-(benzyloxy)propyl)-12-(3-hydroxypropyl)-1,12-dicarbadodecarborane (compound 2) was obtained as white solid with 50-55% yield. $^1\text{H-NMR}$ (400 MHz, CDCl_3 , 300 K): δ =1.2 and 1.3 (dd, 4H, CH_2 -p-Carb.), 1.6 and 1.7 (dd, 4H, $\text{CH}_2\text{CH}_2\text{O}$), 2.0-3.1 (br., H, p-Carb.), 3.2 (d, 2H, CH_2OH), 3.4 (d, 2H, CH_2O), 4.3 (s,

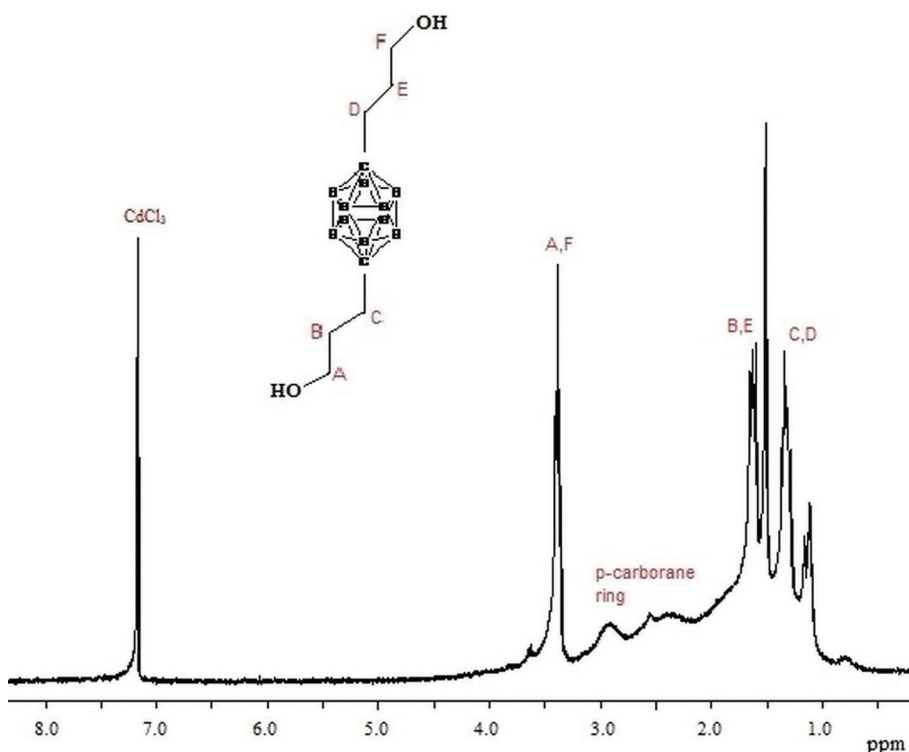


Figure 3. $^1\text{H-NMR}$ (400 MHz, CDCl_3 , 300 K) spectra of 1,12-bis(3-hydroxypropyl)-1,12-dicarbadodecaborane.

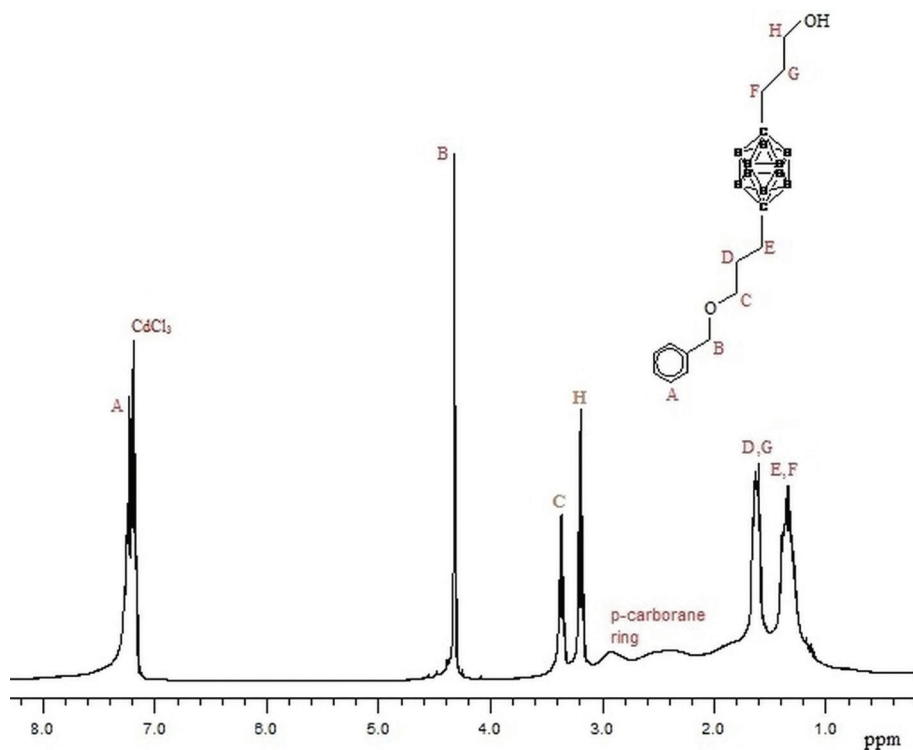


Figure 4. ^1H -NMR (400 MHz, CDCl_3 , 300 K) spectrum of 1-(3-(benzyloxy)propyl)-12-(3-hydroxypropyl)-1,12-dicarbadodecaborane.

2H, $\text{OCH}_2\text{-Ph}$), 7.3 (m, 5H, Ph) (Figure 4).

2.3.3. 3rd step: Synthesis of 12-(benzyloxy)propyl-1,12-dicarbadodecaboranyl-1-(3-propionic acid) (Compound 3):

The remaining free alcohol of compound 2 was reacted with TEMPO and iodobenzene diacetate according to the steps in the literature [2]. At the end of this procedure, the product was crystallized from ethanol and p-carborane containing carboxyl group (Compound 3) was obtained as colorless crude product with 60% yield. ^1H -NMR (400 MHz, CDCl_3 , 300 K): δ =0.8-2.3 (br., H, p-Carbor., one above the other), 1.29 (t, 2H, $\text{CH}_2\text{-p-Carbor.}$), 1.47-1.51 (dt, 4H, $\text{CH}_2\text{-p-Carbor.}$

and CH_2COOH), 1.72-1.76 (q, 2H, $\text{CH}_2\text{CH}_2\text{-p-Carbor.}$), 3.30 (t, 2H, CH_2O), 4.43 (s, 2H, $\text{OCH}_2\text{-Ph}$), 7.30 (m, 5H, Ph), 9.62 (s, H, COOH) (Figure 5).

2.4. Synthesis of Carborane-functionalized Hyperbranched Polyester

The peripheral alcohols of the synthesized aliphatic hyperbranched polyester were reacted with bifunctional p-carborane by esterification reaction to obtain carborane-functionalized hyperbranched polyester. All synthesis was carried out under airless medium. In this reaction, a small excess of bifunctional p-carborane (the carborane acid) (1.25 equiv. per alcohol) was used to complete functionalization. Appropriate quantities of

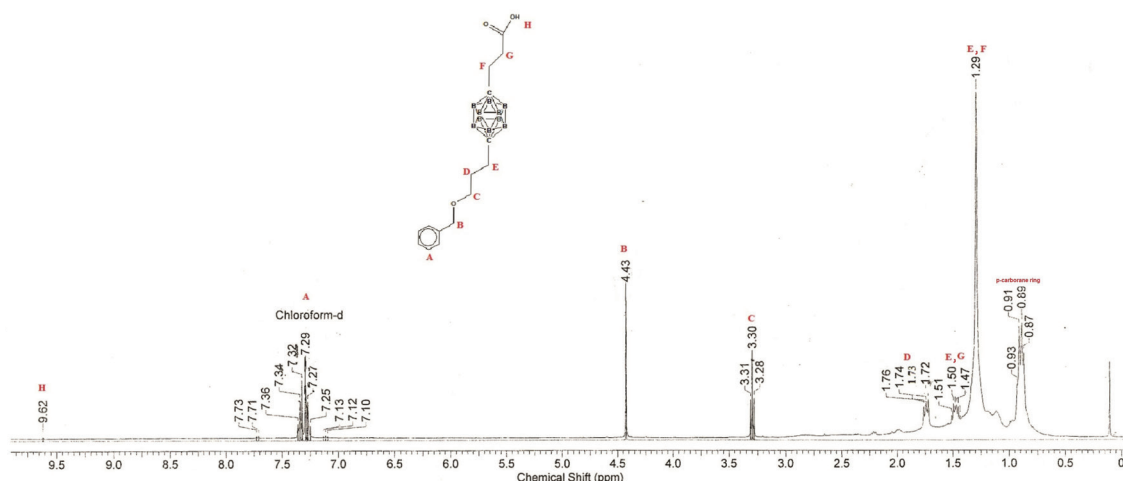


Figure 5. ^1H -NMR (400 MHz, CDCl_3 , 300 K) spectrum of 12-(benzyloxy)propyl-1,12-dicarbadodecaboranyl-1-(3-propionic acid).

aliphatic HBP and compound 3 were placed in a flask and vacuum was applied to remove air and humidity. 4 mL of dichloromethane (CH_2Cl_2) and 0.4 mL of dried pyridine were added to this mixture, respectively. Solutions of EDAC and DMPA in CH_2Cl_2 were prepared into dried tapped bottom flask equipped. These solutions were added into reaction mixture drop by drop under argon atmosphere. Reaction solution was mixed for 40 hours. After all volatiles were removed by vacuum, residue colorless solid was washed by distilled water three times in order to provide neutral solid product and thus, pyridine was removed. 8 mL of cooled pentane was added to the residue and unreacted organic impurity was removed by filtration. The product was crystallized from hexanes at -30°C and the colorless needles crystal product was obtained with 60% yield. ^1H and ^{13}C NMR spectra of final product were performed with $\text{CDCl}_3\text{-d}_1$ as a solvent at 25°C .

3. Results and Discussion

Aliphatic hyperbranched polyester was synthesized according to esterification reaction with acid catalyst and by azeotropic distillation method with toluene in the literature [30,31]. The FTIR and ^1H NMR spectra of aliphatic HBP are given in Figure 6 and 7, respectively. In the FTIR spectrum of aliphatic HBP, the characteris-

tic ester bands ($\text{C}=\text{O}$ and $\text{C}-\text{O}-\text{C}$ stretching vibrations) are observed at 1710 cm^{-1} and $1227\text{-}1024\text{ cm}^{-1}$, respectively. Also, the broadest and the most intense OH stretching band is observed at 3350 cm^{-1} in Figure 6.

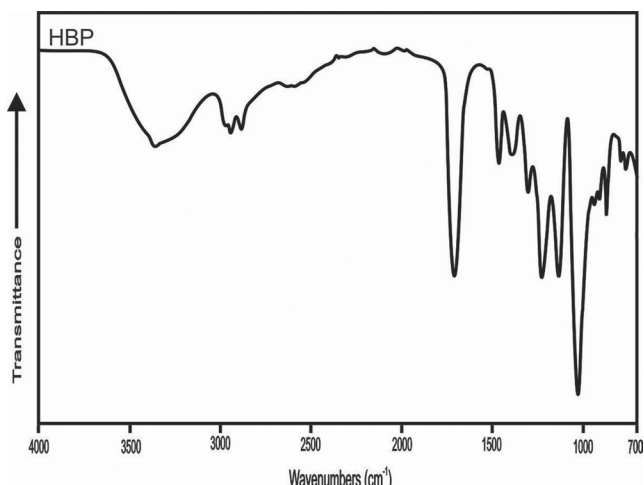


Figure 6. FTIR spectrum of aliphatic hyperbranched polyester.

As it was seen from ^1H NMR spectrum of aliphatic HBP, observed characteristic peaks of CH_3 and CH_2 at 1.1-1.3 ppm and 3.4-4.3 ppm (a, b, c and d, e, f, respectively) show a clear indication of aliphatic hyperbranched polyester synthesis in Figure 7.

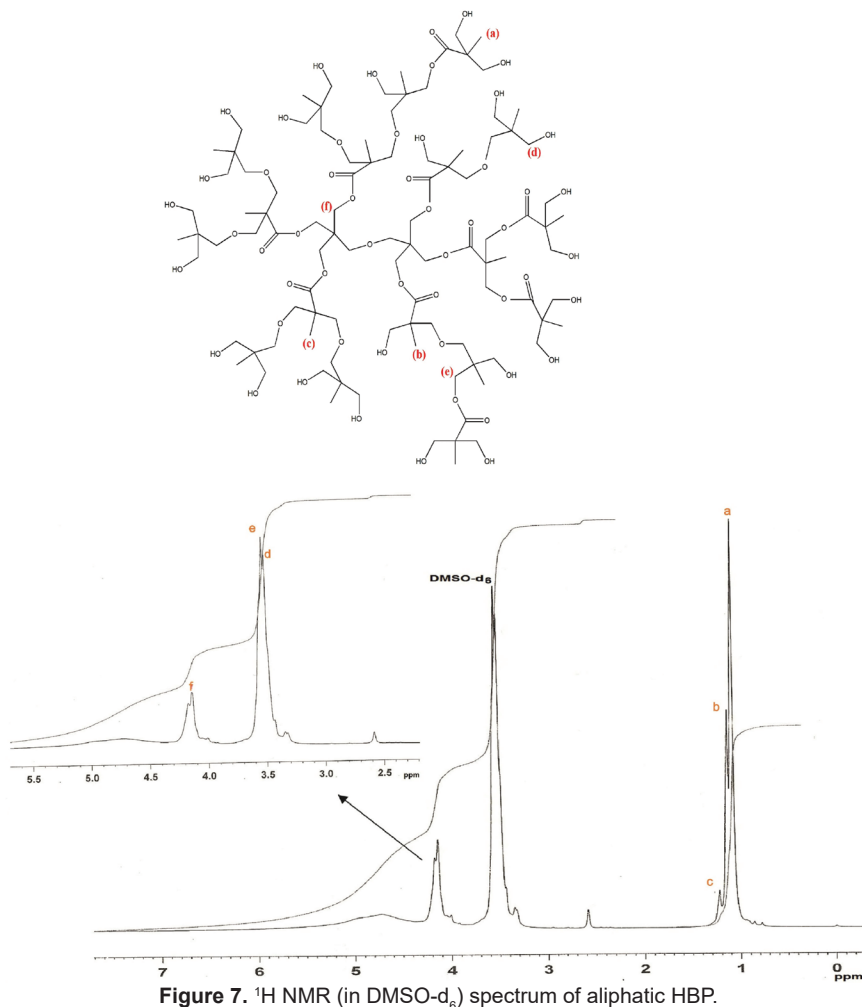


Figure 7. ^1H NMR (in DMSO-d_6) spectrum of aliphatic HBP.

The most important point in the modification of carborane cages into the aliphatic hyperbranched polyester is the preparation of a bifunctionalized carborane containing a carboxylic acid and a protected alcohol. The bifunctional p-carborane was synthesized in three steps according to the literature procedures [2].

Amounts of used acids (HCl) and the crystallization medium in the synthesis of compounds 1, 2 and 3 were slightly different from the literature [2]. At first, p-carborane was reacted with two equivalents of *n*-butyllithium and trimethylene oxide to produce the long tails compound 1 containing two -OH groups with 70% yield. Then, benzyl bromide was attached to one of two -OH groups in compound 1 by protonation under basic condition to obtain compound 2. Finally, the remaining free alcohol of compound 2 was oxidized with TEMPO and IBDA to yield compound 3 containing carboxylic acid in 60% yield. The synthesis of 12-(benzyloxy)propyl-1,12-dicarbadodecarboranyl-1-(3-propionic acid) (bifunctionalized p-carborane, compound 3) is confirmed by the evaluation of ¹H NMR spectrum (Figure 5). The observed proton signals of phenyl group at 7.29 and 7.73 ppm, -CH₂O- at 4.43 ppm, -OCH₂CH₂ at 3.31-3.28 and -CH₂ at 1.76-1.72 ppm are confirmed the formation of bifunctionalized p-carborane cages.

The peripheral alcohols of this aliphatic hyperbranched polyester were reacted with bifunctional p-carborane by esterification reaction under airless medium to synthesize carborane-functionalized hyperbranched polyester. The FTIR spectra of aliphatic HBP, bifunctionalized p-carborane and carborane-functionalized hyperbranched polyester are given in Figure 8. Comparative analysis of FTIR of these compounds indicates that the broad band of OH group of aliphatic hyperbranched polyester at 3361 cm⁻¹ disappearance in the spectrum of carborane-functionalized hyperbranched polyester. However, B-H stretching band of bifunctionalized p-carborane and C=O stretching in ester groups of aliphatic HBP are observed at 2597

cm⁻¹ and 1739 cm⁻¹, respectively in the spectrum of carborane-functionalized hyperbranched polyester.

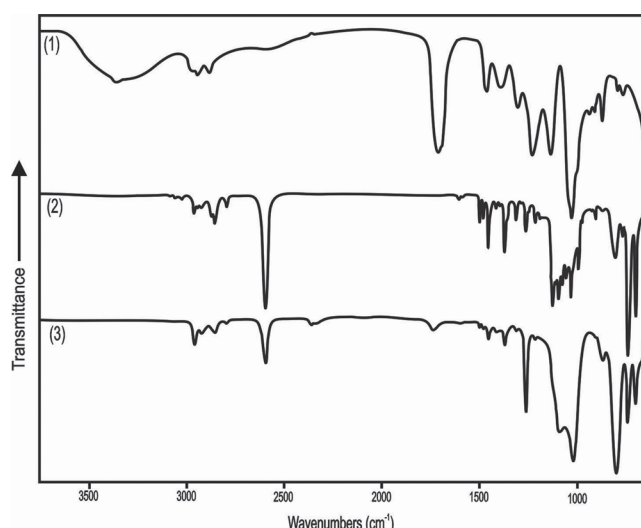


Figure 8. FTIR spectra of (1) aliphatic HBP (2) bifunctional p-carborane and (3) carborane-functionalized hyperbranched polyester.

The synthesis of carborane-functionalized hyperbranched polyester is confirmed by ¹³C and ¹H NMR spectra (Figure 9 and 10). As it was seen from ¹³C NMR spectrum of carborane-functionalized hyperbranched polyester o-, m- and p-C atoms of phenyl group at 128.4 ppm and 127.6 ppm as overlapping and also ipso C atom at 138.2 ppm are observed in the aromatic area. The peaks of -O-CH₂ in bifunctionalized p-carborane group are observed at 72.8 ppm, 69.2 ppm and 61.9 ppm (C_B, C_H and C_C), respectively. The five peaks between 34.5 ppm and 29.6 ppm indicate that 34.5 and 34.2 ppm for O-CH₂ (C_H ve C_B), 32.5 ppm for carbon resonances in methyl groups (CH₃) and 29.7-29.6 ppm for CCH₂CH₂ group (C_D ve C_G) are observed in the ¹³C NMR spectrum of carborane-functionalized hyperbranched polyester. However, the peaks of carbon atom in the carborane cage and C-atom bound to branched oxygen atoms have not been exactly identified in ¹³C NMR spectrum, carbon atoms of carbonyl are observed as a weak peak at ~168.8 ppm.

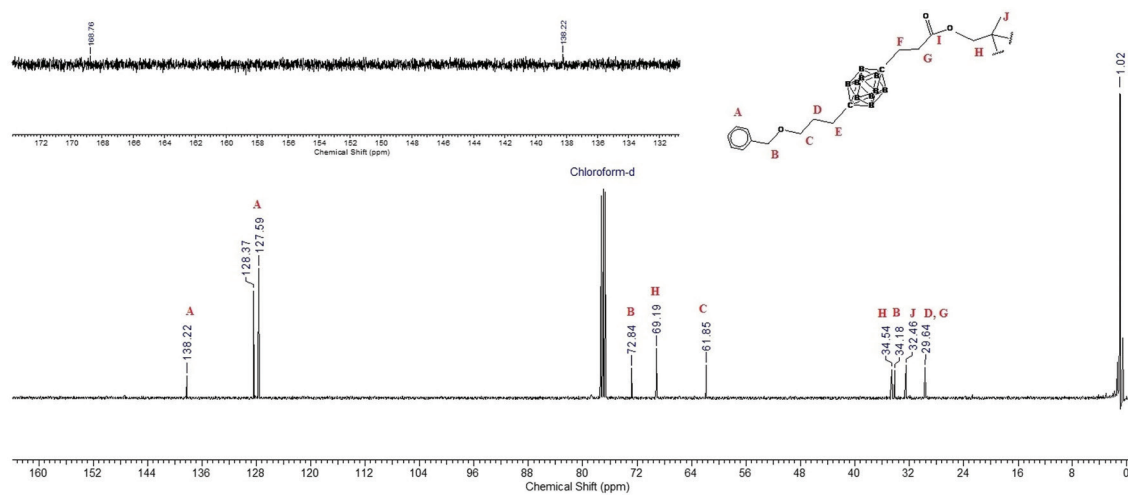


Figure 9. ¹³C NMR (100 MHz, CDCl₃, 300 K) spectrum of carborane-functionalized hyperbranched polyester.

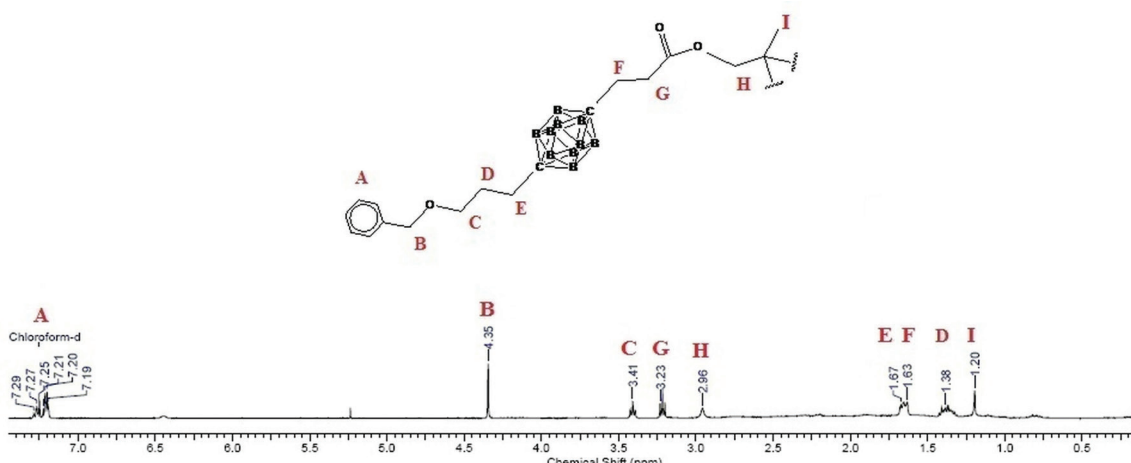


Figure 10. ^1H NMR (400 MHz, CDCl_3 , 300 K) spectrum of carborane-functionalized hyperbranched polyester.

The ^1H NMR spectrum for carborane-functionalized hyperbranched polyester indicates all of the expected resonances that show the aliphatic hyperbranched polyester center, the carborane bond and outer-protecting groups (Figure 10). $^1\text{H-NMR}$ (400 MHz, CDCl_3 , 300 K): δ =0.7-2.8 (br., H, Carbor., one above the other), 1.20 (s, 3H, CH_3 , polyester), 1.38 (t, 2H, CH_2CH_2 -p-Carbor.), 1.63-1.67 (m, 4H, CH_2CH_2 -p-Carbor.), 2.96 (br., 2H, OCH_2), 3.23 (t, 2H, CH_2COO), 3.41 (t, 2H, CH_2O), 4.35 (s, 2H, $\text{OCH}_2\text{-Ph}$), 7.30 (m, 5H, Ph) respectively in Figure 10 (A, B, C, G, H, E, F, D and I, respectively in Figure 10).

The $^1\text{H-NMR}$ of carborane characteristically exhibits a broad signal between -0.75 and 3.00 ppm coming from the protons next to the boron atoms of the carborane cage. The observed broad B-H resonances related to carborane in this spectrum inhibit accurate integration of signals between 0.7 ppm and 2.8 ppm. However, the appearance of proton signals of phenyl group at 7.29-7.25 ppm, - $\text{OCH}_2\text{-Ph}$ at 4.35 ppm, - OCH_2 at 3.41 ppm, - CH_2CH_2 at 1.67-1.63 ppm and - CH_3 at 1.20 ppm is also confirmed the synthesis of carborane-functionalized hyperbranched polyester.

As a result of this study, the functionalization of the p-carborane compound and the synthesis of the aliphatic hyperbranched polyester structure were made according to the literature. The characterization results (FTIR and NMR data) closely matched those in the literature [2,6,24,29]. A compound containing hydrophilic and multi-functional groups should be chosen as a carrier in order to use p-carborane as a biomaterial. There are many studies in the literature showing that the water solubility of carborane, which has a hydrophobic surface, is increased by modification of dendrimer structure [2,32,36-39,45-48]. These studies indicate that aliphatic hyperbranched polyester structures are synthesized more easily, cheaply and in large quantities than dendrimers. Also, aliphatic hyperbranched polyester provides good hydrophobic and hydrophilic balance, low viscosity, solubility etc. to structure which is modified [22-31]. For these reasons, aliphatic

hyperbranched polyester was chosen as the carrier for p-carborane used as a biomaterial. The peripheral -OH groups of the synthesized aliphatic hyperbranched polyester were reacted with carboxylic acid group of bifunctionalized p-carborane by esterification reaction to get a water-soluble material containing many boron atoms. Synthesized carborane-functionalized hyperbranched polyester can be evaluated for use in many different areas (flame-retardant material, radiation shielding material, biosensor), especially biomedicine.

4. Conclusions

This work presents the synthesis and characterization of aliphatic hyperbranched polyester, bifunctionalized p-carborane and carborane-functionalized hyperbranched polyester. The synthesized water-soluble aliphatic hyperbranched polyester containing 24 hydroxyl groups at the outer of its periphery can be modified with different functional materials for different purposes. In this study, water-soluble aliphatic HBP was used as boron carrier agent. It is necessary to overcome steric hindrance of carborane compound in order to easily incorporation of p-carborane cages with peripheral alcohols of carrier agent. A space between the carborane cage and the acid functionality is formed by bifunctional process to reduce this hindrance. The peripheral alcohols of the synthesized aliphatic hyperbranched polyester were reacted with carboxylic acid group of bifunctionalized p-carborane, thus carborane-containing hyperbranched polyester carrying many boron atoms was synthesized to fulfill the required boron amounts for a successful BNCT application. Future studies will focus on determining the amount of boron in the carborane-functionalized hyperbranched polyester compound, deprotonation of this compound and the attachment of polyethylene glycol and targeting moieties such as folic acid for use in BNCT and the evaluation of its toxicity by cell culture studies. This study will contribute to the synthesis and use of end products containing boron compounds in our country.

Acknowledgements

The author thanks for the support of the TAEK (Turkish Atomic Energy Authority) through TAEK-A3.H2.P2.01 project. Also, the author would like to express her gratitude and appreciation to Prof. Dr. Güngör GÜNDÜZ at Middle East Technical University for the helpful discussions about hyperbranched polyester synthesis.

References

- [1] Endo, Y. (2018). Carboranes as hydrophobic pharmacophores: applications for design of nuclear receptor ligands. In Hey-Hawkins E. & Texidior C. V. (Eds.), *Boron-based compounds: Potential and emerging applications in medicine* (pp. 3-19). John Wiley & Sons Ltd.
- [2] Parrott, M. C., Marchington, E. B., Valliant, J. F., & Adronov, A. (2005). Synthesis and properties of carborane-functionalized aliphatic polyester dendrimers. *Journal of the American Chemical Society*, 127(34), 12081-12089.
- [3] Barth, R. F., Coderre, J. A., Vicente, M. G. H., & Blue, T. E. (2005). Boron neutron capture therapy of cancer: current status and future prospects. *Clinical Cancer Research*, 11(11), 3987-4002.
- [4] Hu, K., Yang, Z., Zhang, L., Xie, L., Wang, L., Xu, H., ... & Zhang, M. R. (2020). Boron agents for neutron capture therapy. *Coordination Chemistry Reviews*, 405, 213139.
- [5] Hawthorne, M. F. (1993). The role of chemistry in the development of boron neutron capture therapy of cancer. *Angewandte Chemie International Edition in English*, 32(7), 950-984.
- [6] Bat, E. (2005). Synthesis and characterization of hyperbranched and air drying fatty acid based resins [MSc Thesis, Middle East Technical University, Graduate School of Natural and Applied Sciences]. Council of Higher Education Thesis Center (Thesis Number 166837).
- [7] Gao, C., & Yan, D. (2004). Hyperbranched polymers: from synthesis to applications. *Progress in polymer science*, 29(3), 183-275.
- [8] Kim, Y. H. (1998). Hyperbranched polymers 10 years after. *Journal of Polymer Science Part A: Polymer Chemistry*, 36(11), 1685-1698.
- [9] Uhrich, K. (1997). Hyperbranched polymers for drug delivery. *Trends in Polymer Science*, 12(5), 388-393.
- [10] Cheng, K. C., & Wang, L. Y. (2002). Kinetic model of hyperbranched polymers formed in copolymerization of AB₂ monomers and multifunctional core molecules with various reactivities. *Macromolecules*, 35(14), 5657-5664.
- [11] Liu, H., Näsmann, J. H., & Skrifvars, M. (2000). Radical alternating copolymerization: A strategy for hyperbranched materials. *Journal of Polymer Science Part A: Polymer Chemistry*, 38(17), 3074-3085.
- [12] Kuchanov, S., Slot, H., & Stroeks, A. (2004). Development of a quantitative theory of polycondensation. *Progress in polymer science*, 29(6), 563-633.
- [13] Cheng, K. C., Chuang, T. H., Tsai, T. H., Guo, W., & Su, W. F. (2008). Model of hyperbranched polymers formed by monomers A₂ and B_g with end-capping molecules. *European polymer journal*, 44(9), 2998-3004.
- [14] Fradet, A., & Tessier, M. (2007). First Shell Substitution Effects in Hyperbranched Polymers: Kinetic– Recursive Probability Analysis. *Macromolecules*, 40(20), 7378-7392.
- [15] Jiikei, M., Chon, S. H., Kakimoto, M. A., Kawauchi, S., & Imase, T. (1999). Synthesis of hyperbranched aromatic polyamide from aromatic diamines and trimesic acid. *Macromolecules*, 32(6), 2061-2064.
- [16] Liu, Q., Zhao, P., & Chen, Y. (2007). Divergent synthesis of dendrimer-like macromolecules through a combination of atom transfer radical polymerization and click reaction. *Journal of Polymer Science Part A: Polymer Chemistry*, 45(15), 3330-3341.
- [17] Hirao, A., Matsuo, A., & Watanabe, T. (2005). Precise synthesis of dendrimer-like star-branched poly (methyl methacrylate)s up to seventh generation by an iterative divergent approach involving coupling and transformation reactions. *Macromolecules*, 38(21), 8701-8711.
- [18] Bai, Y., Song, N., Gao, J. P., Sun, X., Wang, X., Yu, G., & Wang, Z. Y. (2005). A new approach to highly electrooptically active materials using cross-linkable, hyperbranched chromophore-containing oligomers as a macromolecular dopant. *Journal of the American Chemical Society*, 127(7), 2060-2061.
- [19] Powell, K. T., Cheng, C., & Wooley, K. L. (2007). Complex amphiphilic hyperbranched fluoropolymers by atom transfer radical self-condensing vinyl (co) polymerization. *Macromolecules*, 40(13), 4509-4515.
- [20] Cheng, K. C., Chuang, T. H., Chang, J. S., Guo, W., & Su, W. F. (2005). Effect of feed rate on structure of hyperbranched polymers formed by self-condensing vinyl polymerization in semibatch reactor. *Macromolecules*, 38(20), 8252-8257.
- [21] Cheng, K. C. (2003). Kinetic model of hyperbranched polymers formed by self-condensing vinyl polymerization of AB^{*} monomers in the presence of multifunctional core molecules with different reactivities. *Polymer*, 44(3), 877-882.
- [22] Žagar, E., & Žigon, M. (2011). Aliphatic hyperbranched polyesters based on 2, 2-bis (methylole) propionic acid-Determination of structure, solution and bulk properties. *Progress in Polymer Science*, 36(1), 53-88.
- [23] Mesias, R., & Murillo, E. A. (2015). Hyperbranched polyester polyol modified with polylactic acid. *Journal of Applied Polymer Science*, 132(10), 44-52.
- [24] Murillo, E. A., Vallejo, P. P., Sierra, L., & López, B. L. (2009). Characterization of hyperbranched polyol polyesters based on 2, 2-bis (methylole propionic acid) and pentaerythritol. *Journal of Applied Polymer Science*, 112(1), 200-207.
- [25] Mishra, A. K., Jena, K. K., & Raju, K. V. S. N. (2009). Synthesis and characterization of hyperbranched polyester–urethane–urea/K10-clay hybrid coatings. *Progress in Organic Coatings*, 64(1), 47-56.
- [26] Kutyreva, M. P., Usmanova, G. S., Ulakhovich, N. A., & Kutyrev, G. A. (2010). Polynuclear Cu (II) complexes with hyperbranched polyester carboxylates. *Russian Journal of General Chemistry*, 80(4), 787-789.

- [27] Murillo, E. A., Vallejo, P. P., & López, B. L. (2011). Effect of tall oil fatty acids content on the properties of novel hyperbranched alkyd resins. *Journal of Applied Polymer Science*, 120(6), 3151-3158.
- [28] Mesias, R., & Murillo, E. (2018). Hyperbranched polyester polyol modified with polylactic acid as a compatibilizer for plasticized tapioca starch/polylactic acid blends. *Polímeros*, 28(1), 44-52.
- [29] Jovičić, M., Radičević, R., Pavličević, J., Bera, O., & Govedarica, D. (2020). Synthesis and characterization of ricinoleic acid based hyperbranched alkyds for coating application. *Progress in Organic Coatings*, 148, 105832.
- [30] Bat, E., Gündüz, G., Kısakürek, D., & Akhmedov, İ. M. (2006). Synthesis and characterization of hyperbranched and air drying fatty acid based resins. *Progress in Organic Coatings*, 55(4), 330-336.
- [31] Malmström, E., Johansson, M., & Hult, A. (1995). Hyperbranched aliphatic polyesters. *Macromolecules*, 28(5), 1698-1703.
- [32] Barth, R. F., Adams, D. M., Soloway, A. H., Alam, F., & Darby, M. V. (1994). Boronated starburst dendrimer-monoclonal antibody immunoconjugates: evaluation as a potential delivery system for neutron capture therapy. *Bioconjugate chemistry*, 5(1), 58-66.
- [33] Sauter, G., Maeda, T., Waldman, F. M., Davis, R. L., & Feuerstein, B. G. (1996). Patterns of epidermal growth factor receptor amplification in malignant gliomas. *The American journal of pathology*, 148(4), 1047-1053.
- [34] Gillies, E. R., & Fréchet, J. M. (2005). Dendrimers and dendritic polymers in drug delivery. *Drug discovery today*, 10(1), 35-43.
- [35] Ihre, H. R., Padilla De Jesús, O. L., Szoka, F. C., & Fréchet, J. M. (2002). Polyester dendritic systems for drug delivery applications: design, synthesis, and characterization. *Bioconjugate chemistry*, 13(3), 443-452.
- [36] Yao, H., Grimes, R. N., Corsini, M., & Zanello, P. (2003). Polynuclear Metallacarborane– Hydrocarbon Assemblies: Metallacarborane Dendrimers. *Organometallics*, 22(22), 4381-4383.
- [37] Núñez, R., González, A., Viñas, C., Teixidor, F., Sil-lanpää, R., & Kivekäs, R. (2005). Approaches to the preparation of carborane-containing carbosilane compounds. *Organic letters*, 7(2), 231-233.
- [38] Qualmann, B., Kessels, M. M., Musiol, H. J., Sierralta, W. D., Jungblut, P. W., & Moroder, L. (1996). Synthesis of boron-rich lysine dendrimers as protein labels in electron microscopy. *Angewandte Chemie International Edition in English*, 35(8), 909-911.
- [39] Arnsbach, D., Cattalini, M., Constable, E. C., Housecroft, C. E., & Phillips, D. (1996). Boron-rich metallogenodrimers—mix-and-match assembly of multifunctional metallosupramolecules. *Chemical Communications*, (15), 1823-1824.
- [40] Newkome, G. R., Keith, J. M., Baker, G. R., Escamilla, G. H., & Moorefield, C. N. (1994). Chemistry within a Unimolecular Micelle Precursor: Boron Superclusters by Site- and Depth-Specific Transformations of Dendrimers. *Angewandte Chemie International Edition in English*, 33(6), 666-668.
- [41] Ihre, H., Padilla De Jesús, O. L., & Fréchet, J. M. (2001). Fast and convenient divergent synthesis of aliphatic ester dendrimers by anhydride coupling. *Journal of the American Chemical Society*, 123(25), 5908-5917.
- [42] Ihre, H., Hult, A., & Söderlind, E. (1996). Synthesis, characterization, and ¹H NMR self-diffusion studies of dendritic aliphatic polyesters based on 2, 2-bis (hydroxymethyl) propionic acid and 1, 1, 1-tris (hydroxyphenyl) ethane. *Journal of the American Chemical Society*, 118(27), 6388-6395.
- [43] Ihre, H., Hult, A., Fréchet, J. M., & Gitsov, I. (1998). Double-stage convergent approach for the synthesis of functionalized dendritic aliphatic polyesters based on 2, 2-bis (hydroxymethyl) propionic acid. *Macromolecules*, 31(13), 4061-4068.
- [44] Padilla De Jesús, O. L., Ihre, H. R., Gagne, L., Fréchet, J. M., & Szoka, F. C. (2002). Polyester dendritic systems for drug delivery applications: in vitro and in vivo evaluation. *Bioconjugate chemistry*, 13(3), 453-461.
- [45] Galie, K. M., Mollard, A., & Zharov, I. (2006). Polyester-based carborane-containing dendrons. *Inorganic chemistry*, 45(19), 7815-7820.
- [46] Mollard, A., & Zharov, I. (2006). Tricarboranyl pentaerythritol-based building block. *Inorganic chemistry*, 45(25), 10172-10179.
- [47] Dubey, R., Kushal, S., Mollard, A., Vojtovich, L., Oh, P., Levin, M. D., ... & Olenyuk, B. Z. (2015). Tumor targeting, trifunctional dendritic wedge. *Bioconjugate chemistry*, 26(1), 78-89.
- [48] Benhabbour, S. R., Parrott, M. C., Gratton, S. E., & Adronov, A. (2007). Synthesis and properties of carborane-containing dendronized polymers. *Macromolecules*, 40(16), 5678-5688.